Title
Fabrication and Characterization of Gecko-inspired Fibrillar Adhesive

Author
Kim, Yongkwan

Publication Date
2014

Peer reviewed|Thesis/dissertation

Fabrication and Characterization of Gecko-inspired Fibrillar Adhesive

By

Yongkwan Kim

A dissertation submitted in partial satisfaction of the
requirements for the degree of
Doctor of Philosophy

in

Chemical Engineering

in the

Graduate Division

of the

University of California, Berkeley

Committee in charge:

Professor Roya Maboudian
Professor David Graves
Professor Ali Javey

Spring 2014

Fabrication and Characterization of Gecko-inspired Fibrillar Adhesive

Abstract

Fabrication and Characterization of Gecko-inspired Fibrillar Adhesive

by

Yongkwan Kim

Doctor of Philosophy in Chemical and Biomolecular Engineering

University of California, Berkeley

Professor Roya Maboudian, Chair

Over the last decade, geckos' remarkable ability to stick to and climb surfaces found in nature has motivated a wide range of scientific interest in engineering gecko-mimetic surface for various adhesive and high friction applications. The high adhesion and friction of its pads have been attributed to a complex array of hairy structures, which maximize surface area for van der Waals interaction between the toes and the counter-surface. While advances in micro- and nanolithography technique have allowed fabrication of increasingly sophisticated gecko mimetic surfaces, it remains a challenge to produce an adhesive as robust as that of the natural gecko pads. In order to rationally design gecko adhesives, understanding the contact behavior of fibrillar interface is critical.

The first chapter of the dissertation introduces gecko adhesion and its potential applications, followed by a brief survey of gecko-inspired adhesives. Challenges that limit the performance of the current adhesives are presented. In particular, it is pointed out that almost all testing of gecko adhesives have been on clean, smooth glass, which is ideal for adhesion due to high surface energy and low roughness. Surfaces in application are more difficult to stick to, so the understanding of failure modes in low energy and rough surfaces is important.

The second chapter presents a fabrication method for thermoplastic gecko adhesive to be used for a detailed study of fibrillar interfaces. Low-density polyethylene nanofibers are replicated from a silicon nanowire array fabricated by colloidal lithography and metal-catalyzed chemical etching. This process yields a highly ordered array of nanofibers over a large area with control over fiber diameter, length, and number density. The high yield and consistency of the process make it ideal for a systematic study on factors that affect adhesion and friction of gecko adhesives.

The following three chapters examine parameters that affect macroscale friction of fibrillar adhesives. Basic geometric factors, namely fiber length and diameter, are optimized on smooth glass for high friction. The test surfaces are then processed to intentionally introduce roughness or lower the surface energy in a systematic and quantifiable manner, so that the failure mechanisms

of the adhesive can be investigated in detail. In these studies, observed macroscale friction is related to the nano-scale contact behavior with simple mechanical models to establish criteria to ensure high performance of fibrillar adhesives.

Chapter 6 presents various methods to produce more complex fiber structures. The metal-assisted chemical etching of silicon nanowires is studied in detail, where the chemical composition of the etching bath can be varied to produce clumped, tapered, tilted, and curved nanowires, which provide interesting templates for molding and are potentially useful for applications in various silicon nanowire devices. Hierarchical fiber structures are fabricated by a few different methods, as well as composite structures where the fibers are embedded in another material. A way to precisely control tapering of microfibers is demonstrated, and the effect of tapering on macroscale friction is studied in detail. The final chapter summarizes the dissertation and suggests possible future works for both further investigating fibrillar interfaces and improving the current gecko adhesive.

Contents

Acknowledgments

I want to thank Professor Roya Maboudian for helping me have such a meaningful experience in graduate school. I feel that I have matured so much academically and personally the last five years, and I owe much of it to my interaction with her. Her kind and calm natured support has always been encouraging throughout both good and challenging times. Most importantly, she always put my interest as a student before hers, a true advisor in every sense of the word.

I am grateful to Dae Ho Lee, who has been a great mentor inside the lab and a great friend outside, and who I respect as a hard worker and a critical thinker. I will never forget the stimulating discussions (both scientific and completely non-scientific) and late night lab work with him.

I cannot overstate the help of the undergraduate researchers Francesca Limanto, Angela Tsao, Mengwen Zhang, Robert Claus, Yunsie Chung, Zizhou (Joe) Zhao, Manuel Leyva, and Gina Zaghi. Not only did I learn from and was inspired by their work ethic and intelligence, I learned a great deal about myself through my interaction with them. I appreciate stimulating collaboration with Kamran Shavezipur and Ye Tian on several projects. I am glad to have had a pleasant and a lively desk neighbor, Lunet Luna. Ian Laboriante has been a great friend inside and outside the lab. I thank Carlo Carraro for his advice and scientific insight. I am appreciative of all group members I had the opportunity to interact with, Nicola Ferralis, Albert Gutés, Brian Bush, Greg Doerk, Guohua Li, Fang Liu, Ben Hsia, John Alper, Maxime Vincent, Wenjuan Gou, Junqin Zhang, Anahit Raygani, Alessandro Piotto, Nicolas Miani, Anna Harley-Trochimczyk, Peter Lobacccaro, Shuang Wang, Shuo (Steve) Chen, Candy Chang, Marco Tocchio, Mun Sek Kim, Nisha Mair, Ernest Chen, Brian Lee, Maxwell Fisch, Jiawen Hwang, Anton Suwandi, and Charles Dhong.

I feel privileged to have worked with Professor Ronald Fearing, a pioneer in the topic of the work presented here and his talented students Andrew Gillies and Paual Birkmeyer. I thank the Center of Integrated Nanomechanical Systems, its director Willi Mickelson, and all of its members, for broadening my perspective in the field of nanotechnology.

On a more personal note, I cherish the friendships I developed during my time in Berkeley. I thank Eli for convincing me to finally get a smartphone in the year 2014 (and his friendship). Kyunam, Jimmy, Chad, David, and Minsung have all enriched my life in different ways, and I am lucky to have such great friends. I am also lucky to have been roomates with Matt Pavlovich, Zach Baer, and Tom Dursch, who blessed me with 5 conflict-free years.

Finally, I must end the acknowledgment with the appreciation for my family. Not only have they been motivation to finish my study, they have qualities that I admire so much that it would not be an exaggeration to say that they have shaped me of today. My mom defines the word resilience, and her unwavering support made possible the life I have. My brother I always consider to be my more compassionate and optimistic half. I end this page remembering my dad, who I know would have been very proud.

Chapter 1

Introduction to gecko-inspired synthetic adhesive

1.1 Gecko adhesion

Over the last decade, geckos' remarkable ability to stick to and climb just about any surface found in nature has motivated a wide range of scientific interest in understanding the adhesion mechanism of their foot-pads [1-6], as well as interest in engineering gecko-mimetic surface for various applications [7-14]. The high adhesion and friction of its pads have been attributed to a complex array of hairy structures, which maximize surface area for van der Waals interaction between the toes and the counter-surface [1, 2]. As shown in Figure 1.1, the pads have a hierarchy of structures that cover various length-scales: the millimeter-sized lamellae layers, micro-sized setae hairs, and nano-scale spatulae that terminate in thin plates that are just a few nanometers thick.

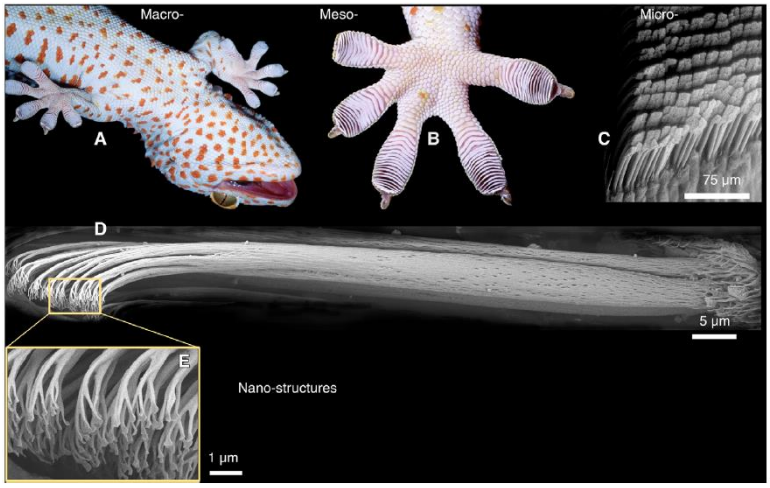

Figure 1.1: Hierarchical structure of gecko (A) foot-hairs, ranging from the mesoscale lamellae (B), microscale setae (C, D), and nanoscale spatulae (E). Reproduced with permission of Company of Biologists Ltd. from [3]. Permission conveyed through Copyright Clearance Center, Inc.

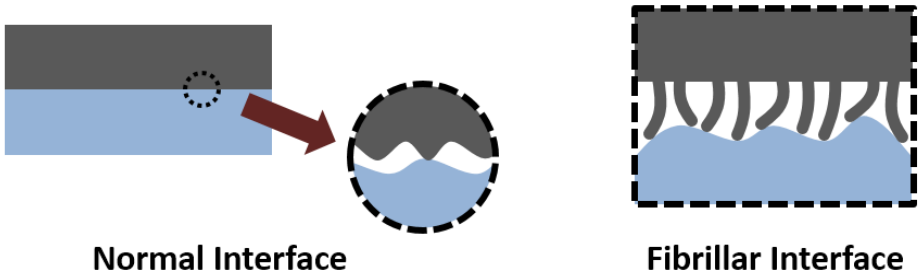

Figure 1.2: Comparison of a typical interfacial contact between solids where only a few contact are made (left) and a fibrillar interface where flexible fibers can bend to adapt to surface asperities (right).

Typically when two surfaces come to contact, the roughness on either surface allows only a few micro- or nano-scale asperities to come into contact (Figure 1.2 - left). While van der Waals force is universally present between any two surfaces, small surface area of real contact prevents any significant adhesion to occur on the macroscale. Conventional glue or tapes typically use viscoelastic layer to fill in the crevices between the surfaces, resulting in high real contact area [15]. In fibrillar adhesion by contrast (Figure 1.2 – right), flexible high-aspect-ratio elements bend to intimately contact the counter-surface to drastically increase the number of contact points, and thus maximize the van der Waals interaction force between the surfaces [16]. While van der Waals interaction is usually considered weak, the summation of force over numerous contact points can be surprisingly high. For a particular species Tokay gecko (*Gekko gecko*), each setal branch can produce adhesion on the order of 100 μN, and a pad area of 1 cm^2 can generate about 10 N [1], roughly equivalent to 1 kg object hanging off of the small area (a Tokay gecko typically weighs only a few hundred grams).

Several unique aspects of gecko adhesion are worth noting and have been summarized in detail by Autumn [17]. As mentioned, its toes consist of hierarchical structures ranging from milli- to nano-scale, allowing conformal adaption to various levels of surface roughness found in nature. The hairs also exhibit anisotropic behavior in attachment and detachment, where loading parallel to the surface results in engagement of fibers and thus high adhesion and friction, and unloading in a peeling motion allows disengagement with minimal force. Contrary to a common misconception that its "sticky" toes are the results of glue-like secretion or other soft material, the adhesion is dry and the hairs are actually quite rigid, made of β-keratin (estimated Young's modulus of $E \sim 2$ GPa), comparable in stiffness to human fingernail. Even though the material stiffness is high, the structural flexibility due to high aspect ratio gives rise to low effective modulus of the surface. Finally, as required for repeated use over many cycles, the hairs are durable and resistant to contamination. There is evidence that the hairs can self-clean even in absence of water, shedding any contaminants on contact with other surfaces.

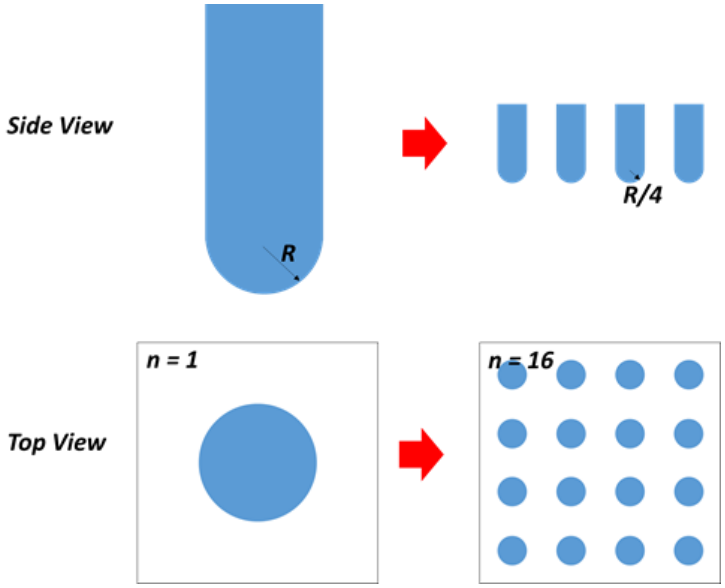

Figure 1.3: Schematically represented fiber element splitting into n number of finer elements. Because the radius scales with $1/n^{1/2}$ and the force scales with $n^{1/2}$, a higher number of smaller fibers have results in higher adhesion [4].

While the exact mechanism of gecko adhesion can be quite complex [4-6], the principle can be demonstrated by approximating the hair element with a cylinder terminated with a spherical tip (Figure 1.3) [4]. The van der Waals adhesion force between the tip and a flat surface is given by the Johnson-Kendall-Roberts (JKR) pull-off force equation:

$$F = \frac{3}{2}\pi W R, \tag{1.1}$$

where W is the adhesion energy per unit area between the two surfaces and R is the tip radius of curvature. As the fiber is divided into n number of smaller contacts in a given area, there is a corresponding change in the pull-off force:

$$F' = n\left(\frac{3}{2}\pi W R'\right) = n\left(\frac{3}{2}\pi W \frac{R}{\sqrt{n}}\right) = \sqrt{n}F \tag{1.2}$$

The simple relation shows that the as the contacts are split into finer elements, the van der Waals interaction force increases and scales with $n^{1/2}$. This contact splitting theory partially explains how fiber arrays can adhere strongly to surfaces, and why heavier animal like a gecko requires such small nanostructures in comparison to insects that also use hairy structures for adhesion (e.g., fly and spider) [4].

1.2 Potential applications of synthetic gecko adhesive

The unique adhesive characteristics of gecko toe pads have motivated researchers to create surfaces inspired by gecko adhesion, which have been termed gecko-inspired synthetic adhesive (GSA). Several application areas of gecko-inspired adhesive surface have been suggested or demonstrated as a proof-of-concept [17]. One use is as a substitute for conventional pressure-sensitive adhesives (PSA, e.g., Scotch tape, Band-Aid, etc.). Common PSAs leave residues after removal, and are often damaging to the surface, which are undesirable in many situations. This is particularly important for applications where cleanliness and preservation of the surface is critical, for example in fabrication clean-rooms for electronics and in medical application to skin. Although production of GSAs would be more costly in comparison to conventional PSAs, in such niche applications their advantage may be significant. In addition to being contamination and damage-free, reversible nature of GSAs would allow multiple uses.

There is also an active research in application of GSA as foot-pads for climbing robots [18-26]. Potentially reversible and versatile nature of GSA makes it ideal for this application since the foot-pads of robots have to be subjected to a large number of contact cycles and should provide adhesion to a variety of surfaces. While other adhesion mechanisms, such claws [27] or magnets [28], have been demonstrated, these mechanisms are specific to the surface on which they are compatible, whereas surface interaction via van der Waals attraction is universally present for all surfaces. Mimicking the directional adhesion of gecko pads can also potentially provide efficient detachment mechanism for minimizing the power requirement. Some climbing robots that use GSAs have demonstrated limited climbing capability on various surfaces. Such robots, if enabled to maneuver on all terrain with further development of GSAs, have potential applications in surveillance, environmental monitoring, and searching in places difficult to access.

High static friction of GSAs makes them potentially useful for applications where strong and non-slipping grip is required [17]. Numerous examples exist, for example grips for hand tools or sporting equipment, tires, gloves, and shoes. GSAs are unique in that the high friction is the result of van der Waals attraction between surfaces, in contrast to typical frictional interfaces where the asperities of rough surfaces resist shear movement against one another. Consequently, little or no normal load is required to achieve high friction with GSAs, and very high friction coefficient can be obtained.

The reversible and non-damaging nature of gecko attachment also makes GSAs ideal for transport mechanism for picking up and releasing objects. One particular study has demonstrated grabbing, transporting, and releasing of an LCD screen [29], which is promising for handling of various products where cleanliness is essential. Transport of particles has also been demonstrated,

where magnetically activated fibers can pick up particles in the adhesive mode and release them in the non-adhesive mode [30]. Such particle transport can be useful in cleaning of micro-particulates, e.g., on a wafer, which could be a way of avoiding expensive cleaning costs associated with some electronic components. Application to other common hand tools, such as tweezers or wafer handling wand, could also yield improved tools.

1.3 Survey of current synthetic gecko adhesives

Researchers over the last decade have produced numerous, increasingly complex GSAs with the aid of improving micro- and nano-lithographic techniques, which have been surveyed in numerous reviews [7-14]. As gecko adhesion requires flexible elements that can bend to intimately contact surfaces, synthetic gecko adhesives invariably involve fabrication of high-aspect ratio pillars or fibers in the micro- to nano-scale. While complete categorization is difficult due to a wide variety of GSAs, they can be roughly divided by the base material used to fabricate them: soft elastomer, thermoplastics, and carbon nanotubes.

Soft elastomers are typically a synthetic rubber material, and by far the most common material used for fabricating GSAs. Polydimethylsiloxane (PDMS), polyurethane (PU), and polyurethane acrylate (PUA) are some examples of such material used in the field [7, 8]. With low Young's modulus in the range of 0.1 – 100 MPa, they have several advantages in that the structures are flexible even at low aspect ratio, and that the contacts are soft enough to make conformal contact to many surfaces. The soft surface, however, is prone to contamination as adhesive contact can be made with unwanted particulates [30]. This limits the potential lifecycle of the tape, suffering the same shortfall of conventional PSAs that have limited number of usage. Additionally, low modulus material may have durability issues due to low material strength, which can lead to easy breakage or tear of the adhesive.

Thermoplastics have also been researched as a potential GSA material with higher modulus in comparison to soft elastomers [7, 8]. With Young's modulus in the range of 100 MPa to several GPa, the stiffness of this category of material is similar to that of natural gecko's. GSAs made from them have been shown to be less prone to contamination [30], suggesting longer lifetime and better reusability. Common thermoplastics such as polyethylene and polypropylene are widely available as films at low cost and easy to mold from templates by simple melting process, which can potentially aid in cheap production of the adhesives. However, higher modulus requires fabrication of higher aspect ratio fiber for sufficient flexibility for surface conformity, which can be costly. Thermoplastic fibers are also subject to plastic deformation that can limit the load beyond their yield strength [31].

Carbon nanotubes have also been researched as a potential GSA. While their high modulus (~1 TPa) requires very high aspect ratio structures, recent advances in bottom-up growth of carbon nanotubes have facilitated their fabrication [7, 9]. They have been demonstrated to have high adhesive strength, although the amount of force required to engage the fibers onto surface can be high because of stiffness of the tubes. They also suffer permanent deformation at high loading

similar to thermoplastics, and structural collapse of high aspect ratio tubes have been observed [32].

Advances in semiconductor processing to define template for molding elastomers or thermoplastic films, soft lithography techniques for pattern transfer, and nanowire growth processes (in particular for carbon nanotube adhesives) have facilitated fabrication of various adhesives mimicking some aspects of natural gecko fibers. While earlier efforts have mostly involved simple geometrical shapes like PDMS bumps [2], cylindrical thermoplastic fibers [33], or vertically aligned carbon nanotubes that demonstrated adhesive property [32], more complex aspects natural gecko fibers have been mimicked over time [7].

Angled fibers aligned in one direction have shown anisotropic adhesion, where attachment and detachment behavior differs depending on whether the loading direction was with or against the tilting direction of the fibers [34-41]. In addition to the loading direction, the tilting angle has been shown to affect the resulting adhesion behavior [41]. Such adhesive can be useful for applications where high adhesion is required during engagement in one direction, but easy release is immediately required afterwards by disengagement in the opposition direction, for example in climbing robots with quick, repeated attachment and detachment cycles.

An important characteristic of natural gecko fibers is the thin spatula tips that terminate the spatula stocks (Figure 1.1). These thin plates provide compliance at the nano-scale that allows conformal contact, and show that the tip shape of the contact elements can be important in providing high adhesion [42]. Many fabrication methods have been devised to manipulate the tip shape of the fibers [43-48]. Some simple structures consisting of a circular plate on top of cylindrical stock have been fabricated. The thin plate with a larger radius than the stock increases the area available for contact at the tip and better adaptability to surface roughness, showing improved adhesion in comparison to a cylinder [44, 47]. More complicated three-dimensional tip shapes have been fabricated [43], as well as asymmetrical tip shapes that add anisotropy to the adhesive [46].

Natural gecko fibers are multi-level structures, which aid their adaptability to surfaces that exhibit various level of roughness as would be expected in nature. Numerous fabrication schemes have been demonstrated for two- or three-level hierarchical fibers [29, 49-59]. Hierarchical structures have often shown worse adhesive performance than single-level structures due to a reduced number of contacting elements [7], but there is evidence of improved performance on rough surfaces [29]. The milli- or micro-scale base structures conform to correspondingly large surface asperities, ensuring that the smaller, micro- to nano-scale ends can make a high number of contact points for van der Waals interaction.

A study using a natural gecko setal branch has shown that gecko fibers have dry self-cleaning characteristics, where repeated contacts between contaminated fibers and a clean surface can lead to contamination transfer, effectively cleaning the adhesive pad [60]. Some GSAs have demonstrated similar characteristics [61, 62]. GSA contaminated by well-defined microsphere particles recovered adhesive property after repeated use, in contrast to conventional PSA that failed to do so [61]. Additionally, thermoplastic adhesives have shown to be more robust against contamination in comparison to those made from soft elastomers [62]. Wet self-cleaning GSAs,

where water can absorb surface contaminants and roll off, has also been shown to be an effective mode of self-cleaning [47, 63].

As briefly overviewed, there has been an impressive progress in regard to fabrication of new structures that mimic one or more aspects of natural gecko adhesion. However, limitation in lithography technology have prevented producing synthetic gecko adhesive that closely imitates the versatile and durable performance of natural gecko pads. Furthermore, adhesion and friction behavior of fibrillar surface is still poorly understood. Rather than focusing the entire effort on fabrication of structure that matches that of natural gecko, which would be costly in both research and in production, a more reasonable approach would be to study parameters that affect the interfacial behavior in order to aid in rational design. The next section will describe some of the challenges that need to be met in order to successfully replicate the versatile performance of natural gecko pads.

1.4 Current challenges of GSAs

Although many GSAs have shown adhesion and friction performance comparable to that of a natural gecko, almost all testing of GSAs has been done in ideal laboratory settings, in particular on smooth glass free of contamination [7-10]. Surfaces encountered in application present additional complications due to roughness, variation in surface energy, and contamination. On a smooth surface, all fibers on typical GSAs can easily contact the surface, but introduction of various levels of roughness have shown to dramatically reduce the adhesion or friction of GSAs [18, 29, 47, 50, 64]. Because most of surfaces encountered in applications have some level of roughness, GSAs must be improved to adapt to asperities on surfaces.

Glass is ideal for high adhesion because of its high surface energy. The higher the surface energy, the more thermodynamically unstable the surface, which results in stronger adhesion to another surface (in this case the contacting tips of the fiber structures) [65]. While metal and ceramics typically have high surface energy (several J/m^2 for a fresh cleaved surface, but closer to the order of 100 mJ/m^2 in a laboratory setting), many common surfaces (e.g., wood, painted wall, contaminated surface) have lower surface energy falling in the range of 30 – 60 mJ/m^2 [65-68]. Some hydrophobic surfaces, for example Teflon coating, can have surface energy below 20 mJ/m^2 [65]. To have a truly gecko-like adhesive, the GSA should be able to adhere to surfaces with a wide range of surface energy.

Other practical considerations include durability and contaminations during multiple use. While natural gecko foot-hairs can withstand thousands of step cycles without significant wear, limited testing has been performed on GSAs durability over repeated usage. Because reversible attachment is a key advantage of GSAs, durability remains an important issue. Surfaces in real application could also present various sources of contamination (dust particles, oily residues, etc.) that can degrade the performance of the adhesive over multiple cycles. While natural geckos have robust design against such contamination [60], limited studies have been done on GSA contamination and how to mitigate the issue.

It is worth noting that adhesive and frictional behavior of fibrillar surface is poorly understood. Effects of even the most fundamental parameters like the length and diameter of the fibers on fibillar adhesive have been a subject of debate, and limited experimental data exist [7]. Still less study has been done on rough and low-energy surfaces, even though they present critical challenges in application as mentioned. Finally, most experimental studies of GSAs have been performed with soft elastomers, which are adhesive without any high aspect ratio structuring due to the low Young's modulus. Thermoplastic materials that are closer to the stiffness of natural gecko hairs have not received as much focus, and they have potential to be true to the principle of gecko-like adhesive, where strong attachment is enabled by structuring the surface with compliant elements.

1.5 Outline of work presented

This dissertation presents fabrication and experimental study of the interfacial behavior of gecko-inspired thermoplastic fibrillar adhesives. Chapter 2 begins by describing the overall fabrication process, including the method to chemically etch silicon nanowire (SiNW) array, which serves as the molding template for creating thermoplastic replica that exhibit adhesive characteristics. The testing method to characterize the adhesive strength of the nanofibrillar surface will be explained, focusing on the friction force of macro-sized samples.

The next three chapters focus on better understanding a fibrillar interface by examining factors that critically affect the friction performance of the fabricated GSA. In Chapter 2, two basic fiber geometric parameters, length and diameter, are varied to study their effect on the macroscale friction of the fibrillar array and optimized for high friction on smooth glass. Chapters 3 and 4 investigate fibrillar friction on non-ideal surfaces, where lower surface energy and roughness will each be introduced in a controlled manner to provide insights on why GSAs often fail under these conditions.

The last chapter presents fabrication schemes for more complex fiber designs. For the chemical etching of SiNW template, various aspects of etching chemistry are explored to control the resulting SiNW morphology. Control over geometrical factors like aspect ratio, clumping, tapering, and directionality of the SiNW is presented. Fabrication of single-level fiber will be extended to produce hierarchical fiber designs, and composite fibrillar adhesive material composed of thermoplastic and soft elastomer is presented. A method to control the tapering of high aspect ratio structure is demonstrated, which allows fabrication of more complex shaped fibers. The dissertation concludes with future work to be done in relation to the presented work.

Chapter 2

Template fabrication and friction test setup

This chapter is reproduced in part with permission from: Y. Kim, R. K. Claus, F. Limanto, R. S. Fearing, R. Maboudian. Friction characteristics of polymeric nanofiber arrays against substrates with tailored geometry. *Langmuir* **2013**, *29*, 8395-8401 <http://pubs.acs.org/articlesonrequest/AOR-zasD6r7JwTvaZcEnujbF>; Y. Kim, F. Limanto, D. H. Lee, R. S. Fearing, R. Maboudian. Role of counter-substrate surface energy in macroscale friction of nanofiber arrays. *Langmuir* **2012**, *28*, 2922-2927 < http://pubs.acs.org/articlesonrequest/AOR-8mRysJmZEiGJ5335qbxK>; D. H. Lee, Y. Kim, R. S. Fearing, R. Maboudian. Effect of fiber geometry on macroscale friction of ordered low-density polyethylene nanofiber arrays. *Langmuir* **2011**, *27*, 11008-11016 < http://pubs.acs.org/articlesonrequest/AOR-JyXIubdUfFwS7RPMqJG8>. Copyright 2011, 2012, 2013 American Chemical Society.

A systematic study of fibrillar interface first requires a consistent micro/nano-fabrication method for defining a regular array of polymer fibers with control over important geometrical factors like fiber number density and aspect ratio. In comparison to direct patterning of polymer micro/nano-fabrication techniques of silicon are much more researched owing to its applications in areas such as integrated circuits, micro-electro-mechanical systems, and renewable energy devices. Therefore, it is a sensible approach to first define an array of high aspect ratio silicon structures, for example SiNWs, and transfer the pattern to a polymer by various molding processes. This is particularly useful for thermoplastics, since they can be easily molded from a template by a simple melting process. The following sections describe the process for fabrication low-density polyethylene nanofibers by molding from SiNW templates. A description of method for friction testing of the fabricated GSA is then presented.

2.1 Fabrication process overview

The fabrication process is shown in Figure 2.1 [69-71]. The procedure is first briefly described in this section, and the detailed explanation of significant parts of the process follows. The process begins by floating a monolayer of packed polystyrene (PS) microspheres on water and transferring it onto a silicon chip (typically 1 × 1 cm^2) or a wafer. Oxygen plasma is used to etch and

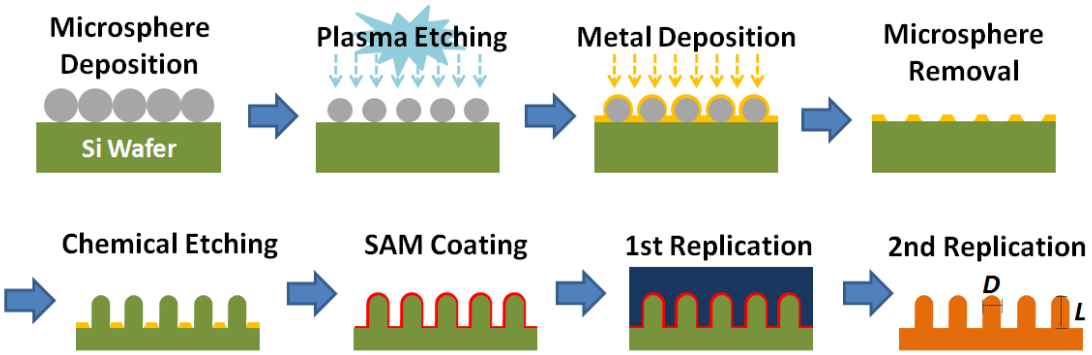

Figure 2.1: The process overview of low-density polyethylene nanofiber array fabrication. A close-packed monolayer array of polystyrene microspheres is deposited on a Si chip or a wafer, followed by size reduction by oxygen plasma. Deposition of Au and removal of the spheres produces a gold mesh film. Si is selectively etched in the region contacting Au, leaving a silicon nanowire array. A self-assembled monolayer coating allows the peel-off of the intermediate polycarbonate mold. After molding low-density polyethylene, the intermediate mold is dissolved away.

reduce the diameter of the microspheres and a thin gold film is subsequently evaporated onto the substrate. Sonication in deionized (DI) water removes the spheres and leaves behind the gold mesh defined by the holes where spheres masked the evaporation. The substrate is submerged in a chemical etch bath containing hydrofluoric acid and an oxidizing agent. The gold film acts as the catalyst for Si etching, resulting in the mesh etching down vertically to leave behind an array of SiNWs. An intermediate hole template is molded by melting a polycarbonate film against the SiNW, and separated by either peeling off or dissolving the silicon template. The final nanofiber array is molded by melting low-density polyethylene onto the polycarbonate template, and the intermediate is dissolved away in methylene chloride. In additional to allowing a consistent fabrication of thermoplastic nanofiber array, this process offers control over several important parameters. The spacing between the nanofibers is determined by the diameter of the deposited spheres, and the fiber diameter can be tuned by the duration of the plasma etching. The length is easily controlled by the reaction time in the etch bath. The final replication steps can be modified to produce fibers of various materials, by either curing synthetic rubber or melting thermoplastics.

2.2 Colloidal lithography

The first set of steps for deposition of colloidal particles aids the lithographic patterning of gold mesh by serving as the shadow mask during evaporation. This method, commonly referred to as colloidal lithography, avoids expensive patterning steps of conventional photolithography

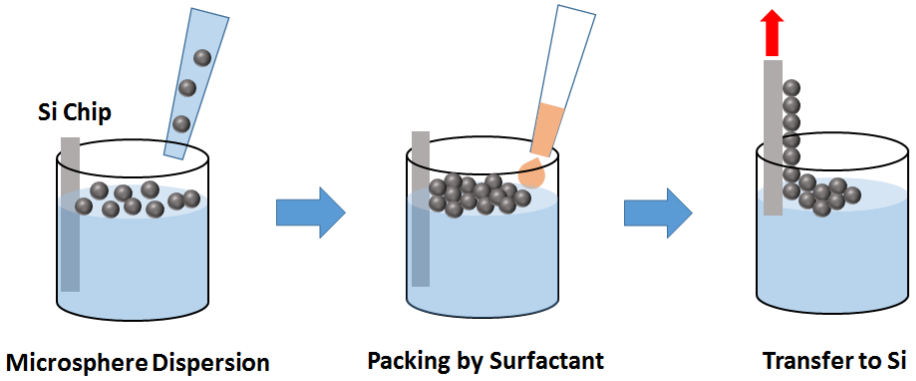

Figure 2.2: The procedure for depositing a monolayer of hexagonally-packed polystyrene microspheres. A water solution containing polystyrene is carefully introduced to water/air interface, where the spheres float. The spheres are packed by a small amount of surfactant, and subsequently transferred to a silicon chip/wafer.

and is especially useful for producing repeating patterns of small size [72]. To begin the procedure, a Si(100) wafer chip of ~1×1 cm^2 size or a wafer are cleaned by successive sonication in acetone and isopropanol for 10 min. each, followed by UV ozone cleaning for another 10 min. All Si substrate used are purchased from either Universitywafer (p-type, 1 - 30 Ω-cm) or Silicon Quest International (p-type, 10 - 30 Ω-cm). Cleaned Si substrate is thoroughly washed with deionized (DI) water (18 MΩ), then blow dried by N_2 gas. PS microsphere array is deposited on the Si substrate by a simple float and transfer technique, as shown in Figure 2.2.

Commercially purchased monodispersed microsphere solution (Duke Scientific, 10 wt% in water) is first diluted by DI water (to 2 wt%) and mixed with ethanol (1 : 1 volume ratio). The solution is carefully introduced with a pipet to a NaCl solution (~0.5 wt% in distilled water), which produces a disordered film of floating PS microspheres. PS pheres of a wide range of diameter can be floated (500 nm – 10 μm), but larger sized spheres require additional hexane layer on water bath to prevent a significant number of spheres from sinking into the bulk water. The floated spheres can be pushed into a close-packed monolayer film with the addition of a small droplet (a few μL) of a surfactant solution (sodium dodecylsulfate, 3 wt% in distilled water). The array is then transferred to the Si substrate by a micro-manipulating setup based on a stepping motor used for controlled motion of the substrate during immersion and withdrawals (~2 mm/sec). Close-packed PS microsphere arrays on Si surface could be obtained over a large area (up to 4" wafer-scale) as seen from the scanning electron microscope (SEM) image (JEOL JSM 6490LV, Agilent NovelX-MySEM, or LEO 1550 is used to take the SEM images presented throughout this dissertation) and a picture of the wafer covered by the monolayer (Figure 2.3 - left). While similar to the Langmuir-Blodgett trough method for depositing monolayers, this method uses a small amount of surfactant, rather than a mechanical trough, for packing the monolayer. After the

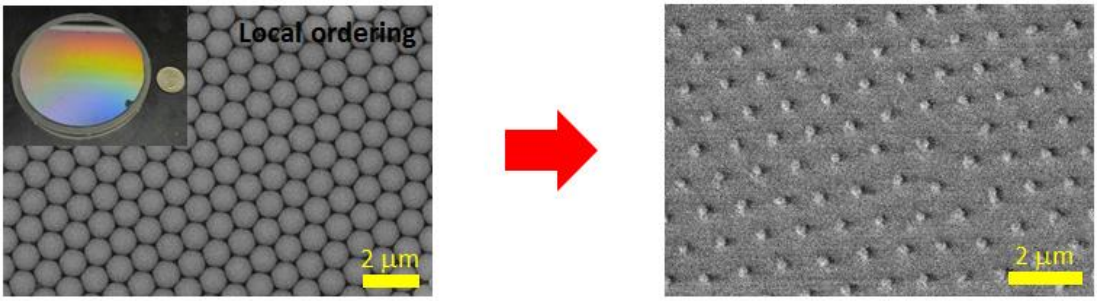

Figure 2.3: SEM images of microspheres in a hexagonal arrangement before oxygen plasma etching (left) and after oxygen plasma etching (right). Inset shows the spheres can be deposited on a 4" wafer scale.

deposition, the microspheres are reduced in size (Figure 2.3 - right) by oxygen plasma treatment, which produces a non-close packed array. For most of this work, the diameter of the deposited microsphere is 1 µm, also resulting in center-to-center spacing of 1 µm in a hexagonal arrangement.

2.3 Metal-catalyzed electroless etching of silicon template

This section contains material from the following publication with permission from the contributing authors: D. H. Lee, Y. Kim, G. S. Doerk, I. Laboriante, R. Maboudian. Strategies for controlling Si nanowire formation during Au-assisted electroless etching. *J. Mater. Chem.* **2011**, *21*, 10359-10363. <http:/dx.doi.org/10.1039/C1JM11164G>. Reproduced by permission of The Royal Society of Chemistry (RSC).

Once the spheres are reduced in size by plasma treatment (Plasma-Therm PK-12 RIE, 30 W, 100 SCCM), a thin layer of gold (20 nm) is evaporated (Thermionics VE-100) and the spheres are removed by sonication in DI water (any oxide layer formed during the processing is removed by 10 min of vapor HF exposure prior to evaporation and 5 to 10 min of liquid HF treatment after the sphere removal). This produces a gold mesh defined by the holes where spheres have initially been placed (Figure 2.4b). Gold is a catalyst in chemical etching of silicon by HF and an oxidizing agent, in this case hydrogen peroxide. While uncatalyzed Si etching in HF/H_2O_2 solution is rather slow, the electrochemical reaction is greatly accelerated in the presence of metal catalysts such as Au, Ag, and Pt, which are more electronegative than Si, where the metals can accept electrons from Si and donate electrons to H_2O_2. This etching is generally understood to be a localized electrochemical process, with the metal acting as a local cathodic site and the underlying Si as a local anodic site as follows [73]:

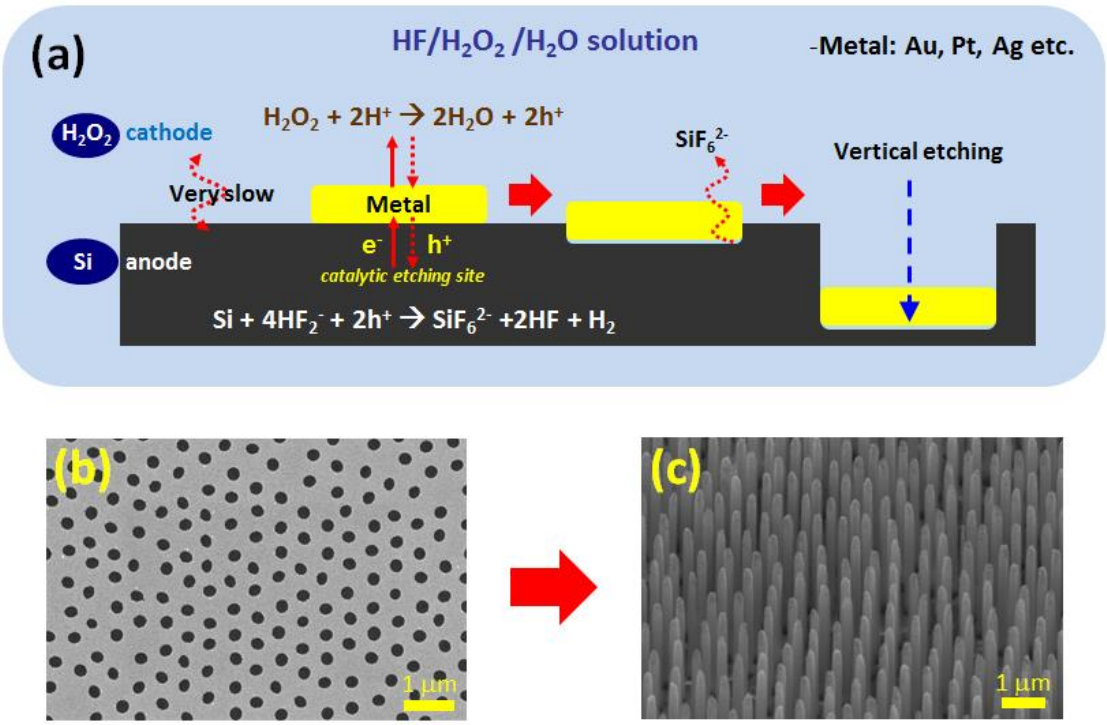

Figure 2.4: (a) A schematic of electrochemical etching of Si catalyzed by Au. While etching by HF and H_2O_2 is usually slow, Au facilitates the transfer of holes, and the etching preferentially occurs at the Si/Au interface. (b) An SEM image of Au film with exposed Si holes. (c) A SiNW array left behind after the Au mesh has been vertically etched down.

Cathode reaction (metal):

$$H_2O_2 + 2H^+ \rightarrow 2H_2O + 2h^+ \quad (2.1)$$

Anode reaction (Si):

$$Si + 4HF_2^- + h^+ \rightarrow SiF_6^{2-} + H_2 \quad (2.2)$$

During the reduction of hydrogen peroxide, holes (h^+) are generated and injected into Si, which induce oxidation of Si to SiF_6^{2-} in the presence of HF, followed by dissolution in aqueous solution (Figure 2.4a). Since electron and hole transport is highly localized near the metal/Si interface, etching of Si occurs mainly in the immediate vicinity of the metal particle, resulting in continuous

sinking of the metal and the formation of high-aspect ratio nanostructures [73]. In our case, the patterned gold mesh sinks down, leaving behind an array of silicon nanowires (Figure 2.4c).

Many factors affecting the final Si nanostructures have been studied such as the type of metal (e.g., Ag, Au, Pt), the HF and H_2O_2 concentrations, the substrate doping level, crystal orientation of the substrate, and etching temperature [73]. Later sections (6.1 and 6.2) will present variations in the etching conditions that critically affect SiNW morphology. For now, the etching bath consists of a fixed amount of HF (48 wt%, EMD), H_2O_2 (35 %, Fisher Scientific), DI water, and acetonitrile (Fisher Scientific) in the volume ratio 2:1:5:2, respectively, where acetonitrile is added as a wetting agent that improves the etching uniformity across the substrate. The total volume of solution is typically 10 mL for each 1 × 1 cm^2 chip, although the volume of solution has little effect on the etching behavior as long as enough reactants are present for the etching duration. This composition produces an array of vertical, untapered SiNWs, suitable as a template for molding a well-defined thermoplastic fiber array.

2.4 Nanostructure molding

The SiNW pattern is transferred to thermoplastic by simple vacuum molding steps. The gold catalyst layer is first removed by soaking in an aqua regia bath (a mix of 38% hydrochloric and 70% nitric acid in 3:1 volume ratio) for a few minutes. To aid the separation from the template, SiNWs are first treated by octadecyltrichlorosilane, a self-assembled monolayer easily prepared by reaction in the liquid phase. The substrate is submerged in a bath containing 1:1000 volume ratio of octadecyltrichlorosilane (Sigma-Aldrich) to toluene (Fisher Scientific) for 15 hr, which covers the surface of the SiNWs with a hydrocarbon layer. Typical solution volume is about 5 mL of toluene for each 1 × 1 cm^2. An intermediate hole template is molded by melting a polycarbonate film (McMaster-Carr, 100 µm thick) against the SiNW template in vacuum at 300 ℃ for 1.5 hr. Once cooled to room temperature, the film is mechanically peeled-off from the template. Alternatively in cases where peel-off is difficult due to high aspect ratio, Si template can be dissolved away with a silicon etchant (typically acidic solution containing HF and nitric acid). The nanofiber array replica is molded by melting low-density polyethylene (LDPE, McMaster-Carr, 100 µm thick film) into the polycarbonate template at 160 ℃ for 1 hr. Physical separation of the films at this point is undesirable due to plastic yielding of LDPE fibers. Instead, the polycarbonate intermediate is dissolved away in a methylene chloride (Fisher Scientific) bath for 1 hr, followed by additional soaking in methylene chloride for 10 min. An isopropanol rinse and N_2 blow drying complete the fabrication process. Representative SEM images of a template and the replicated LDPE fibers are shown in Figure 2.5.

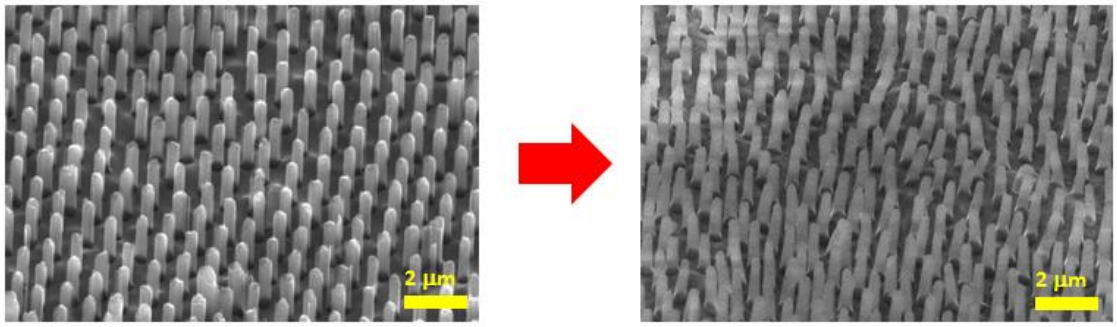

Figure 2.5: SEM images of Si template (left) and the replicated low-density polyethylene nanofiber array (right).

2.5 Friction testing setup

There are numerous ways to measure adhesive strength of a GSA, e.g., normal adhesion test, friction/shear adhesion test, and peeling test. The tests can be performed over a relatively large area (a few mm^2 to cm^2 patch area), or over some microscale contact zone [7]. This work focuses on macroscale friction measurements in which an adhesive patch of 1×1 cm^2 is tested, since this is a relevant patch size for many applications. As will be discussed later, friction of GSA is closely indicative of the adhesive strength because the main contribution to the friction is the van der Waals adhesion.

The schematic of the friction test setup is shown in Figure 2.6a. A 1×1 cm^2 fibrillar array film is brought in contact with the counter-surface with a rubber pad and a small normal load (10 g) on top. The purpose of the normal load is to ensure a consistent sample contact with the counter-surface for each test cycle, so that variation of friction due to film contact is minimized. The soft rubber layer helps distribute the load across the sample. After the sample is contacted, a shear load is progressively applied using a standard pulley setup with loading weight, and the static friction prior to detachment is measured and recorded. Thermoplastic adhesives typically exhibit training effects during repeated cycles [31], where the fiber and the backing film align with the counter-surface during shear loading. This often results in a gradual increase in friction over multiple testing cycles. Each sample has a limited lifetime, and the initial increase in friction is followed by a gradual decrease due to contamination and deterioration. A representative example of this behavior is shown in Figure 2.6b, where a sample increased in friction from 4 to 5.5 N, then decreased to 3.8 N over 13 testing cycles. For consistency, the maximum friction value obtained is taken as the friction value of that particular sample. Each friction data presented is based on measurements of at least 3 samples. To minimize contamination, the counter-surface is thoroughly washed with acetone, and the fibers with isopropanol, between each trial. Unless otherwise noted,

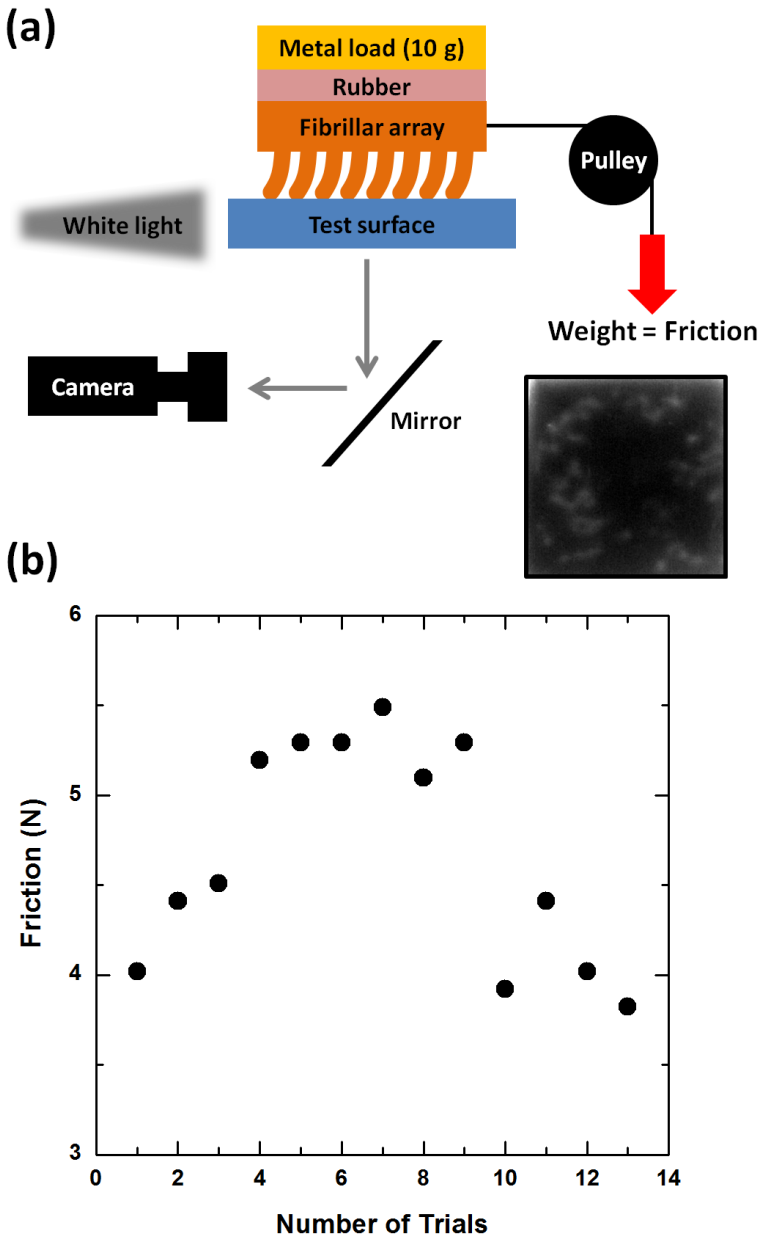

Figure 2.6: (a) A schematic of the testing setup for friction measurements. The beam of white light directed parallel to a transparent test surface creates a contrast between the contacting bright region and the non-contacting dark region (inset shown for a 1 × 1 cm^2 adhesive patch). (b) A representative friction data for one sample (the test surface is flat SiO_2). An increase in friction due to fiber and backing film alignment is followed by a decrease due to sample degradation. For each adhesive sample, the highest friction is taken as the final value for consistency.

the tests are performed in an ambient condition at 20 ℃ and 35% relative humidity.

The bottom portion of the setup (the white light, mirror, and camera) allows the observation of regions where the film is in actual contact with the counter-surface. Referred to as the frustrated total internal reflection method (FTIR), a beam of white light is directed parallel to a transparent substrate [74]. In presence of only glass/air interface, the light travels parallel to the surface, but when a glass/LDPE interface forms, the light is redirected to the normal direction, where a camera can record the resulting contrast between the contacting bright region and the non-contacting dark region. An example of this is shown in the inset of Figure 2.6a for a 1×1 cm^2 patch.

Chapter 3

Effect of fiber length and diameter on macroscale friction

3.1 Background

For GSAs there are only a few experimental reports [32, 75-78] on the effect of basic geometrical factors such as fiber diameter, length, and density on the macroscale adhesion and friction behavior. As reviewed recently [7] the basic issue of geometrical effect remains unclear, as there have been contradictory results regarding the effect of aspect ratio on the adhesion or friction of fibrillar surfaces. A systematic study has been reported by Greiner et al. [75], where increased adhesion for higher aspect ratio of cross-linked polydimethylsiloxane (PDMS) microfibers was attributed to larger elastic dissipation during the pull-off process. However, Glassmaker et al. [77] have shown that measured pull-off stresses of poly(vinyl-butyral) fibers were nearly independent of fiber lengths, though the energy dissipation increased linearly with increasing fiber length as expected due to the higher stored elastic strain energy in a single fiber.

In some cases, increasing aspect ratio was observed to decrease adhesion or friction. Burton et al. [76] measured the pull-off forces of poly(methylmethacrylate) and polyurethane acrylate nanofibers and reported lower adhesion for higher aspect ratio at various humidities. Zhao et al. [78] have reported a decrease in adhesive strength with increasing height of multi-walled carbon nanotube arrays which was attributed to the formation of canopy-like entangled surface layers as MWCNT fibers become longer. In contrast, Qu et al [32]. have more recently demonstrated a dramatic increase in adhesion and friction with increasing MWCNT fiber length. They have shown shear-induced alignment of top-entangled MWCNT fibers, which became more significant with increasing fiber length.

The goal of this chapter is to systematically investigate the effects of fiber geometrical factors, namely length and diameter, on their friction characteristics and to provide a useful reference for optimum conditions for high performance. To minimize complications from the substrates, smooth glass is used as the counter-surface. It is demonstrated that macroscale friction of these ordered nanofiber arrays is very sensitive to small changes in those parameter. A friction design map is presented by modifying the adhesion map previously reported [79], and a good agreement with experimental results is observed regarding the optimal geometry of the LDPE nanofibers.

3.2 Fabricated LDPE fiber arrays

As mentioned in Chapter 2, the fabrication method used allows precise control over the length (L) and diameter of the fibers ($D = 2R$). For this geometrical study, the initially deposited spheres are 1 μm in diameter (corresponding to fiber center-to-center distance of 1 μm), and the fiber diameter and length are in the range of 0.2 μm to 4.5 μm and 400 – 900 nm, respectively. Figure 3.1 shows representative images of LDPE nanofibers with various diameters and lengths.

3.3 Fiber clumping

As shown in Figure 3.1, with increasing fiber length, some of nanofibers start bending and contacting each other (referred to as the partial clumping regime, e.g., the third row for D ~ 600 nm); then all the nanofibers clump (all images on the 4th row) into bundles with further increasing length (referred to as the clumping regime). For the fibers contacting at their tips, a simple equation can be derived from Johnson-Kendall-Roberts theory of adhesion and elastic beam theory [80-82]:

$$L_{crit} = \left(\frac{\Delta R_t^{\,3} E}{W} \right)^{1/3}, \tag{3.1}$$

where L_{crit} is the maximum length before clumping, 2Δ the spacing between adjacent fibers, R_t the radius of curvature of the fiber tip, E the Young modulus (~200 MPa for LDPE [83]), and W (the adhesion energy of the fiber. The adhesion energy is twice the surface energy of LDPE ($W = 2*\gamma_f$ = 60 mJ/m^2 for LDPE [67]). As shown in Figure 3.2a, experimentally observed values in this study coincide reasonably well with the theoretical prediction, assuming that the tip radius of curvature is equal to the fiber stock radius ($R_t = R$). This is a reasonable approximation supported by the experimental observations shown in Figures 3.2b and c, where the tip-curvature of the nanofiber is measured from the side view SEM image (Figure 3.2b and c). This clumping behavior will later be discussed as a critical factor limiting friction performance of a fibrillar adhesive.

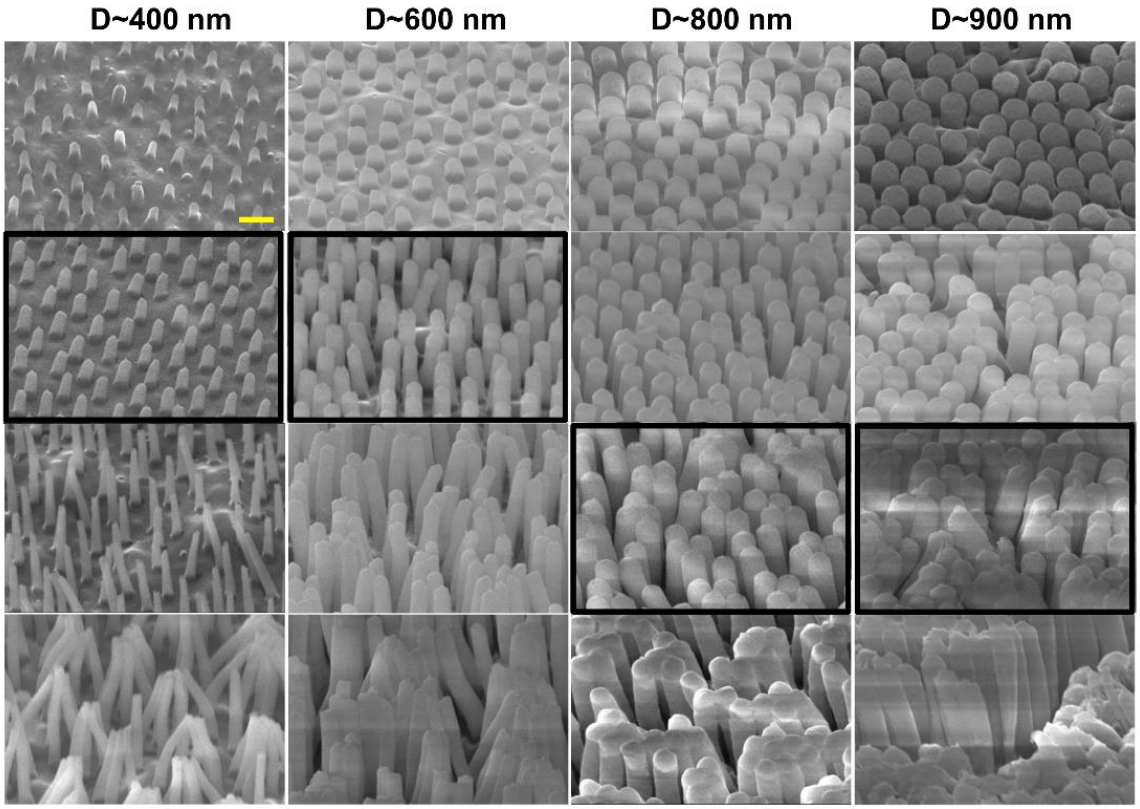

Figure 3.1: Representative SEM images of LDPE nanofiber arrays with increasing length down the row for each fiber diameter. Fiber clumping is observed above a certain critical length. The black outlines indicate the length at which the fibers exhibit the maximum friction for a given diameter. Scale bar = 1 μm.

3.4 Macroscale friction of LDPE nanofiber arrays

By the method detailed in Section 2.5, macroscale friction of 1×1 cm^2 fibrillar array film has been measured for the wide range of length and diameter, and the result is plotted in Figure 3.3a and b. At each diameter, a maximum friction force is observed with respect to the fiber length. This maximum point increases with diameter up to D ~ 800 nm, then decreases for D ~ 900 nm, indicating an optimum with respect to the diameter as well. The maximum friction observed (~6 N) is comparable to the adhesion of about 10 N for the same patch area of a natural gecko pad. The next sections will explain why such optimal behavior is observed for the fiber length and diameter, and how friction can be maximized by tuning the fiber geometry.

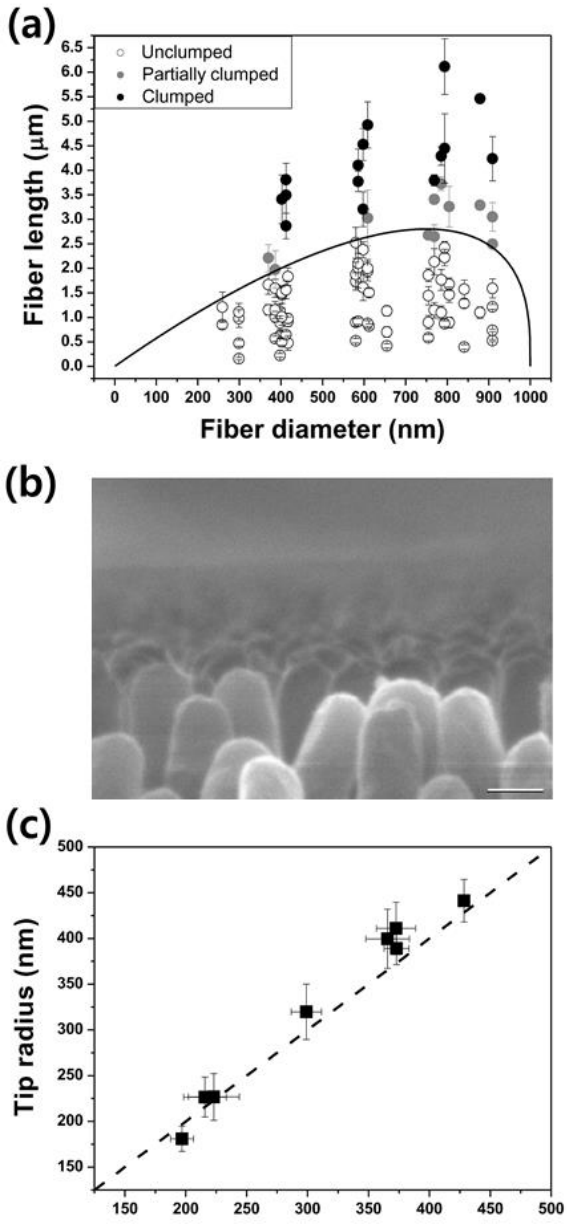

Figure 3.2: (a) Experimental observation of the length at which the fibers clump at a given diameter. The curve is the predicted clumping condition from Equation 3.1. (b) An SEM image of the cross-sectional view of the fiber array (~5° tilt) after cryogenic fracture in liquid nitrogen (scale bar = 0.5 μm). (c) Tip radius of curvature (R_t) measured from the cross-sectional view compared to the fiber radius (R). The data points fall near the $R_t = R$ line, indicating that two are approximately the same.

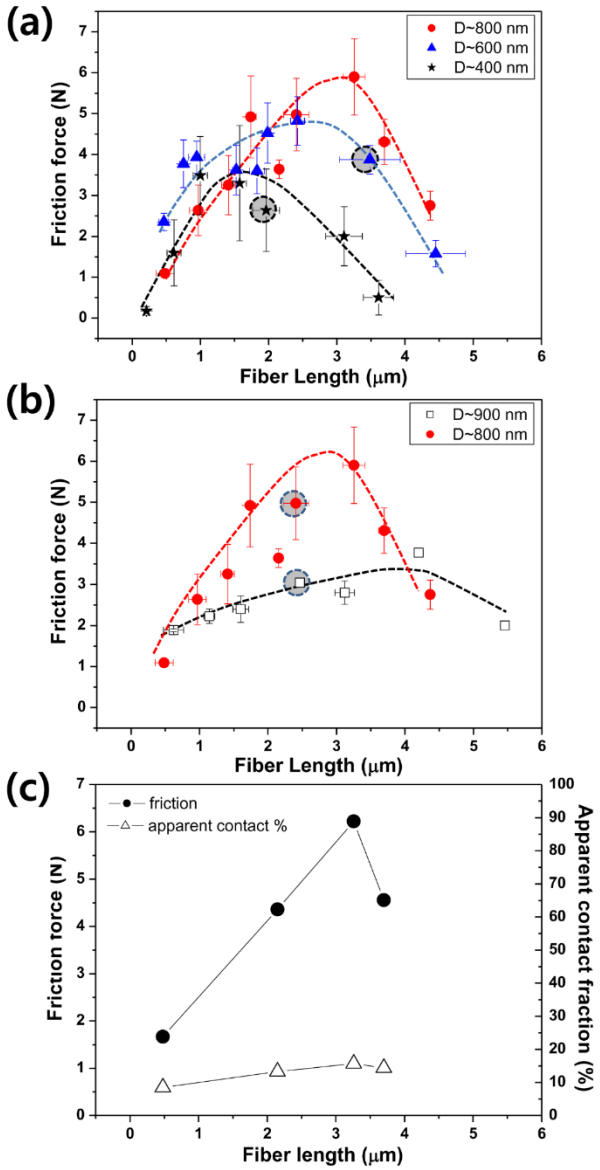

Figure 3.3: (a) Friction of LDPE nanofiber array (1 × 1 cm^2 patch) with various fiber diamters and lengths with fixed center-to-center distance of 1 μm. (b) The data set of D = 900 nm has been plotted separately with that of D = 800 nm for clarity. For (a) and (b) the lines are guides to the eyes, and the dotted circles indicate the points at which partial clumping is observed. (c) A representative plot of apparent contact area % (apparent contact area/test area × 100) with respect to the fiber length (for D = 800 nm). While ~6 fold increase of friction force is observed, the apparent contact fraction is not significantly altered between samples, typically 10 - 15% for all cases.

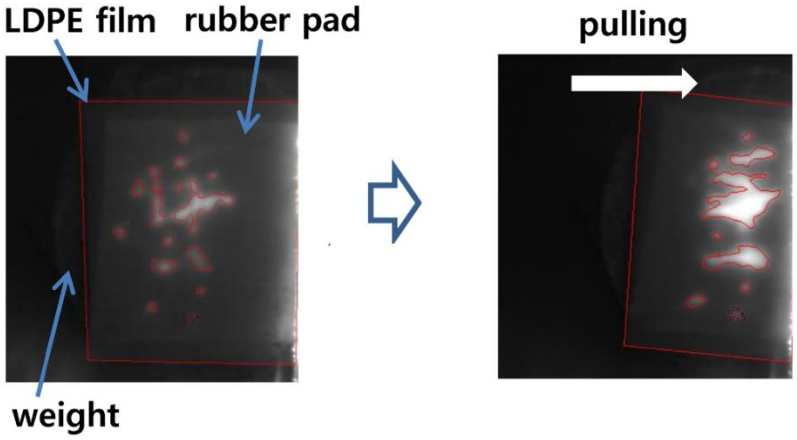

Figure 3.4: The apparent contact area indicating the portion of the film which is in actual contact with the glass from before being shear loaded (left) to just prior to being detached (right). The red square outlines the sample area (approximately 1 × 1 cm^2), and the contacting bright region is indicated with red outlines.

3.5 Apparent contact area

Before relating the nano-scale geometry of fibers to the macroscale friction of the array, it is important to note that not the entire film area is in contact with glass. Figure 3.4 shows the apparent contact area measured by the FTIR method, and it is observed that the contact is not uniformly distributed across the surface, but rather concentrated in the specific area with an irregular shape. The bright zone indicates that the contacting region increases from the initial to final state with a concomitant increase in brightness during the friction measurement.

Though non-contacting dark regions are clearly distinguished from contacting bright regions by this method, detailed micro-scale information inside the contact region is unknown. For example, the actual number of LDPE nanofibers in contact with the counter surface may be smaller than that estimated from the area defined by the bright region. It is noted that any difference in brightness may be influenced by the actual number of contacting nanofibers or by morphological change in contacting nanofibers, e.g., from tip to side contact. Thus, bright region is referred to as the *apparent* contact area. Despite the lack of detailed microscale information, it is useful for friction analysis in macroscale to visualize how the nanofiber contact is confined within this apparent contact area.

Since the static friction force is determined by the state just prior to sliding, the apparent contact area at this moment should be considered. It was found that this apparent contact fraction (f_{ca} = apparent contact area / test area × 100) was not significantly different between samples, typically 10 - 15% for the sample size of ~1×1 cm^2 as shown in Figure 3.3c, which is similar with the

previous results for polypropylene fiber arrays (~11%) [84]. Distributions of each data point in Figures 3.3a and b may reflect the variation in contact area for each test. Despite this distribution, it is clear that the measured friction forces are strongly correlated with the nanofiber geometry.

3.6 Friction prediction and dependence on fiber diameter from JKR model

In general, friction between surfaces can be modelled as the sum of two components as follows,

$$F = \tau A + \mu F_{\mathrm{N}}, \tag{3.2}$$

where τ is the shear strength coefficient, A is the real area of contact, μ the Coulomb friction coefficient, and F_{N} the normal load [85]. The first term is the area-dependent adhesive contribution to friction, while the latter is the load-dependent mechanical friction. In the limit that adhesion between two surfaces can be neglected (as is the case with many macroscale contact with few contact points), the equation reduces to the familiar linear relationship between the applied normal load and friction. In gecko adhesion, however, the adhesive term is likely to be the dominant contribution, due to the increased number of contact points. Applying the equation to a single fiber:

$$F_{\mathrm{f}} = \tau A_{\mathrm{f}} + \mu F_{\mathrm{N,f}}, \tag{3.3}$$

where F_{f}, A_{f}, and $F_{\mathrm{N,f}}$ are the friction, tip contact area, and normal load per fiber. The shear coefficient for LDPE-glass interface is 6 MPa [86]. The tip contact area can be estimated from the well-known Johnson-Kendall-Roberts (JKR) equation [80]:

$$A_{\mathrm{f}} = \pi\left[\frac{3\left(1-\nu^2\right)R_{\mathrm{t}}}{4E}\left(F_{\mathrm{N,f}} + 3\pi W R_{\mathrm{t}} + \sqrt{6\pi W F_{\mathrm{N,f}} R_{\mathrm{t}} + \left(3\pi W R_{\mathrm{t}}\right)^2}\right)\right]^{2/3}. \tag{3.4}$$

All the variables have been previously defined except the Poisson ratio (v ~ 0.4 for LDPE [87]), and the adhesion energy is $W = 2(\gamma_{\mathrm{f}}*\gamma_{\mathrm{g}})^{1/2}$, where the surface energies of the fiber (γ_{f}) and glass (γ_{g}) are ~30 and ~100 mJ/m^2, respectively [67, 68]. The second coefficient, μ, between LDPE and glass is 0.3 [86]. A 10 g (0.1 N) of normal load is applied to the 1 × 1 cm^2 patch, which contains approximately 10^8 fibers. However, only about 15% of film is in contact with glass, which corresponds to 7 nN of normal load per fiber. With all the terms now known, the adhesion contribution to friction is calculated to be 75 – 220 nN for the range of diameters tested (400 – 900 nm). Corresponding macroscale friction range is 1.1 – 3.2 N, which is a reasonable range of values compared to those observed in Figure 3.3a and b, although somewhat underestimated. The load-

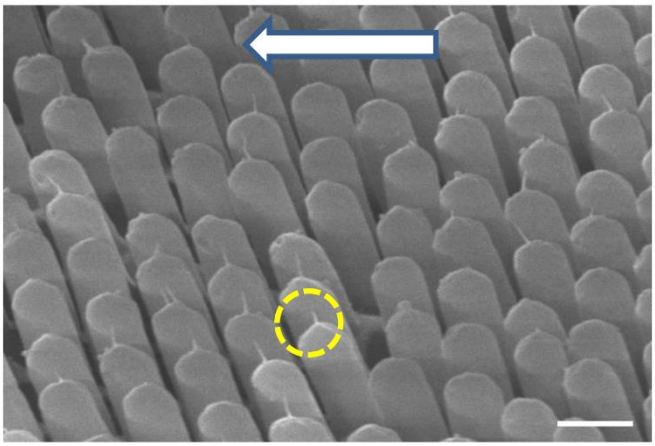

Figure 3.5: An SEM image of LDPE nanofibers after being friction tested. In some cases where the nanofiber array exhibited high friction, the fibers in the contacting region show permanent slating deformation with plastic yielding at the tip, indicating where the contact has been made (dotted circle). The arrow indicates the relative direction of shearing (by glass) at the tip. Scale bar = 1 μm.

dependent friction is only about 2 nN per fiber (0.03 N for the sample), confirming that this term contributes little to the overall friction of LDPE fibrillar adhesive.

Although the contact area analysis based on JKR theory gives a reasonable approximation as discussed above, it does not explain the complex behavior of friction forces depending on fiber diameter and length. Specifically, any variation in friction forces according to fiber length cannot be explained. Intuitively, lateral flexibility of the nanofibers may play significant role in friction, e.g., through further increase in contact area or fiber alignment during friction measurement. As mentioned, elastic dissipation and side-contact models have been typically considered for explaining changes in adhesion and friction with respect to fiber length (or more generally, aspect ratio). Elastic dissipation theory considers trapped and dissipated energy induced by fiber stretching in normal direction during the pull-off from the substrate [75, 77]. Thus, this theory explains only the effect of fiber geometry on normal adhesion, and is not directly applicable to frictional properties. On the other hand, side-contact models describe bending of sufficiently long fibers, which brings them into a stable side-contact with the opposing surface when adhesion is high enough to exceed the elastic bending forces [84, 88]. However, the SEM image of the fibers after friction testing (Figure 3.5) shows nanoscale plastic yielding at the fiber tips, which clearly indicates that the fiber contact is restricted to the tip. An approach developed to estimate the side contact length [84] predicts no side contact for all the geometries of LDPE nanofibers tested in

this study, which further supports that there is no side-contact induced by large bending of LDPE nanofibers.

3.7 Friction dependence on fiber length

In addition to the above explanation, small spacing between ordered nanofibers (2Λ = 1 μm – $2R$) would not allow a large bending for side contact. We suggest nanofibers have *slanted contacts* from fiber bending and alignment by shearing during friction measurement as illustrated schematically in Figure 3.6. Long nanofibers (b) are bent during the alignment by shear; thus they can more easily tolerate the nano-scale height distribution (distribution of nanofiber lengths) inside the apparent contact (bright) region, which further increases friction via increased number of contact points. Short nanofibers (a) are much less compliant, resulting in a lower number of contact points and thus lower friction. However, even long nanofibers cannot overcome the macroscale height variation of the backing film (as observed by bright and dark region in Figure 3.4), which results in a similar apparent contact area irrespective of the fiber geometry (Figure 3.3c). Further increase in fiber length (c) results in fiber clumping as discussed with Figure 3.2. In this case, significant a decrease in friction is expected by the engagement of several nanofibers into bundles that are not as compliant as individual nanofibers, as observed in Figures 3.3a, b.

The degree of height tolerance induced by the lateral bending of nanofibers may be approximated by the vertical displacement generated when the fibers are under a large deflection as a result of the shear loading. With the assumption of negligible load-dependent friction, δ_N can be obtained from an elastic beam model [89, 90]. As shown in Figure 3.7a, a beam of length L is subjected to a concentrated shear load F_f (friction per fiber) at the tip. Any position along the arc of the beam is denoted s, and $\varphi(s)$ the angle formed at the position with a vertical line. As such, the angle $\varphi(L) = \varphi_0$ is formed and the resulting vertical displacement is δ. This system can be described by $EI\varphi'' + F_f \cos\varphi = 0$, where $I = \pi R^4/4$ is the moment of inertia and φ'' is the second derivative respect to s, and simplifies to [89]:

$$L = \sqrt{\frac{EI}{2F_f}} \int_0^{\varphi_0} \frac{d\varphi}{\sqrt{\sin\varphi_0 - \sin\varphi}}, \tag{3.5}$$

Given the fiber length, the unknown angle φ_0 can be solved for numerically. Once the angle is known, the vertical displacement of the tip from the original position can be calculated by subtracting the vertical height of the fiber in the bent state from the height of the fiber in the upright state [89]:

$$\delta = L - \sqrt{\frac{2EI}{F_f}\sin\varphi_0}\,. \tag{3.6}$$

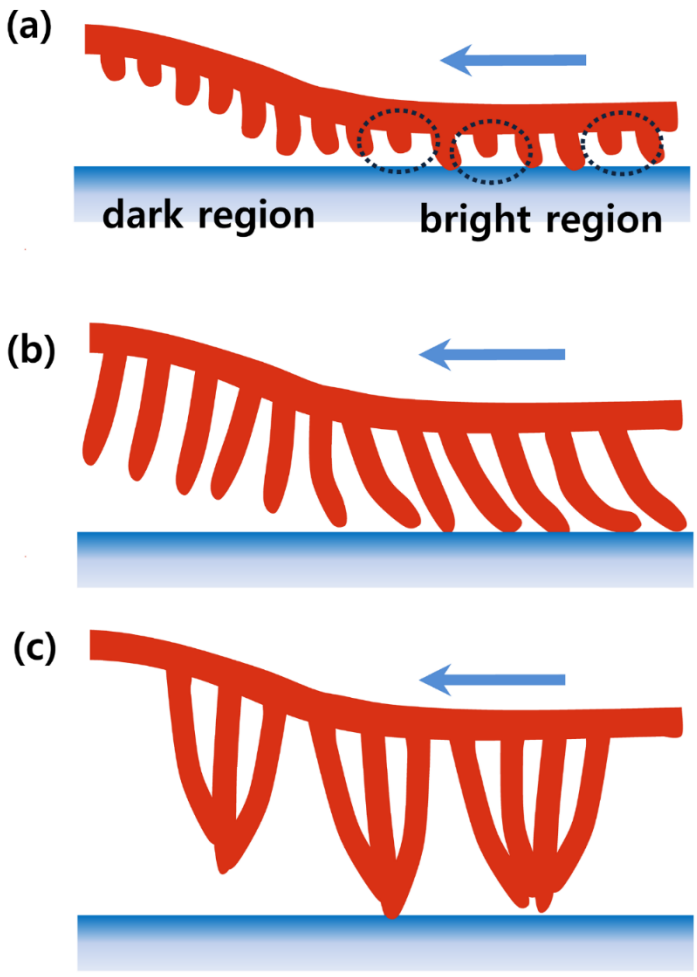

Figure 3.6: An illustration of the possible contact morphologies of nanofibers during the shear loading. (a) Within the contact portion of the film, short fibers are not flexible enough to adapt to any surface roughness or height variation in the array. No fibers are in contact in the dark region. (b) Long fibers can adapt better to increase the number of fibers in contact within the apparent contact area to increase the friction, but still unable to overcome any macroscale variation in film. (c) Clumping is detrimental to friction as the fibers lose flexibility and tips available for contact.

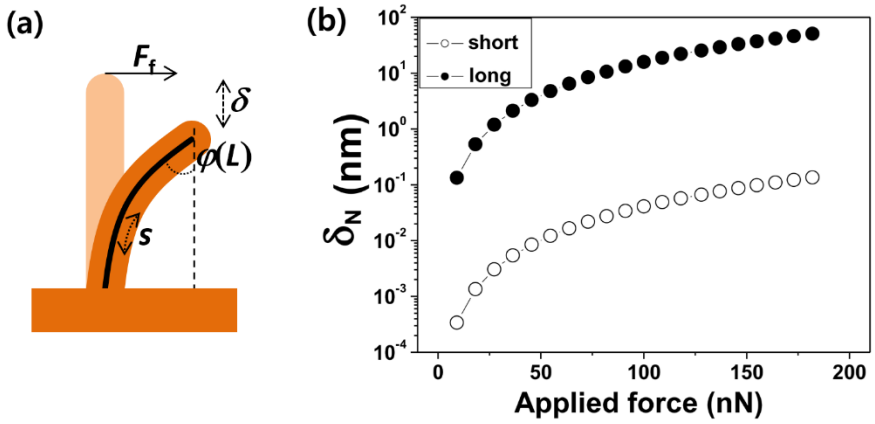

Figure 3.7: (a) A schematic showing the variables associated with the fiber bending. A shear force loaded at the tip (F_f) creates a vertical displacement (δ) and creates the angle φ along the arc s. (b) A comparison of δ with respect to the applied load for long (3.3 µm, close to the maximum friction) and short (1 µm) fiber with D = 800 nm.

Figure 3.7b is a representative result for D ~ 800 nm, which compares δ for short (1 µm) and long (3.3 µm) fibers when the applied force increases up to the theoretical friction force (F_f). Long nanofibers can have a significant normal displacement up to ~50 nm. Structural hindrance imposed by the fiber gap may make this value smaller, e.g., ~10 nm if the lower limit of δ is assumed to be given at a corresponding lateral displacement (δ_L) of 2Δ (i.e., at δ_L = 200 nm with D = 800 nm). Meanwhile, short nanofibers have only negligible δ value up to ~0.1 nm (corresponding δ_L ~ 15 nm). Note that the long nanofiber has much greater δ values than the short one by 2-3 orders of magnitude. While short nanofiber array detaches from the substrate by further increasing the load (i.e., exceeding the sum of the theoretical friction of all fibers in contact), long nanofiber array are able to withstand higher load by increased contact from neighboring nanofibers (which were not in contact previously) induced by this height toleration. Our previous discussion based on the schematics in Figure 3.6 is well supported by this explanation. This also suggests the increased brightness in the apparent contact area during friction measurement (Figure 3.4) is due to the increased number of contacting nanofibers. While this analysis is a helpful aid in relating the observed macroscale friction behavior to the mechanical behavior of the nanofibers, it is important to note its limitation. For example, the contact deformation of the fibers is accompanied by some degree of plastic yielding in addition to the elastic bending, which is not taken into account by the simple elastic model.

3.8 Optimum fiber length

As indicated in Figure 3.1 with black and Figure 3.3a and b with dotted circles, the fiber length at maximum friction (L_{max}) for a given fiber diameter is close to the fiber clumping condition (L_{crit}). As can be envisioned from Figure 3.6c, fiber clumping is detrimental to friction as also experimentally observed – maximum friction values for D ~ 400 and ~600 nm are obtained for the unclumped structures just prior to clumping (Figure 3.3a). However, it is interesting to note that the maximum friction forces for D ~ 800 and ~900 nm are observed for a partially clumped structure (Figure 3.3b). The morphology difference between unclumped and partially clumped nanofibers becomes less distinguishable as the diameter increases. Due to the narrow spacing between thick nanofibers, partially clumped nanofibers of large diameter are touching the neighboring fibers with only a small deflection, and many of the nanofiber tips are still individually exposed to contact the opposing surface (Figure 3.1, third row images for D ~ 800, 900 nm), which is not the case for smaller diameter fibers (Figure 3.1, third and fourth row images for D ~ 400, 600 nm). Since thick nanofibers are not as readily bent as thin nanofibers, increasing the fiber length into a slightly clumped state may still be helpful to obtain higher friction by achieving more compliance for bending to further tolerate the height distribution and maximize the number of contacts. Further clumping into the bundled structure with increasing length causes drastic decrease in the fiber compliance, and friction decreases as observed.

3.9 Optimum fiber diameter

As seen in Figures 3.3a and b, friction forces at L_{max} increase with diameter up to ~800 nm, but decrease for ~900 nm. This is contradictory to JKR analysis which predicts increased friction for larger diameter. This can be understood by extending our previous explanation based on fiber bending and height tolerance: though larger fiber diameter increases the tip-contact area, it will concomitantly decrease the gaps between fibers, which results in geometrical hindrance for lateral fiber bending with enhanced tendency for clumping. Thus, decreased friction for D~900 nm can be attributed to the reduced height tolerance due to restricted lateral bending of nanofibers.

Based on our results in this study, it is found that the optimum geometry of LDPE nanofiber arrays for macroscale friction is D ~ 800 nm and L ~ 3 μm with slight clumping, representing a compromise between the tip contact area and the fiber compliance. It should be noted that this structure is optimal for the specific case of having a flat glass as the counter-surface. The optimum geometry could be different for rough surfaces for example, possibly with a smaller diameter and larger spacing to tolerate a wider height distribution of the rough substrates.

3.10 Comparison with theoretical friction design map

Spolenak et al. [79] have proposed theoretical adhesion design maps for GSAs by considering conditions that limit the adhesive performance, such as fiber fracture, ideal contact strength, fiber clumping, and surface adaptability. The design map quantifies these criteria with respect to the fiber radius (R) and the material modulus (E), so that a failure of fibrillar adhesive can be avoided with proper geometrical and material considerations. It would be useful to see where the nanofibers in this study are located in the design map. For this, a *friction design map* was developed by modifying the equations used in Ref. 78 so that friction can be taken into account instead of normal adhesion. The development of a friction design map by modifying the criteria from the adhesion map is as follows.

- *Fiber fracture*

Fibrillar adhesive can fail by fiber fracture, when the applied stress on the fiber exceeds the fracture strength of the material. The friction stress exerted on a single fiber (σ_f) can be expressed as:

$$\sigma_f = \frac{F_f}{\pi R^2} \cong \frac{\tau A_f}{\pi R^2} = \frac{\tau}{R^2}\left\{\frac{9\pi R^2 W(1-\nu^2)}{2E}\right\}^{2/3} \le \sigma_{f,th}, \tag{3.7}$$

where the friction force (F_f) is the adhesive friction from Equation 3.3 at zero normal load and $\sigma_{f,th}$ is the theoretical fracture strength of the fiber based on the fiber radius (R). If the bulk shear strength is approximated to be similar with tensile strength (~E/10), the above condition is rearranged as:

$$R_{fracture} \ge \frac{10^{3/2}\tau^{3/2}}{E^{5/2}}\left(\frac{9\pi W(1-\nu^2)}{2}\right). \tag{3.8}$$

- *Ideal contact strength*

An adhesive contact cannot be stronger than its ideal contact strength. Since the stress concentrated on the actual contact area is considered as the ideal contact strength (σ_c), the limiting condition simply reduces to the maximum allowed τ as:

$$\sigma_c = \frac{F_f}{A_f} = \frac{\tau A_f}{A_f} = \tau \le \sigma_{c,th}\left(=\frac{W}{b}\right), \tag{3.9}$$

and thus:

$$\tau \le \frac{W}{b}, \tag{3.10}$$

where b is the characteristic length of surface interaction. The above condition sets a maximum parameter value that can be used for τ, which is well above typical τ values [86], for example, $W / b \approx (0.1\ \text{N/m}) / (2 \times 10^{-10}\text{m}) = 500$ MPa.

- *Fiber clumping*

As discussed in Section 3.3, adhesive can fail when a significant number of fibers clump into groups. Equation 3.1 is used for the clumping condition, which is rearranged into

$$R_{\text{clumping}} \le \sqrt{\frac{1}{4\rho_N}} - \frac{8W\lambda^3}{E}, \tag{3.11}$$

where ρ_N is the fiber number density (~10^8/cm^2) and $\lambda = L/2R$ is the aspect ratio. It is noted that the number density is used instead of the area fraction used in the previous study [79]. Since the number of fibers per unit area is fixed with the center-to-center distance of ~1 μm (area fraction is changed with respect to fiber diameter), the number density is used for comparing the nanofiber geometry.

- *Adaptability*

The reduced material stiffness due to the fiber elements has been described as the effective modulus [16], which is closely related to the ability of the fibers to conform to surfaces for adhesive contact. The effective elastic modulus (E_{eff}) for vertical fibers can be expressed as:

$$E_{eff} = CE\frac{\rho_N R^2}{4\lambda^2}, \tag{3.12}$$

where C is a geometrical factor (typically ~10) [16]. The adaptability condition becomes:

$$R_{\text{adaptability}} \le \sqrt{\frac{E_{\text{eff}}}{E}\frac{4\lambda^2}{C\rho_N}}. \tag{3.13}$$

E_{eff} needs to be arbitrarily chosen to ensure the contact adaptability, which will depend on the surface roughness.

It is noted that apparent contact strength (σ_{app}, this is the strength of the adhesive for a given patch area) increases with increasing fiber diameter in this study under fixed fiber number density, different from the previous report [79] where larger diameter fibers mean lower number density under fixed area fraction. σ_{app} can be written as:

$$\sigma_{app} = \frac{F_f}{A_{app}} = \rho_N \sigma_f \pi R^2 = \pi \rho_N \tau \left(\frac{9\pi R^2 W(1-\nu^2)}{2E} \right)^{2/3}, \tag{3.14}$$

which gives R as the following form:

$$R = \left\{ \frac{2E}{9\pi W(1-\nu^2)} \right\}^{1/2} \left(\frac{\sigma_{app}}{\pi \tau \rho_N} \right)^{3/4}. \tag{3.15}$$

The friction design map can be obtained by drawing Equations 3.8, 3.11, and 3.13 with a set of apparent contact strength values from Equation 3.15. Figure 3.8 shows the friction design maps for three different aspect ratios. For this design map, E_{eff} was set at 5 MPa based on the estimated E_{eff} values from Equation 3.12 which are 1 – 10 MPa at maximum friction condition ($L = L_{max}$) corresponding to different diameter fibers. In Figure 3.8a, for a low aspect ratio ($\lambda = 1$), it can be seen that most of short nanofibers are out of the optimum region limited by the surface adaptability (R should be less than ~100 nm to be in the optimum region). This indicates that less stiff material than E ~ 200 MPa is desired to ensure the contact for low aspect ratio geometry. For higher aspect ratio at $\lambda = 4$ (a typical value at $L = L_{max}$) in Figure 3.8b, most diameters are within the optimum region while achieving a maximum friction stress up to ~200 kPa by increasing the diameter to ~700 nm. This is quite similar to the experimental values, that is, the friction stress for the actual contact friction of 15% is ~5 N/0.15 cm^2 ~ 300 kPa. Further increasing the diameter along the E = 200 MPa line is limited by the fiber clumping condition. This indicates that the design map in Figure 3.8b also predicts the existence of optimal diameter at ~700 nm according to the fiber clumping condition. Further increasing aspect ratio ($\lambda = 7$) results in exclusion of all nanofiber geometry out of the optimum region by the clumping limit, which is reflected by experimental observation that friction decreases for clumped nanofiber bundles.

As discussed above, experimental results show that a slightly higher aspect ratio above the clumping condition, i.e., partial clumping, is allowed to achieve higher friction for larger diameters. This may indicate that the clumping limit needs to be less strict, allowing some range rather than a fixed value. For example, if the red line (clumping limit line) in Figure 3.8b is allowed to slightly shift upwards, increasing fiber diameter (along the E = 200 MPa line) to achieve higher friction is bound by the surface adaptability limit rather than the clumping limit, as experimentally shown by partially clumped structures exhibiting maximum friction forces (D ~ 800, 900 nm). Although the friction design map in Figure 3.8 is based on simplified models, it successfully describes the optimum geometry of LDPE nanofibers observed, and thus appears useful as a design guide.

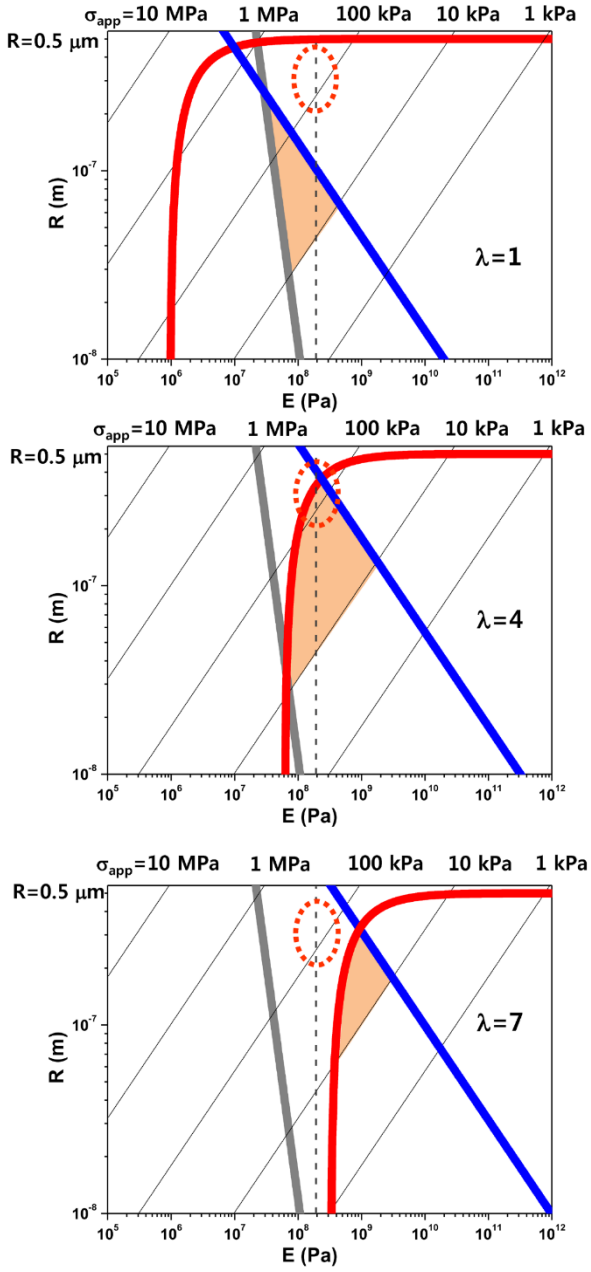

Figure 3.8: Friction design maps for LDPE nanofibers for three different aspect ratios (λ = 1, 4, 7). E_{eff} = 5 MPa was chosen for the surface adaptability limit. Shaded regions enclosed by three lines (gray: fiber fracture limit, red: fiber clumping limit, blue: adaptability limit) in each figure define the optimum design area to achieve at least 10 kPa of friction stress. Dashed line indicates E = 200 MPa. Dotted circles indicate the experimental region in this study (fiber radius, R ranges from 200 to 450 nm along the E = 200 MPa line).

3.11 Summary

This chapter examined the effect of two basic geometrical parameters of fibers, length and diameter, on macroscale friction of a fibrillar array. The experimentally observed dependence of friction on the two parameters was explained by simple JKR and elastic beam models, which indicated that increasing diameter increased available tip contact area, while increasing length facilitated the fibers to contact counter-surface by increasing compliance. Because fiber clumping limits the aspect ratio, the optimum geometry for macroscale friction against a flat glass substrate was found at D ~ 800 nm and L ~ 3 μm with slight clumping, which represents the optimum compromise between the tip contact area and compliance. A friction design map was developed based on the adhesion map previously reported, and the predicted optimum region marked on this map was found to be in a good agreement with the experimental observation.

Chapter 4

Effect of counter-substrate surface energy

4.1 Background

As briefly introduced in Section 1.4, one of the limitations faced by current GSAs is that they have mostly been tested on smooth glass, which is particularly suitable for high adhesion and friction due to its high surface energy. Since it is critical for GSAs to perform on a wide variety of surfaces as the natural gecko foot does, the role of counter-substrate surface energy in adhesion and friction remains an important issue. Only a few experimental studies have compared adhesion or friction of fibrillar surface against substrates with different surface energies. Autumn et al. [2] reported similar shear stress of a gecko seta on hydrophilic oxidized Si and hydrophobic GaAs surface, which they indicated as an evidence that capillary force does not play a significant role in fiber adhesion. Huber et al. [91] reported significantly higher pull-off force for an individual gecko spatula against glass in comparison to silicon wafer treated with hydrophobic monolayer at various relative humidities, and concluded that the pull-off force is controlled by short-range forces with capillarity contribution due to adsorbed water layer. However, Puthoff et al. [92] later reported that the material property change of the foot-hairs due to humidity may be responsible for the change in the observed adhesion, rather than any significant capillarity contribution. Ge et al. [93] showed that for their carbon nanotube-based synthetic adhesive, shear force was similar against substrates with varying surface energies, but the peel-off strength was correlated with surface energies.

While it is difficult to directly compare such experiments due to variations in the adhesive design and testing method, it seems that the quantitative role of counter-substrate surface energy on the performance of GSA's is unclear. This chapter provides some insights on this issue by testing the LDPE fibrillar adhesive against substrates with a wide range of surface energies. Glass

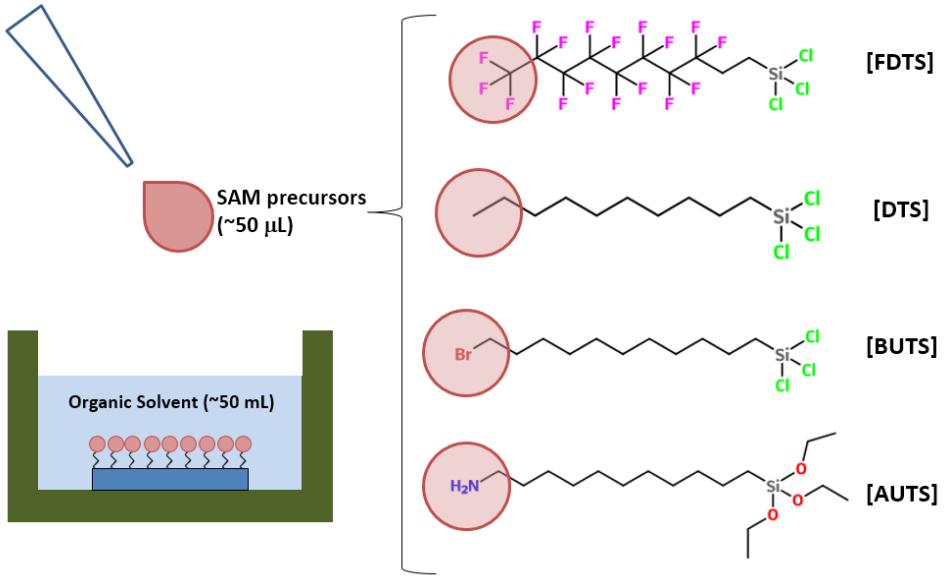

Figure 4.1: Chemical structures of four self-assembled monolayer precursors used for modifying glass. Fluorinated (FDTS), hydrocarbon (DTS), brominated (BUTS), and amine-terminated molecules are chosen so that the exposed end (indicated by the circle) can exhibit a wide range of surface energy. All coatings are performed by reaction in the liquid phase, where the silane end attaches to the glass.

surfaces treated by commercially available self-assembled monolayer (SAM) with various terminal groups are used as test substrates. Friction data are discussed in the context of simple theoretical models relating the substrate surface energy to fibrillar friction.

4.2 Counter-substrate preparation

For a systematic study relating to the surface energy, the substrate must be modified chemically without a significant change in the roughness and modulus. SAM deposition is appropriate since a monolayer thin molecular coating can alter the surface energy drastically with minimal impact on the surface morphology. As shown in Figure 4.1, a SAM precursor typically consists of an attachment end that covalently bonds to a substrate (the trichloro- or triethoxysilane end), and an exposed end responsible for altering the surface energy of the substrate (in red circles). For glass (SiO_2), common precursor molecules are long-chained silane molecules. Four precursors are chosen to cover a wide range of surface energy: 1H,1H,2H,2H-perfluorodecyltrichlorosilane (FDTS), n-decyltrichlorosilane (DTS), 11-bromoundecyltrichlorosilane (BUTS), and 11-

Table 4.1: The terminal group, contact angle, and the reported surface energies [taken or deduced from Refs. 94 and 95] of untreated glass and glass modified by 11-aminoundecyltrichlorosilane (AUTS), 11-bromoundecyltrichlorosilane (BUTS, Gelest), N-decyltrichlorosilane (DTS), 1H,1H,2H,2H-perfluorodecyltrichlorosilane (FDTS).

Substrate	**Terminal Group**	**Contact Angle**	**Surface Energy (mJ/m^2)**
Untreated Glass	SiO_2	<10°	100
AUTS-treated	$-NH_2$	75°	45
BUTS-treated	-Br	90°	30
DTS-treated	$-CH_3$	107°	25
FDTS-treated	$-CF_3$	112°	15

aminoundecyltriethoxysilane (AUTS). To minimize any difference between the treated substrates other than the exposed functional group, all selected precursors have been chosen to have a similar chain length (10 to 11 carbons).

The surface treatment procedure is as follows. Glass slides (Fisher Scientific) are successively sonicated in acetone and isopropanol for 10 min each, then cleaned in boiling Piranha solution (3 : 1 ratio of 97% H_2SO_4 and 35% H_2O_2) for 30 min. The cleaned glass is submerged in a coating bath containing the silane precursor and organic solvent in 1:1000 volume ratio (50 µL : 50 mL) in a nitrogen environment with less than 5% relative humidity. The organic solvent used and the reaction time varies depending on the precursor. 1H,1H,2H,2H-perfluorodecyltrichlorosilane (Alpha Aesar) is deposited in 2,2,4-trimethylpentane (EMD) for 1 hr. n-decyltrichlorosilane (Gelest) and 11-bromoundecyltrichlorosilane (Gelest) are deposited in toluene (Fisher Scientific) for 2 hr and 1.5 hr, respectively. 11-aminoundecyltriethoxysilane (Gelest) is deposited in chloroform (Fisher Scientific) for 1 hr. After the deposition step, the substrates are sonicated for 10 min in fresh baths of respective solvents, followed by another 10 min in isopropanol. Finally, they are post-baked at 130 ℃ in ambient pressure for 30 min.

Water contact angle is a good indication of how well the surface has been modified by the monolayers. Static contact angles have been measured with 3 µL drops of deionized water using a tensiometer (Ramé-Hart Model 290). Table 4.1 summarizes the water contact angles of glass substrates modified by monolayers with various terminal functional groups. A good agreement with contact angles reported in the literature suggests that the glass surfaces have been successfully modified with monolayers, and the surface energy values are those typically reported in the literature [94, 95] for the corresponding exposed functional groups. Topographical measurements

by atomic force microscope (Digital Instrument Nanoscope IIIa, measured over 10 × 10 μm^2 area) showed that all treated substrates had root mean squared roughness between 1 - 2 nm, which is in the range of roughness of the untreated glass surface, indicating that negligible change in substrate roughness occurred by the SAM treatment.

4.3 Friction and surface energy of counter-substrate

The friction of LDPE fiber array against the SAM-treated surfaces has been measured by the method presented in Section 2.5. The geometrical parameters of the array are fixed at *D* (diameter) = 2*R* = 600 nm, *L* (length) = 2.5 µm, and the center-to-center distance of 1 µm, corresponding to ~1.0×10^8 fibers/cm^2. Figure 2a shows static friction of LDPE nanofiber arrays on the five substrates of varying surface energies. The samples show high friction (~9 N) on untreated glass. The significant improvement of friction on the untreated glass in comparison to the previous set of data in Chapter 3 is likely due to improvement in fabrication procedure, in particular peeling the polycarbonate template off the silicon template, rather than dissolving the silicon template with possible damage to the polycarbonate film. Only a minor drop in friction (to ~8.5 N) is observed on AUTS-treated glass despite the large change in the observed contact angle of the substrate. However, a drastic drop in friction is observed for even lower surface energies, leading to a poor performance on hydrocarbon (DTS) and fluorocarbon (FDTS) monolayers. While the friction values on these two surfaces are quite similar, FDTS surface seems to exhibit a slightly higher friction. AFM-based sliding friction measurements have reported higher values against fluorocarbon monolayer than against hydrocarbon monolayer [96]. Similar phenomena may be occurring in our case with some of the fibers sliding against glass. Figure 4.2b shows the corresponding apparent contact fraction of the ~1 × 1 cm^2 just prior to sliding, simultaneously observed during the friction measurements. As shown, the apparent contact fraction does not deviate significantly between substrates from the average value of ~17%, and therefore cannot account for the large change in friction.

One possible explanation of the observed disparity in friction is that the water meniscus formed from the environment (RH ~ 35%) increases the interaction between the sample and high surface energy, thus hydrophilic, substrates. It has already been suggested that humidity can play a significant role in fibrillar adhesion, either from capillary effect [76, 91, 97] or change in viscoelastic properties of the material [92]. In either case, increasing adhesion is expected with increasing relative humidity. However, the same friction measurements repeated for hydrophilic glass in a low humidity environment (RH < 5%), as shown in Figure 4.2c, resulted in similar friction, indicating that the humidity effect in our case is not significant.

With insignificant capillarity contribution in the testing condition, the friction of a single fiber can be estimated in the same manner as presented in Section 3.6:

$$F_f = \tau A_f + \mu F_{N,f}, \tag{4.1}$$

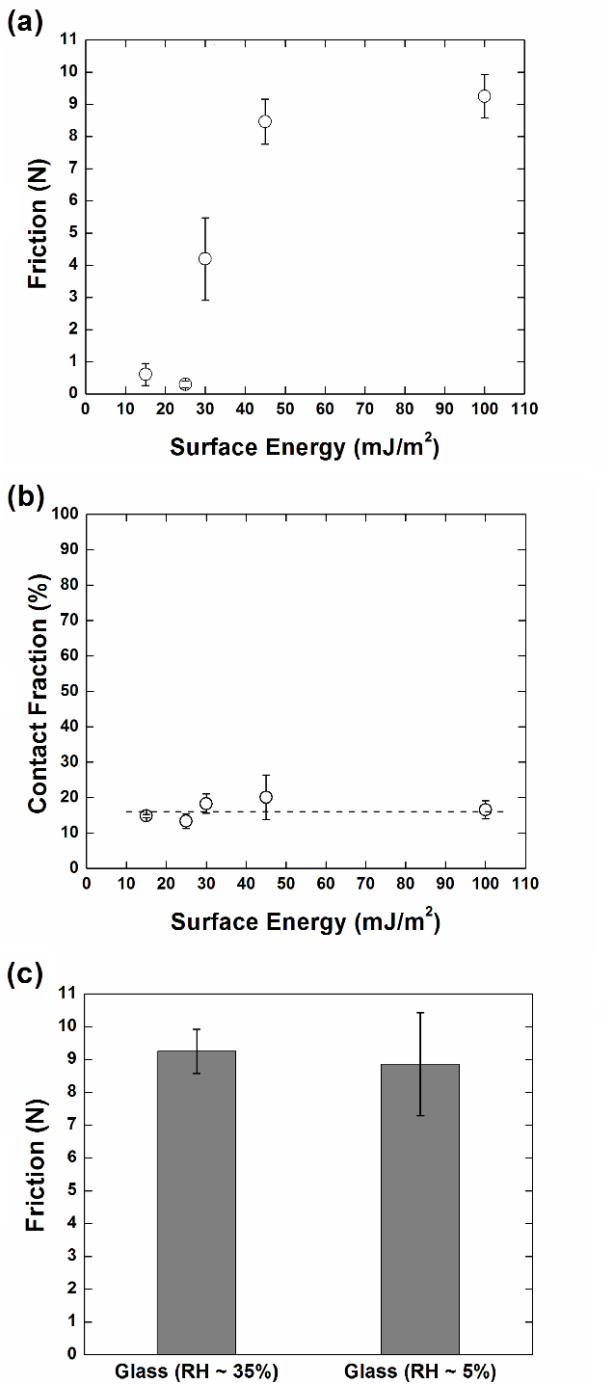

Figure 4.2: a) Macroscale friction of 1 × 1 cm^2 sample against substrates with various modified surfaces. b) The apparent sample contact area simultaneously observed for the same substrates. c) Friction of nanofiber array against hydrophilic glass substrate at two different humidities.

where τ is the shear strength coefficient, A_f the tip contact area, μ the Coulomb friction coefficient, and $F_{N,f}$ the normal load per fiber. With ~17% apparent contact and assuming all fibers within this area are in actual contact, the normal load per fiber is ~6 nN. Taking friction against glass as an example, a typical value of τ = 6 MPa for LDPE [86] and A_f = 0.023 μm^2 predicted from JKR contact mechanics [80] yields ~140 nN of contribution to friction from the first term. The value of μ = 0.3 for LDPE [86] gives rise to only a small value of ~2 nN for the second term.

With negligible contribution from the load-dependent friction, the counter-substrate surface energy can affect friction in two ways. At low normal loads, the JKR prediction of fiber tip contact area (Equation 3.4) reduces to:

$$A_f = \pi\left(\frac{9\pi(1-\nu^2)WR_t^{\ 2}}{2E}\right)^{2/3}, \tag{4.2}$$

where E (~200 MPa [83]) and ν (~0.4 [87]) are Young's modulus and the Poisson ratio of the LDPE fibers, W the work of adhesion between LDPE and the substrate, and R_t (~300 nm) the radius of curvature of the fiber tip. The work of adhesion can be approximated as $W = 2(\gamma_f\gamma_s)^{1/2}$, where γ_f (~35 mJ/m^2 [67]) and γ_s are the surface energies of the fiber and the substrate, respectively [65]. This indicates that the fiber tip contact area is proportional to $\gamma_s^{1/3}$.

The interfacial shear strength (τ) itself is also directly proportional to W as suggested by the Cobblestone model of interfacial friction [98], in the case of static friction. This results in roughly F_f α $\gamma_s^{5/6}$ overall dependence, predicting a nearly linear decrease in friction with decreasing substrate surface energy. This corresponds to 30 to 140 nN of friction per fiber over the surface energy values from 15 to 100 mJ/m^2. However, while this simplified analysis explains the decrease in friction due to the reduced adhesion between a single fiber and the substrate, it cannot fully account for the observed macroscale behavior, specifically the sudden drastic reduction in friction in a narrow range of surface energy. To give further insight as to why such a drop in performance is observed, the assumption that all fibers within the apparent contact area are in actual contact, should be revisited.

While all substrates showed similar fraction of bright region (~17%), the light intensity within the contacting region showed drastically different behavior during testing. As shear load was progressively added, substrates with low surface energies (e.g. DTS) showed only marginal increase in intensity, while those with high surface energies (e.g. AUTS) showed a significant increase. It is important to note that the contact fraction (~17 %) only represents the macroscale contact determined primarily by the non-planarity of the backing film. The higher light intensity, on the other hand, is attributed to increased degree of microscale contact (as more intimate LDPE/Glass interface is formed to redirect more incident light from the parallel direction along the interface to the normal direction observed by the camera), suggesting either more fibers coming into contact within the contact fraction, or conformational change of individual fibers from tip-contact to side-contact [74]. As mentioned, the fibers are not sufficiently long to make such a

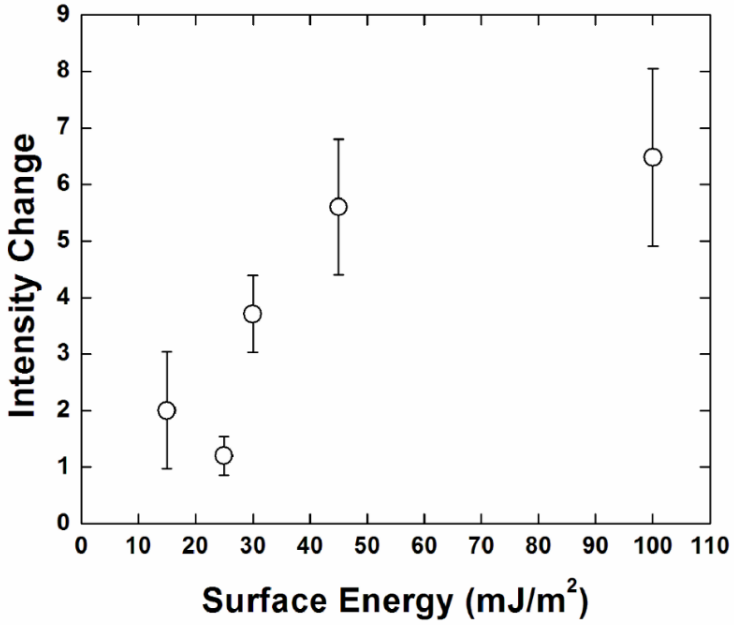

Figure 4.3: Increase in light intensity of contacting area observed during friction measurements. While samples against all substrates showed ~17% apparent contact area prior to sliding, only the ones exhibiting high friction showed a significant increase in intensity.

conformation change, so the increase in intensity is likely from increased number of fibers in contact, rather than transition from tip-contact to side-contact.

In order to correlate the number of fibers in contact with the intensity of images obtained from FTIR method, the images were first converted to 256 grayscale, then the difference in grayscale values between the contacting region and the background region was calculated (ImageJ, version 1.43u). This allows the quantification of the relative change in intensity, I, from the initial state (before any shear loading) to the final state (just prior to detachnment), defined by the ratio $I_{final}/I_{initial}$. The analysis has been performed for the samples corresponding to the data in 4.2a, and the result is summarized in Figure 4.3, which shows that there is a strong correlation between the light intensity of the contacting region and the friction of the nanofiber arrays. The sharp drop in friction against lower surface energy substrates, which could not be fully accounted by simply considering either the capillary effect or the adhesion energy based on the apparent contact area, is suggested to be from dramatically decreased number of fibers in actual contact.

As described in Section 3.7, the number of fibers in contact is directly affected by the ability for fibers to bend to overcome any fiber height variation from fabrication and/or the roughness in the substrate to induce neighboring fibers into additional contact. Equations 3.5 and 3.6 can again

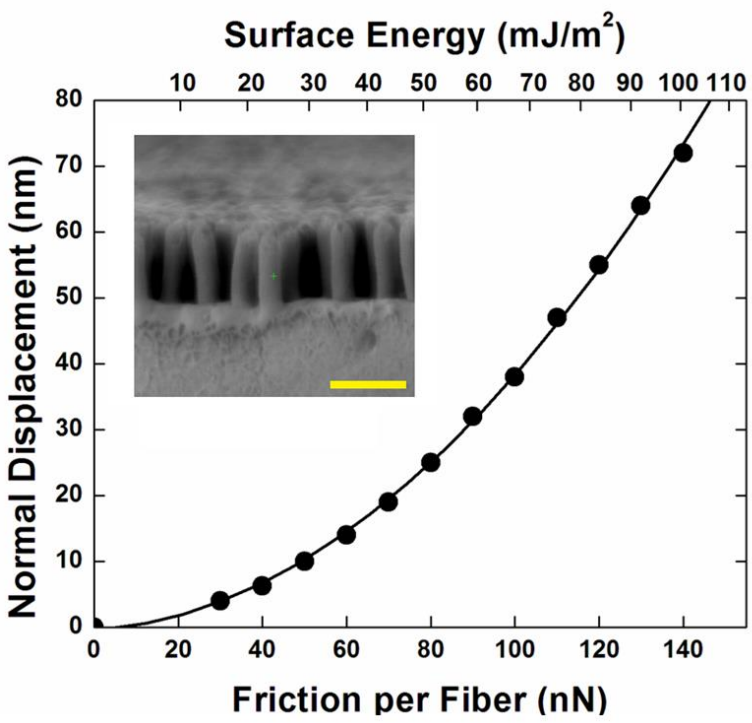

Figure 4.4: The vertical displacement, δ, of a fiber induced by a range of friction values, F_f. The corresponding surface energy of the substrates required for generating the friction is also shown, based on the approximated $\gamma^{5/6}$ dependence. The inset shows the cross-sectional image of the nanofiber array (scale bar = 2 μm).

be applied to calculate vertical displacement caused by the shear loading. The dependence on substrate surface energy is reflected in the term F_f, since the maximum loading allowed on each fiber is limited by the adhesion between the fiber tip and the substrate. As given earlier, the range for the counter-substrates tested here is 30 – 140 nN. Figure 4.4 shows the maximum displacement possible for an individual fiber (D = 600 nm, L = 2.5 μm) over various maximum theoretical friction forces determined by the surface energies. For lower values of surface energies, e.g., 15 - 25 mJ/m^2 corresponding to the substrates that showed very low friction (FDTS- and DTS-treated surfaces), the fibers are able to bend only several nanometers. With increasing adhesion between the substrate and the fibers, significantly more bending occurs, up to nearly 100 nm.

In the previous chapter, the idea that the fiber bending allows increasing number of fibers to come into contact has been used to explain why fiber length is a critical factor in macroscale performance of fibrillar adhesives, where the fibers must be flexible enough to overcome the variation in fiber height and/or any roughness of the substrate. This can be similarly applied to

Figure 4.5: Schematic illustration of the suggested microscale contact morphologies during the friction testing of nanofiber array against high- and low-surface energy substrates. Arrows indicate the direction of loading, where the sizes qualitatively show the relative magnitudes of the maximum load before sliding.

explain the critical role surface energy may play in attachment of fibrillar adhesives, where the adhesion between the fiber and surface must be sufficient to result in bending that can allow neighboring fibers to come into additional contact, as schematically depicted in Figure 4.5. For the LDPE nanofibers tested in this study, the critical point above which this can happen seems to lie between the surface energy range between ~20 - 40 mJ/m^2 as observed in Figure 4.2a. From Figure 4.4, this would imply that fibers have to overcome roughly 10 - 20 nm in either the roughness of the substrate or the height variation of the fibers. The counter-substrate topography was measured with AFM to be nearly smooth (RMS ~ 1 - 2 nm) as previously mentioned. From the SEM side view of the nanofiber array (Figure 4.4 - inset), the RMS variation in fiber height was estimated to be ~30 nm. Thus, it seems that for the LDPE nanofibers in this study, sufficient adhesion from high surface energy substrate was required to ensure the fibers bent enough to tolerate the variation in height and lead to the large observed macroscale friction values. Finally, as suggested by the elastic beam model used in the analysis, any change in parameters that decrease the rigidity of fiber (i.e., smaller diameter, larger length, and lower modulus) may moderate the sudden reduction in performance at lower surface energies.

4.4 Summary

In this chapter, we examined macroscale friction of nanofiber arrays against substrates of varying surface energy. While the arrays exhibited high friction on high surface energy substrates, they showed unexpectedly low performance against those with low surface energy. The drastic reduction could be explained neither in terms of capillary effect nor by only considering the reduced adhesion resulting from reduced surface energy. Simultaneous measurement of contact area by reflected white light showed that while the apparent contact area stayed similar between

all substrates, the intensity varied significantly, indicating that the number of fibers in actual contact was very sensitive to substrate surface energy. By relating the friction per fiber predicted from the JKR model to the vertical displacement of the fiber, it was suggested that the nanofibrillar array could overcome their inherent height distribution only when the substrates had sufficient surface energy to ensure effective engagement. This study shows that surface energy of countersurface is an important criterion in gauging the performance of gecko-inspired adhesives. Future design of versatile fibrillar adhesives should ensure attachment to substrates with widely varying surface energies, which are likely to be encountered in practical applications. For example, higher aspect ratio structures with hierarchy could cover a wider range of counter-substrate surface energy via easier fiber bending even under weak interfacial adhesion.

Chapter 5

Effect of counter-substrate roughness

5.1 Background

While many fibrillar adhesives perform well against smooth surfaces, their adhesion and friction are drastically reduced with the introduction of surface roughness [18, 29, 47, 50, 64]. Since most surfaces encountered in practical applications are rough at various length scales, understanding the interface between fibrillar and rough substrates is critical in rational design of fibrillar adhesives. Only a limited number of studies have experimentally probed the effect of roughness on fibrillar adhesion and friction. Studies of natural geckos show that the ability of the animal to cling to an angled or inverted surface can exhibit a minimum [42] or maximum [99], depending on whether the surface roughness scale allows for the penetration of nanoscale spatula or microscale seta structures. Synthetic gecko adhesives have shown similar behavior with a maximum pull-off strength [100] and friction force and normal adhesion after sliding [101], when the roughness was compatible in scale with the fibers. Other studies, however, have shown monotonic decrease in normal and shear adhesion with increasing roughness [18, 47, 64]. While these studies suggest interesting and complex relationships between roughness and adhesion/friction, the surfaces used had randomly rough features that are difficult to characterize and compare. Although this is true of surfaces in real use situations, simplified model substrates with defined patterns would aid in fundamental understanding of fibrillar contact against rough surfaces. To this end, some studies have used microfabricated gratings to test adhesion or friction on substrates with more well-defined features, where fibers are observed to deform to conform to the substrate during normal loading [20], and the friction has shown to decrease with increasing peak heights [29]. Incorporation of a structured backing more compatible with corrugation on the counter-substrate has also been demonstrated to improve shear adhesion [50].

Still, many factors that contribute to defining rough surfaces, e.g., spacing, height, and shape of asperities, have not been studied in detail and further elucidation would help in design of gecko-like adhesives that perform well on practical surfaces. In addition, most of the literature, in particular studies that focus on the roughness effect [100, 101], have used soft elastomers (such as PDMS with Young's modulus of a few MPa or lower). Such materials can have large bulk deformation to conform to surface features, which is not possible with harder polymers such as polyethylene (Young's modulus 100 MPa or higher). This chapter presents a systematic study of how macroscale friction of polyethylene nanofibrillar surfaces is affected by various geometrical factors of roughness, such as the height of the peaks, distance between the peaks, and the area available for contact. A simple method utilizing colloidal lithography and silica evaporation is used to fabricate rough substrates with independent control over those geometrical factors. This allows us to examine the factors that allow synthetic fibrillar adhesives to adhere successfully to some rough substrates and fail on others. Simple mechanical models are used to aid the understanding of the observed friction behaviors.

5.2 Counter-substrate preparation

As described in Section 2.2, colloidal lithography provides a simple way to pattern a large area with repeating patterns. This facilitates the preparation of a model rough substrate with well-defined asperities with control over the geometrical parameters such as height, width, and spacing. The overview of the procedure is shown in Figure 5.1. A base silica layer of 300 nm is first evaporated on a Si wafer, and then the substrate is diced into a size large enough for friction testing (larger than 1×1 cm^2). Microspheres of various diameters (0.5 – 8 μm) are deposited, and an additional layer of silica is evaporated. After the removal of spheres by sonication, the substrate is left with silica peaks where the interstices of the sphere array allowed the penetration of the additional evaporated layer.

As depicted in Figure 5.1 (bottom), the microsphere array would ideally be hexagonally close-packed, leaving triangular peaks around the area where the spheres were originally deposited. However, due to some unavoidable defects from monolayer assembly, some peaks merge and deviate from hexagonal arrangement. Therefore, we nominally take the size of the spheres to be the peak spacing. In this process, the diameter of the initially deposited spheres determines the resulting distance or the spacing between the peaks (S_P), and the duration of silica layer evaporation over the spheres can be varied to control the height of the peaks (H_P). As needed, the deposited spheres can be reduced in size by oxygen plasma prior to silica evaporation to increase the interstitial area between the spheres, which results in peaks with larger areas at the top. A representative 3-D AFM topography is shown in Figure 5.2a, along with a line profile (Figure 5.2b). Figure 5.2c is a representative AFM image of the evaporated silica layer, revealing nanoscale surface texture.

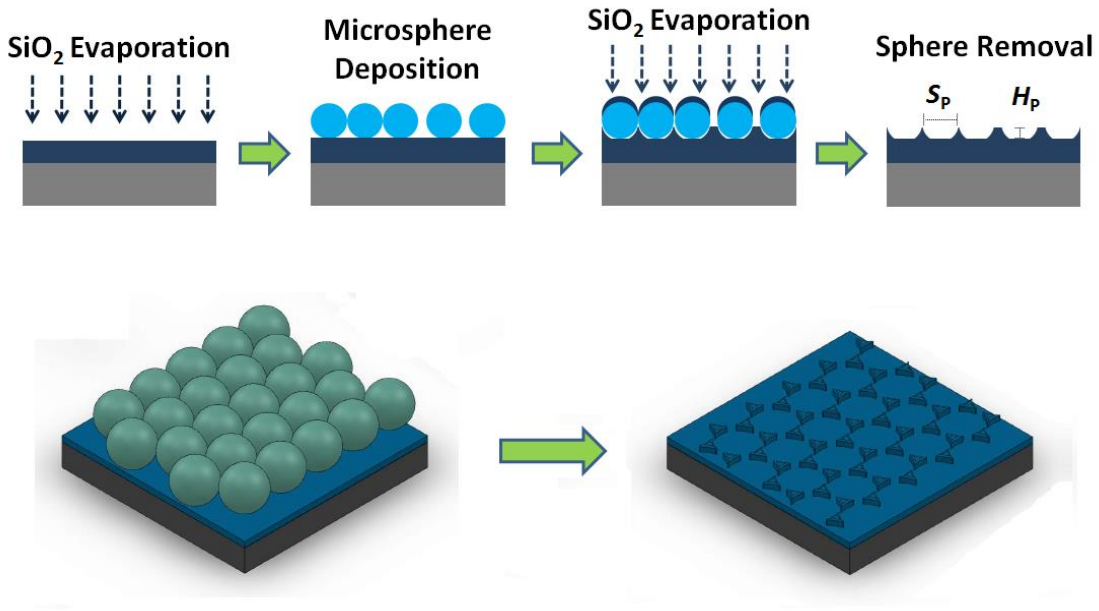

Figure 5.1: Colloidal lithography to produce patterned rough counter-surface. A base silica layer is first evaporated, then the second silica layer is deposited over the sphere array. The spheres are removed by sonication. 3D views of steps (ii) and (iv) are shown below.

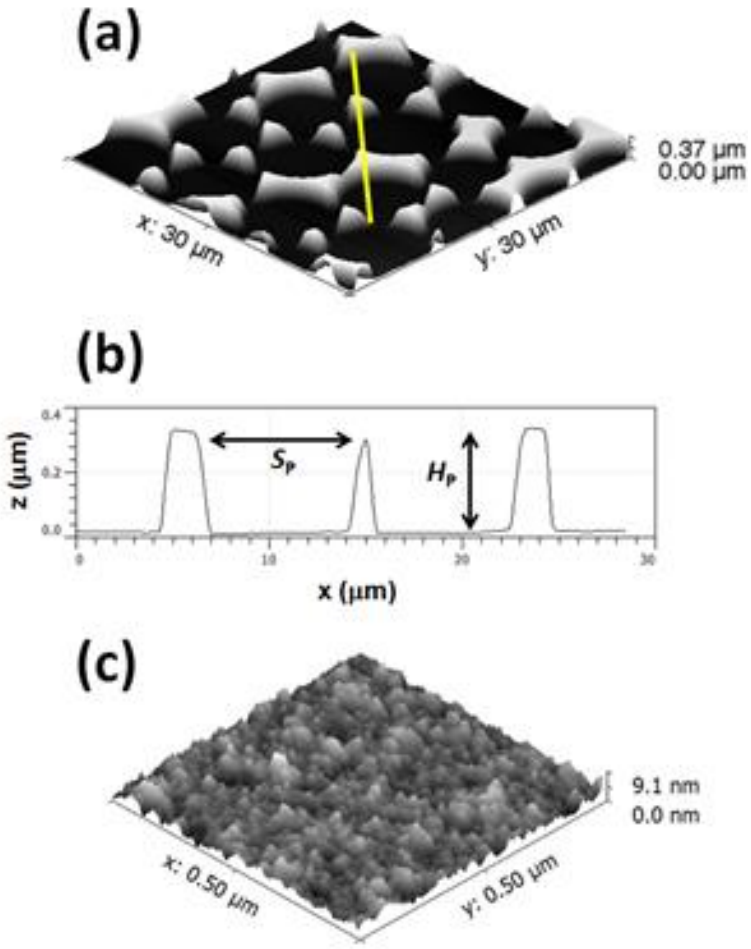

Figure 5.2: (a) A representative 3-D AFM topography of a patterned surface (S_P = 8 µm is the initial size of the sphere, H_P = 300 nm is the height of the evaporated silica). (b) A line profile across the surface corresponding to the line drawn in (a). (c) AFM topography of the evaporated silica layer with nanoscale roughness (RMS = 1.1 nm).

5.3 Friction and roughness of counter-substrate – effect of peak spacing and height

For the roughness study, fiber diameter (D) is fixed at 510 nm, and fibrillar arrays with two different fiber lengths (L) are fabricated (1 µm and 2 µm). In Figure 5.3a, the macroscale friction of a 1 × 1 cm^2 LDPE fibrillar array patch (L = 2 µm) is plotted against the counter-surface peak height, H_P, for three peak spacings, S_P = 0.5, 1, and 8 µm. The friction against the control flat substrate is ~5 N, and is generally adversely affected with the introduction of roughness. However, the decrease is more drastic when the peak spacing approaches the fiber diameter (0.51 µm), e.g., high friction (4 - 5 N) is maintained for H_P = 30 nm for S_P = 8 µm, but the same height of roughness for S_P = 0.5 µm reduces friction by a factor of roughly 10. This could indicate that as peaks on the counter-surface are placed closer together, individual fibers have more difficulty penetrating to contact the valleys, and the overall number of contacting fibers is reduced (since the area of the peaks accounts for only about 15% of the projected area, a significant number of fibers must reach down to valleys in order to ensure high macroscale friction). Studies on randomly rough surfaces for natural gecko and synthetic fibers have observed a drop in adhesion or friction as the average size of the counter-substrate features becomes smaller than the fiber diameter [99-101]. While we also observe reduction of friction at small asperity spacing, the reduction is evident even for peak spacing higher than the fiber diameter. It seems that as the number density of the peaks increases with decreased spacing, the fibers are more likely to be obstructed from making proper contacts with the valleys. We also do not observe increase in friction as the asperity spacing and the lateral dimension of the fibers become similar. The studies using polydimethylsiloxane (PDMS) synthetic fibers [100, 101] suggest an interlocking mechanism of fibers and asperities to explain the high friction, and it is indicated that the low modulus of PDMS (~0.75 MPa) facilitates the penetration and interlocking [101]. LDPE is typically over two orders of magnitude stiffer (~200 MPa) which would make the interlocking mechanism more difficult.

It is interesting to note that the evaporated silica control sample has roughness on the length scale of a few nanometers (Figure 4c, RMS = 1.1 nm, with average peak-to-valley height of 3 nm), two orders of magnitude smaller than the smallest dimension of the fibers. While fiber penetration into such small features would be impossible, high friction values obtained on these control samples (which only have the inherent roughness from the evaporated silica) indicate that the LDPE fiber tip can sufficiently deform when features become small enough. Similarly, the adhesion behavior reported on natural gecko spatula indicated that the spatula structure can adapt well to surfaces with low roughness [42].

The friction behavior on substrates with 8 µm-separated features also suggests there is a critical peak height at which the friction rapidly drops, i.e., while high friction is maintained up to 75 nm of feature height, a drastic decline is observed for the feature height of 150 nm and above. The dotted line in Figure 5a indicates the approximate peak height (for 8 µm peak spacing) below which the samples exhibit high friction.

In order for a sufficient number of fibers to contact the valleys in shear loading, it is plausible that the fibers that first contact the top of the peaks have to bend to allow neighboring fibers to

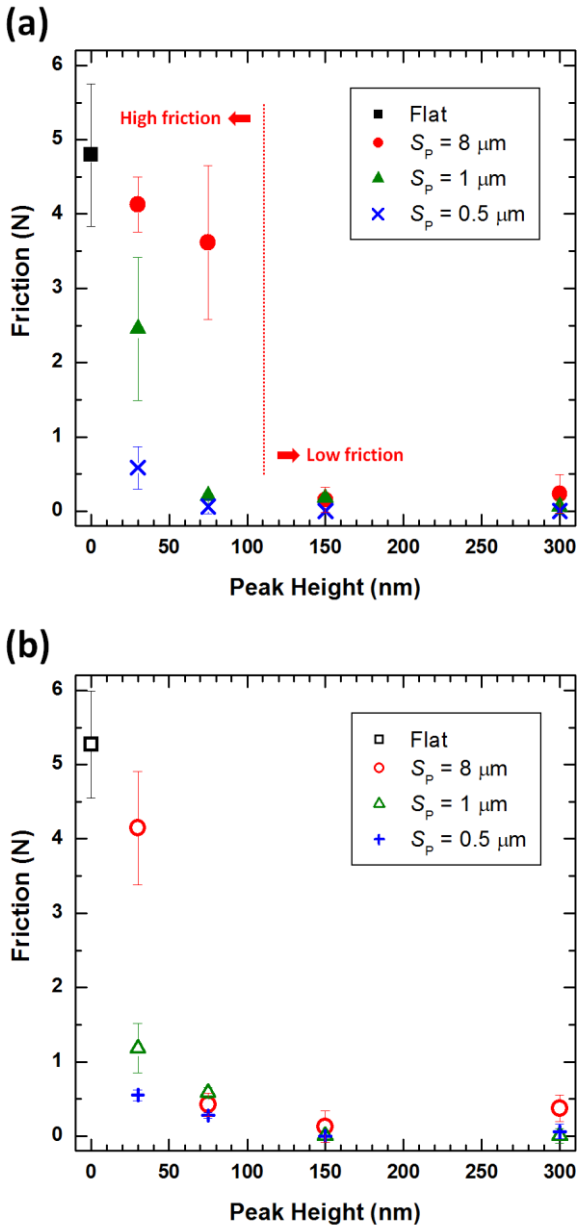

Figure 5.3: (a) Macroscale friction of 1 × 1 cm^2 array of 2 μm fibers on patterned surfaces with varying peak heights, H_P, and spacing, S_P, as well as a control flat surface. For S_P = 8 μm, high friction is maintained up to H_P = 75 nm but sharply drops afterwards, and the approximate boundary is indicated by the dotted line. This drop is observed at lower peak heights as S_P approaches the fiber diameter. (b) Friction tests against the same surfaces using 1 μm fiber array. Similar performance is observed on a flat surface, and decreasing S_P again adversely affects friction. In comparison to 2 μm fibers, drop in friction occurs at lower H_P.

contact the valley. Above a certain peak height, however, fibers may not have enough bending compliance to accommodate the height difference. To test the suggested mechanism, fibers that are roughly half as long (1 µm) are tested, with all other geometric parameters held constant. Friction tests against the same set of patterned surfaces were done with the result plotted on Figure 5.3b. On the flat surface, the fibers of two lengths perform similarly, and the friction of shorter fibers are also adversely affected as the peak spacing gets smaller. With respect to peak height, however, it is evident that the shorter fibers begin to exhibit low friction at a lower height, consistent with the mechanism above. Long fibers significantly outperform shorter ones at H_P = 75 nm for S_P = 8 µm, as well as at H_P = 30 nm for S_P = 1 µm. While there may be some convolution of effects from reduced peak spacing for S_P = 1 µm as explained above, the tests on S_P = 8 µm should only highlight the relationship between the fiber length and peak height (since S_P is much larger than fiber diameter D), and the results have been replotted in Figure 5.4 for more detailed analysis.

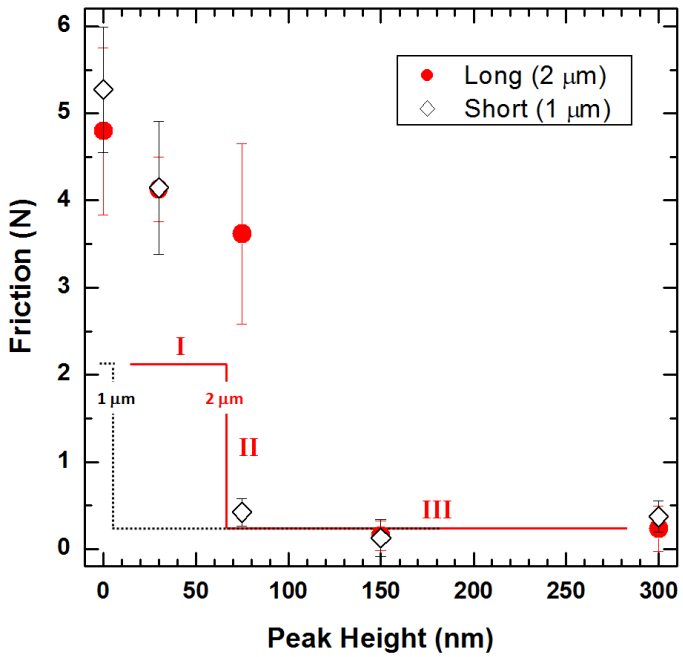

Figure 5.4: Friction comparison of 1 µm (short) and 2 µm (long) fibers on rough surfaces with varying peak height H_P with peak separation S_P fixed at 8 µm (1 × 1 cm^2 samples). Performance of shorter fibers is more adversely affected by roughness than that of longer fibers. The solid (red) and dotted (black) lines are piecewise predictions of friction behavior based on the JKR model (I), bending limitations from an elastic bending model (II), and calculated reduction in the number of fibers in contact (III).

As indicated in Figure 5.4, the data can be categorized into 3 regimes: high friction region where a high number of fibers are in contact (I), a transition point at which the peak height becomes larger than the adaptability limit of the fibers (II), and the low friction region where only a small fraction of fibers are in contact, due to their inability to contact the valleys (III).

The calculated friction per fiber can subsequently be related to the vertical displacement of the fiber by an elastica model for beam bending as a first-order approximation (Equation 3.5 and 3.6), in the similar manner as before. For fibers 1 μm and 2 μm in length, the corresponding δ values are calculated to be 2 and 60 nm, respectively, which serve as rough estimations for the deflection limit of fibers based on the bending flexibility (vertical lines in Figure 5.4). For 2 μm fibers, the simple model seems to be consistent with the experimentally observed drop in friction, although somewhat underestimating where the drop occurs. The critical peak height is significantly underestimated for the shorter fibers, probably due to the limitations of the simple model. Plastic deformation may also provide additional vertical displacement, which would be more significant for short fibers relative to their elastic bending. For a practical consideration, it is noted that while increasing fiber length further would provide more bending compliance, it is limited by lateral fiber clumping, at which point the clumped group loses much of its ability to adapt to surface roughness.

Finally, the low friction behavior can be approximated by considering the reduced number of fibers in contact as fibers are no longer able to contact the valleys. The peak areas account for only about 15% of the total area, and thus, most of individual contact points are lost due to fibers' bending limitations at the microscale. Another, less significant loss occurs at the macroscale, where the contact reduction of patch from 20% to 15% is observed for low friction samples. With these two factors, the macroscale friction is predicted to be reduced to 2.1 N × 0.15 × (0.15/0.2) = 0.24 N, shown as line III in Figure 5.4.

Despite the simplicity and limitations, this analysis predicts similar trends to the experimental behavior and the analysis offers an explanation on how fibrillar arrays of varying fiber lengths can perform similarly on a flat substrate, yet drastically different on a substrate with a certain peak height (75 nm in our case).

5.4 Effect of peak area fraction

So far, the proposed explanations of observed friction behavior rely on the assumption that the number of fibers in actual contact is the dominant factor in determining the macroscale friction. To support this, counter-substrates were prepared with varied area fractions occupied by the peaks of the features. This is achieved by plasma etching the spheres prior to silica evaporation of the features, which increases the interstitial area between the spheres. The height of the peak is chosen at 300 nm so that the fiber contact with the valley is unlikely, and therefore the peak area directly corresponds to the local area available for intimate contact. The friction behavior is shown in Figure 5.5 for 1 and 2 μm fibers against substrates with varying peak areas while maintaining the spacing and height constant at 8 μm and 300 nm, respectively. The macroscale friction correlates

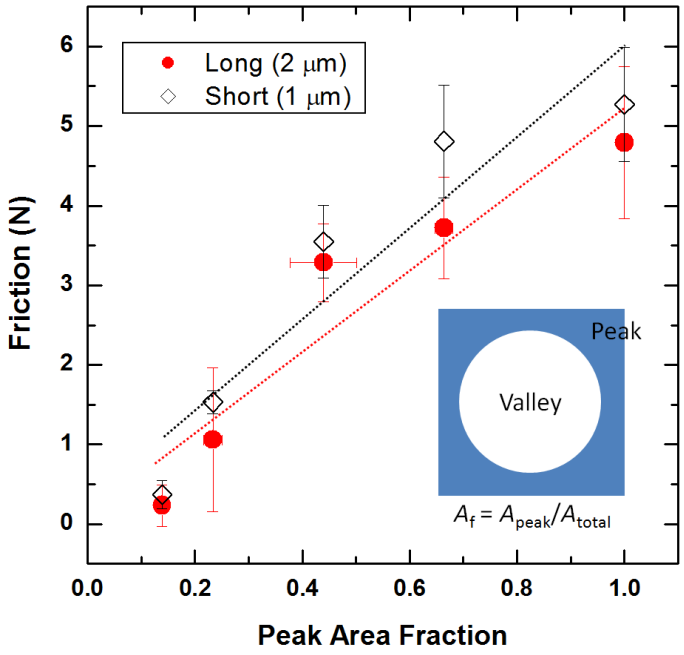

Figure 5.5: Macroscale friction of nanofibrillar array against rough surfaces having different peak area fraction for two fiber lengths, 1 and 2 μm. Increase in peak area available for fiber contact increases macroscale friction for both cases. The dotted lines are linear fits to respective data.

reasonably well with the peak area fraction for both lengths, supporting that the ability of the 1×1 cm^2 sample to adhere to the counter-surface is predominantly driven by the local area available for fibers to contact. As the peak height is too large to adapt for fibers of either lengths, no apparent advantage of long fibers is shown on these substrates.

5.5 Criteria for high friction performance on rough surface

Based on the friction tests of LDPE fibrillated surfaces against patterned counter-surfaces with varying asperity peak spacing, height, and area, the macroscale friction behavior on rough surfaces can be summarized with simple criteria with respect to those geometric parameters. On a nominally flat substrate, most of the fibers can come into contact, and the nanoscale roughness can be overcome by tip deformation (Figure 5.6-i). With introduction of surface roughness, fibrillar arrays can maintain high macroscale friction (ii) until the roughness peak height reaches beyond the bending compliance of the fibers, at which point friction drastically drops (iii). This effect is more

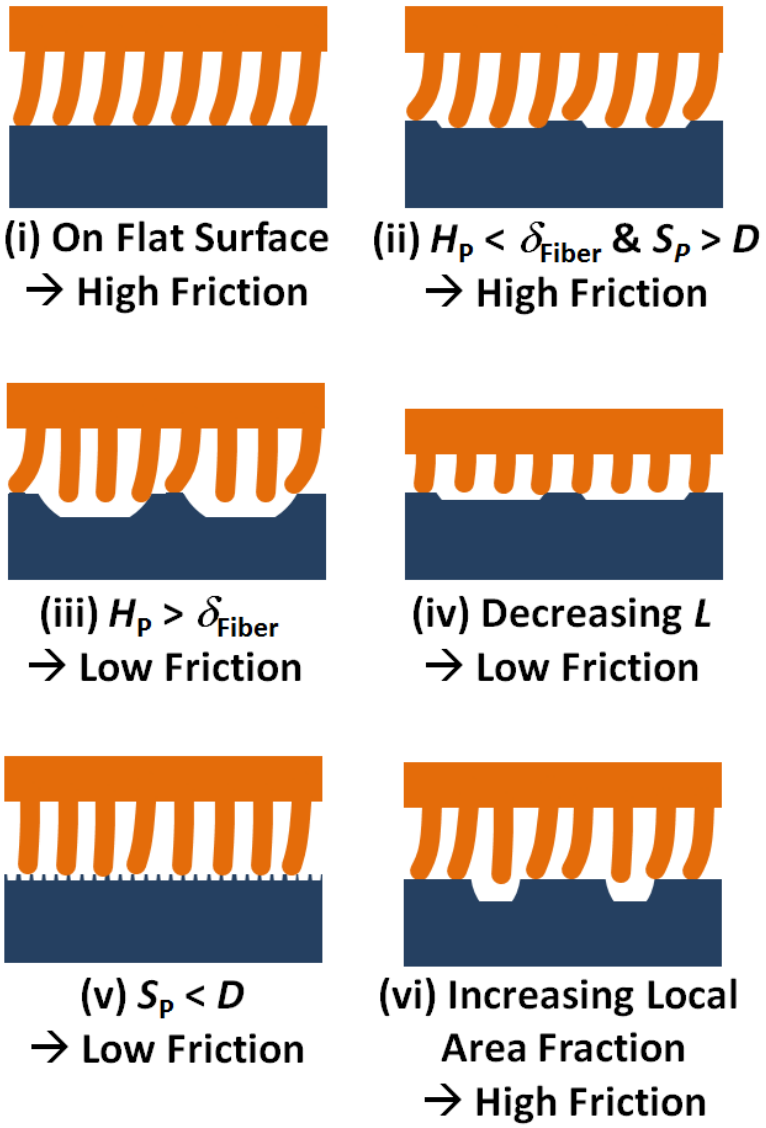

Figure 5.6: Summary of observed behavior in fibrillar friction against patterned rough surfaces. High friction is observed for nominally flat surface (i), when peak is sufficiently shallow and spaced (ii), and with large peak area available for contact (vi). Increasing peak height (iii), shortening fiber length (iv), and closing the gaps (v) lead to low friction.

severe for shorter fibers due to higher stiffness (iv). Regardless of the peak height, poor friction performance is observed as the distance between the peaks becomes smaller than the fiber diameter and prevents penetration of fibers (v). Finally, it is confirmed that the local contact area predominantly determines the macroscale friction behavior, as macroscale friction correlated well with the peak area available for fiber contact (vi).

5.6 Summary

This chapter probed the friction behavior between fibrillar arrays and rough surfaces by independently controlling several parameters important in characterizing a rough surface. While it was evident that the real area in contact with the fibers determined the macroscale friction, high friction was ensured on only the surface whose roughness features had lower height difference than the vertical displacement allowed for individual fibers and had sufficient gap to allow penetration of the fibers. Simple models pertaining to adhesion and bending mechanics of fibers could be used to explain some of the observed behaviors. In spite of the 2 orders of magnitude greater modulus of LDPE compared to PDMS used in previous roughness studies [100, 101], some similarities can be seen in that friction performance can suffer from having surface roughness that prevents proper fiber contact. However, due to using more regularly defined surfaces, we observe a very distinct drop of an order of magnitude in friction that can be specifically attributed to various dimensions of the asperity, as well as that of the fibers.

While the presented method provided a way to fabricate and characterize patterned rough surfaces for testing gecko-like adhesive, real surfaces present more challenges as the asperities are randomly distributed and often are hierarchical. Designing an adhesive surface as versatile as the natural gecko pad would require incorporation of complex hierarchical fibers that would adapt to a wide range of asperity sizes, density, and shapes. This study provides some insights on what the important parameters are in designing such an adhesive, and may provide a useful guidance especially in cases where the application is targeted towards a specific surface and the roughness compatibility between the adhesive and the target surface is critical.

Chapter 6

Fabrication of complex fiber designs

So far, we have examined various aspects of fibrillar friction using well-defined, vertically-oriented cylindrical pillars. While the simple fiber geometry allows for application of simple modelling and provides insights into fundamental aspects of GSA performance, its limitation was clear in their failure to adhere strongly to rough or low-energy surfaces. This motivates more complex fiber designs, some of which were covered in the introduction as part of the literature survey. This chapter presents some alternative methods for fabrication of complex high-aspect-ratio structures. Sections 6.1 and 6.2 are dedicated to controlling the morphology of SiNW etched by metal-assisted chemical etching. Significance of further examining the etching condition and the resulting structure is two-fold: 1) it leads to better control over the template geometry for subsequent molding into GSA, and 2) SiNW have attracted great interest due to their novel physical and chemical properties and potential applications in nanoelectronics [102, 103], optoelectronics [104], thermoelectronics [105], sensing [106], and renewable energy devices [107]. Section 6.1 focuses on the ratio of HF/H_2O_2 concentrations which affects the porosity, tapering, and clumping of the SiNWs, as well as effects of introducing small amount of electrolyte to the solution. Section 6.2 presents a method to induce unidirectional tilting and curving of SiNW by means of adding organic solvents to the etching bath.

Later sections provide new fabrication schemes for complex fiber designs. Hierarchical structures are fabricated by a few different methods that place nanofibers on top of micro-sized base pillars. Composite fibers are fabricated, where two different materials are used for the fiber and the backing film. Finally, a method to precisely tune the tapering angle of micropillar is presented. While most of these fabrication methods do not employ metal-assisted chemical etching, they utilize other silicon etching and soft lithography techniques, and the methods may aid in the future fabrication of even more complex fiber designs.

6.1 Controlling porosity, clumping, and tapering of SiNWs formed by metal-assisted chemical etching

This section contains material from the following publication with permission from the contributing authors: D. H. Lee, Y. Kim, G. S. Doerk, I. Laboriante, R. Maboudian. Strategies for controlling Si nanowire formation during Au-assisted electroless etching. *J. Mater. Chem.* **2011**, *21*, 10359-10363. <http:/dx.doi.org/10.1039/C1JM11164G>. Reproduced by permission of The Royal Society of Chemistry (RSC).

As briefly overviewed in Chapter 2, SiNWs are formed by chemically etching silicon covered by gold mesh film with regularly patterned holes. In this section we aim to examine several factors that control the resulting morphology of SiNW, in particular with respect to the porosity, clumping and tapering of the SiNWs. The substrate preparation method is similar to that described in 2.1 - 2.3, and for simplicity the nanowire diameter and spacing are fixed at 400 nm and 1 μm, while the length is varied by the duration of etching. We first explore the effect of HF/H_2O_2 ratio on the SiNW morphology as the etching progresses. The clumping and porosification phenomena are explained in terms of hole diffusion mechanism. A novel method to regulate these phenomena by introducing electrolyte to the solution is presented.

6.1.1 Effect of HF/H_2O_2 ratio

Figures 6.1 and 6.2 show the structural changes in SiNWs with respect to the HF/H_2O_2 ratio during the Au-assisted electroless etching. The ratio of etching constituents are noted by the volume of $HF/H_2O_2/H_2O$. For example, 1.8/0.2/8.0 denotes an etching condition in which 1.8 mL of HF, 0.2 mL H_2O_2, and 8.0 mL of deionized water are added for the total of approximately 10 mL of solution for a 1 × 1 cm^2 chip. At high HF/H_2O_2 ratio (Figure 6.1), SiNWs are etched vertically, increasing in length as etching progresses. With lowering ratio, slightly tapered SiNWs are tip-clumped with large bending in Figures 6.1b and c, and even SiNWs with low aspect ratios are bent and collapsed toward the bottom gold surface with more tapering (Figure 6.2). Based on the observed dependence of the NW morphologies on the relative ratio of HF and H_2O_2, the results in Figures 1 and 2 are categorized into three different etching regimes – regime I for vertical (Figure 1a), regime II for hooked (Figure 1b, c), and regime III for ground collapsed (Figure 2) shapes, as summarized in Table 1.

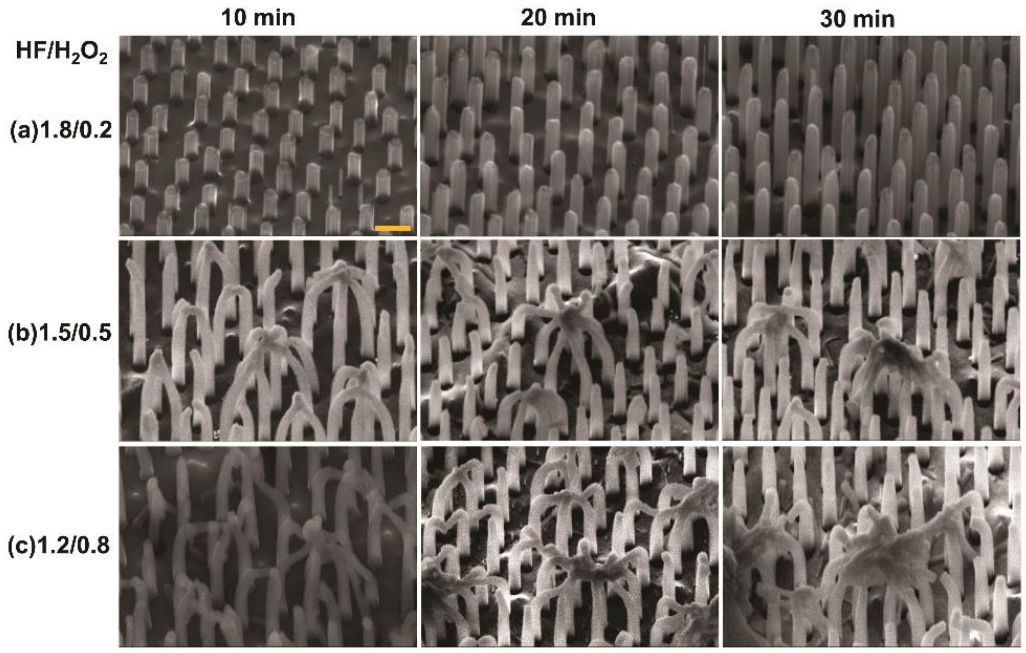

Figure 6.1: Temporal evolution of SiNWs during electroless etching of Si(100) for different HF/H_2O_2 ratios. $HF/H_2O_2/H_2O$ = (a) 1.8/0.2/8.0, (b) 1.5/0.5/8.0, and (c) 1.2/0.8/8.0. Each column indicates the etching time – 10, 20, 30 min. While SiNWs grow vertically for low H_2O_2 concentration (Fig. 1a – regime I), tip-clumped shape with large bending (hooked) SiNWs are observed for higher H_2O_2 concentration (Figs. 1 b, c - regime II). 45° tilt view, scale bar = 1 μm.

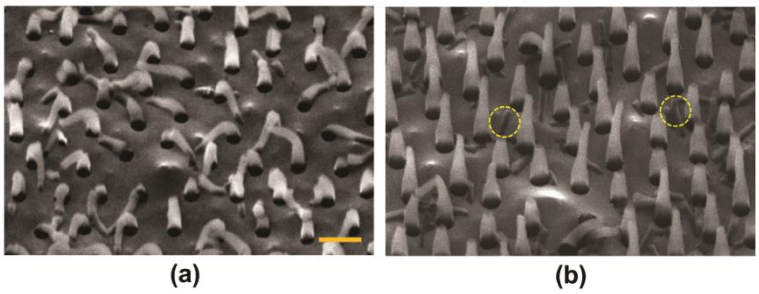

Figure 6.2: SEM images of SiNWs with further increasing H_2O_2 concentration ($HF/H_2O_2/H_2O$ = 0.9/1.1/8.0, etching time = (a) 5, (b) 10 min). Short, highly tapered SiNWs are observed to collapse toward the bottom surface (ground collapse, regime III). Broken fibers are observed as indicated by yellow dot circle (etching time = 10 min). The etched surface becomes unstable and inhomogeneous with significant film dewetting after 20 min. 45° tilt view, scale bar = 1 μm.

Table 6.1: Compositions of etching solutions used in this study with volume in mL and molar concentration in mol/L with a total volume of 10 mL for each 1 × 1 cm^2 chip.

Regime	Volume (molar conc.)		Morphology
	HF	H_2O_2	
I	1.8 (5.0)	0.2 (0.2)	vertical
II	1.5 (4.1)	0.5 (0.6)	hooked
	1.2 (3.3)	0.8 (0.9)	
III	0.9 (2.5)	1.1 (1.2)	ground-collapsed

6.1.2 Nano-porosity in SiNWs

As seen in Figs. 6.1 and 6.2, SiNWs in regimes II and III exhibit a large bending (approaching a 90° angle at the bending point) that is far outside the bounds of the linear elastic regime as shown elsewhere for SiNW bending under mechanical load [108, 109]. If the strain due to bending is expressed as r/R_c, with R_c being the bending radius, the estimated strain value (> 10%) is much larger than the maximum fracture strain of SiNWs (~1 – 2%) [108].

A recent paper has reported the increased porosity of SiNWs with large bending produced by metal-assisted electroless etching [110]. The high surface area and low density of nanoporous Si make it prone to faster ambient and wet chemical oxidation than single Si crystals, and hence susceptible to subsequent HF attack. To examine the porosity in the hooked SiNWs presented here, these samples are immersed in HF solution after wet oxidation in aqua regia solution as shown in Figure 6.3. Freshly etched SiNWs are predominantly unoxidized silicon, based on two facts: (1) The surfaces of the freshly prepared SiNW arrays are hydrophobic (water contact angles on the SiNW array surfaces are often larger than 140° depending on the aspect ratio of the SiNWs) and (2) negligible changes are observed for hooked SiNWs when immersed in HF solution right after electroless etching (Figure 6.3b). However, sharp nano-cone structures are generated when the hooked SiNWs are exposed to the highly oxidizing conditions of aqua regia treatment, followed by HF treatment (Figure 6.3c). This indicates that hooked SiNWs possess a large degree of porosity between the tip-end and bending point.

6.1.3 Visualization of hole diffusion effects

As shown in Figure 6.1b, c and Figure 6.2, hooked and ground-collapsed SiNWs have tapered shapes. A tapered shape with a decreasing diameter toward the tip is rationalized in terms of increased side-wall etching with higher H_2O_2 concentration. Sidewall etching and formation of tapered shapes in silicon nano- or micro-holes [111, 112] and SiNWs [113, 114] have been reported

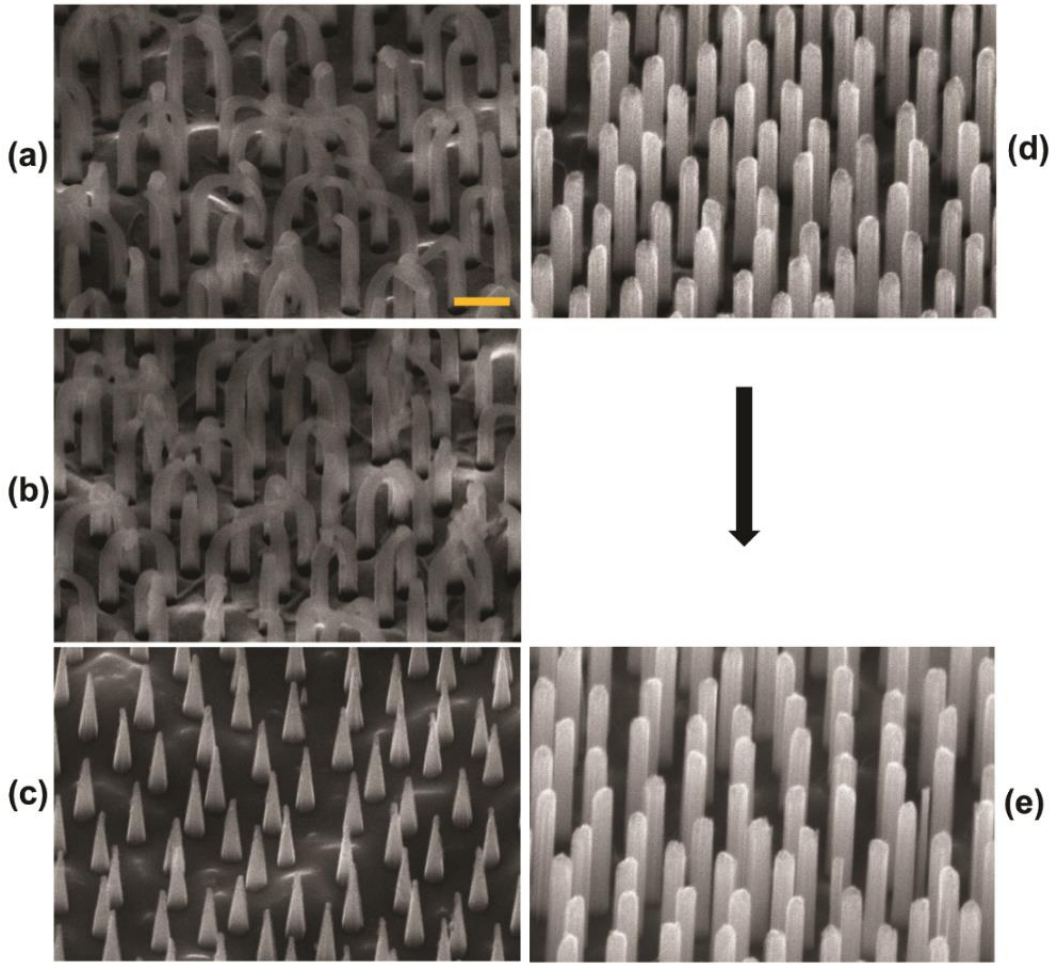

Figure 6.3: SEM images of SiNWs immersed in HF solution (30 min) after wet oxidation in aqua-regia solution (15 min) (45° tilt view, scale bar = 1 μm). Initial structures right after electroless etching are shown in (a) and (d) for hooked (preparation condition in Fig. 6.1b) and vertical (preparation condition in Fig. 6.1a), respectively. This oxidation/etching procedure caused removal of clumped SiNWs from the bent part to tip-end resulting in the formation of Si nanocones (c), while little change is observed for vertical SiNWs (e). For comparison, clumped SiNWs immersed in HF solution without wet oxidation right after electroless etching process show negligible change in SiNW structure (b). This result strongly suggests that hooked SiNWs have a nanoporous structure distributed between the bent part and the tip-end.

previously, and explained by considering either partial dissolution of the metal [112-115] or enhanced hole diffusion toward sidewall [111, 112] (injected by H_2O_2, reaction 2.1 and 2.2) away from the narrow interfacial region in contact with the metal. Partial dissolution of Au seems less probable in this study due to its relatively high redox potential as discussed in a previous report, [112] and thus the tapered shape of SiNWs observed here is attributed mainly to the enhanced hole diffusion toward the sidewall of SiNWs under high H_2O_2 concentration. It has been reported that oxidative dissolution of Si in HF solution is accompanied by the formation of a nanoporous Si structure, which is enhanced when more holes are injected into Si [110-112, 116-121]. This would consequently lead to the tapering of SiNWs after etching and dissolution of nano-porous region [111, 112, 122, 123].

For low H_2O_2 concentration, most of injected holes are consumed by Si dissolution at Au/Si interface, giving rise to the vertical shape (regime I). Increasing H_2O_2, that is, increasing the hole injection, can induce deviated diffusion of unconsumed holes at Au/Si interface toward the sidewall, which results in the tapered shape by significant etching of porous sidewall (regime II). Further increasing H_2O_2 concentration causes more significant development of porous sidewall relative to vertical etching, which gives shorter SiNWs with more tapering. This eventually becomes ground-collapsed (regime III). Details on how the porous NWs is bent are still unknown and remain an open question.

To further highlight the effect of hole diffusion towards the sidewalls, we explored ways to visualize it by changing the etching regime in a serial fashion during the synthesis process. A simple strategy is designed as follows: (i) preparation of vertical SiNWs from regime I, and (ii) exposure to electroless etching in regime III where significant tapering is typically observed. If isotropic etching or Au dissolution is dominant, a similar structure (vertical shape) with a smaller diameter should be observed (case A in Figure 6.4a). On the other hand, if sidewall etching due to lateral hole diffusion is dominant over isotropic etching in regime III, neck formation around a height corresponding approximately to the hole diffusion length scale should be observed (case B in Figure 6.4a). This idea was tested using larger diameter (~600 nm) SiNWs (Figure 6.4b) to magnify the effect. As shown in Figure 6.4c, baseball bat-shaped SiNWs are generated with a significant amount of neck formation. This strongly highlights the role of hole diffusion for solutions with high H_2O_2 concentrations during the electroless etching process, and shows that it is concentrated at the Au/Si interface with a limited diffusion length scale. A more realistic situation would be the case where the hole diffusion toward sidewall is dominant with some contribution from isotropic etching. Beyond the fundamental importance in gaining a more complete understanding of the metal-assisted electroless etching process for Si nanostructure formation, the practical implication of this experiment is that various Si nano-architectures may be fabricated with a proper understanding of the etching mechanism.

6.1.4 Regulating etching rate and clumping by electrolytes

As previously discussed, Au is more electronegative than Si, so the silicon beneath Au becomes more positively charged during the etching process. It may be expected that catalytic effect of Au

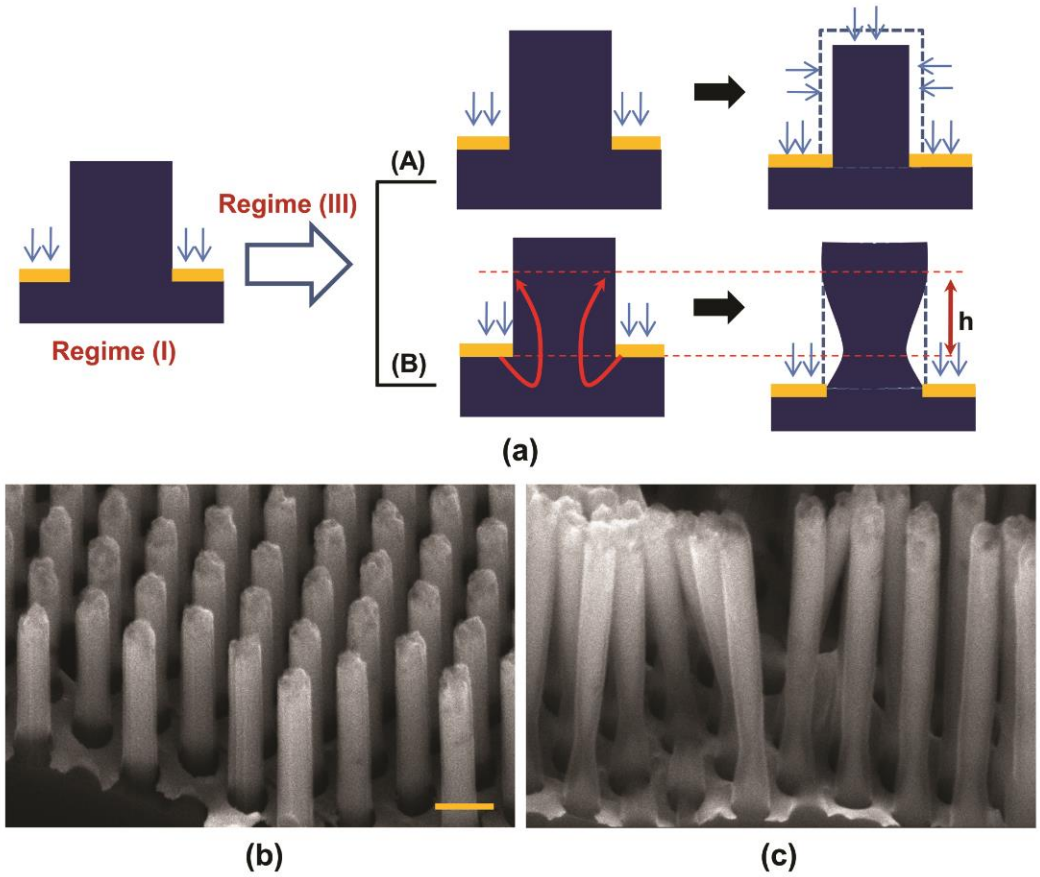

Figure 6.4: (a) Schematic illustration of the effect of transitioning from regime (I) to (III) during etching. As illustrated, if isotropic etching is dominant, neck formation would not be observed (A). If significant sidewall hole diffusion occurs with a length scale of ~*h*, NWs with neck formation would be observed as in (B). The results are shown in the SEM images – (b) vertical SiNWs (~600 nm diameter, grown in regime I ($HF/H_2O_2/H_2O$ (time) = 1.8/0.2/8.0 (20 min)), and (c) SiNWs with neck formation prepared by immersing (b) into etching solution with high H_2O_2 concentration (regime III, $HF/H_2O_2/H_2O$ (time) = 0.9/1.1/8.0 (5 min)), which highlights the role of hole diffusion near the Si/Au interface.

would be significantly altered with the addition of electrolytes due to screening by counterions. To test this idea, a small amount of common electrolytes was added to the etching solution (regime I). As shown in Figure 6.5a and b, a substantial decrease in the etch rate was observed – e.g., from ~10 μm/hr (without an electrolyte) to ~2 μm/hr by adding 10 mM of NaCl. As shown in Fig. 6.5c and d, the etch rate further decreases with higher NaCl concentration, and other electrolytes such as KCl and $CaCl_2$ have a similar effect on the etch rate depending the total ion concentration. These findings strongly support the above hypothesis that the Au surface is effectively screened by counterions from excess electrolyte, which then leads to diminished hole current density at the Au/Si interface. This result is an important finding that common electrolytes can be used as a retardant for metal-assisted electroless etching.

To further study the effect of added electrolyte on SiNWs morphologies, a small amount of NaCl was added to the etching solutions which correspond to bent and clumped shape. Figures 6.6a and b show SiNWs structures obtained by adding 10 mM NaCl into the etching solution used in Figure 6.1b and c, i.e., $HF/H_2O_2/H_2O$ = 1.5/0.5/8.0 and 1.2/0.8/8.0, respectively. Striking morphological difference is observed: vertical NWs with more tapered shape are formed instead of the hooked shape previously observed in the absence of NaCl. Note that the SiNWs in Fig. 6.6 are shorter than those in Fig. 1 under the same etch time, indicating that the etching rate decreases in NaCl-containing solution. As discussed earlier, under the etching solution of regime II and III, the porous regions generated by hole diffusion is formed, giving rise to a tapered shape after sidewall etching. Thus, more tapered shape with shorter length in Fig. 6 can be understood by greater contribution from porous sidewall etching when the reaction time is extended at a slower rate in the presence of electrolyte ions in solution. Under these conditions, SiNWs tend to be less porous and would not be subjected to clumping, and in extreme cases, long, spear-like structure are produced as shown in Fig. 6.6c.

6.1.5 Summary

Dramatic changes in SiNW morphology was demonstrated depending on the HF/H_2O_2 ratio. The hooked SiNWs with large bending beyond linear elastic deformation possessed a nano-porous structure distributed from the bending region to the tip-end during the etching process. This phenomenon was dominated by the relative amount of H_2O_2 to HF, so that increasing H_2O_2 was accompanied with more bending and tapering, eventually leading to the ground collapse of short, highly tapered SiNWs. These structural transformations were attributed to the enhanced hole diffusion towards SiNW sidewalls during the electroless etching process, which was made more evident by the observation of the neck formation when transitioning to different etching regime during the SiNW formation. A method was demonstrated for the conversion of hooked SiNWs into sharp nanocone structures by simple oxidation and etching. Furthermore, SiNW tip-clumping could be regulated by adding a small amount of NaCl, which is attributed to a reduced metal-assisted etch rate resulting from electric screening of the charged Au surfaces. Common electrolyte can also be used as a retardant for the metal-assisted electroless etching.

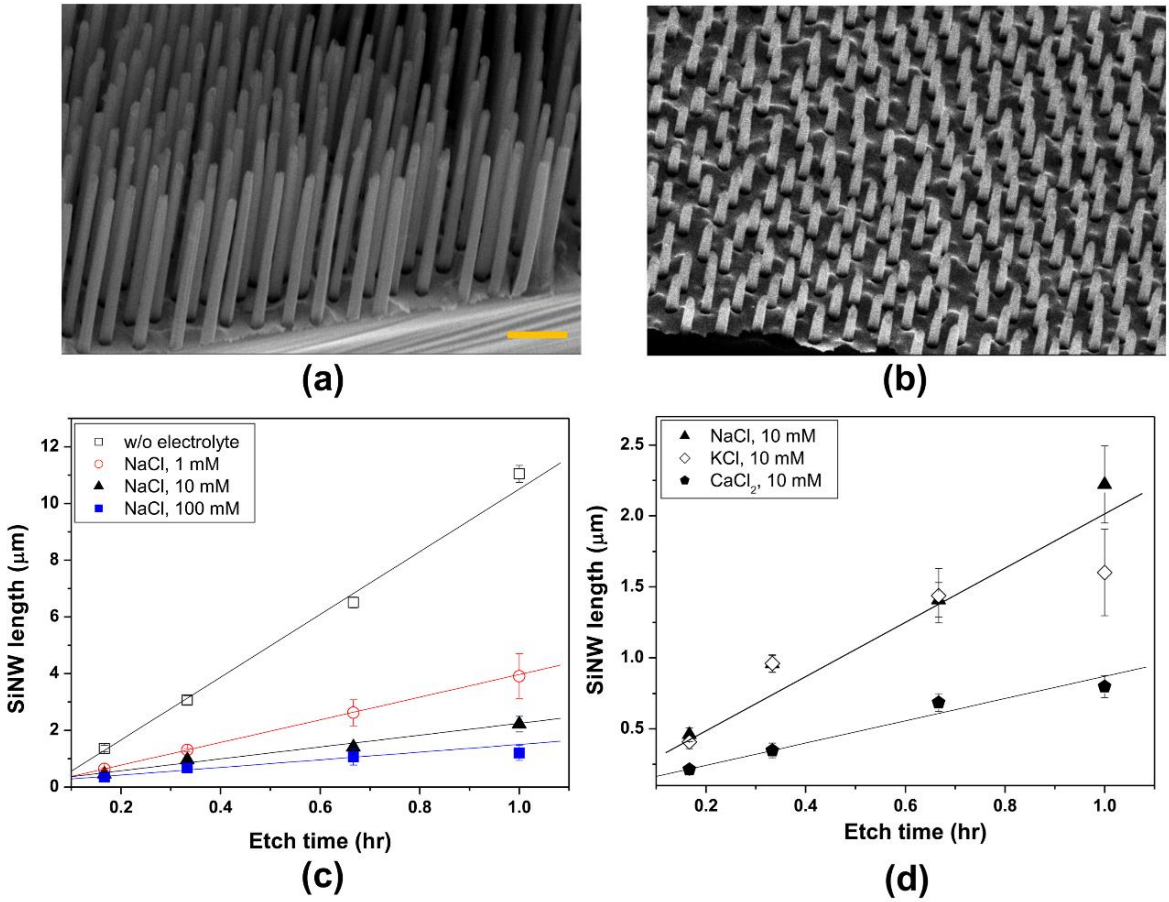

Figure 6.5: SEM images of SiNWs prepared with etching solutions of $HF/H_2O_2/H_2O$ (time) = 1.8/0.2/8.0 (40 min, regime I) – (a) without NaCl, and (b) with NaCl (10 mM) (45° tilt view, scale bar = 2 μm). SiNW lengths were plotted against the etching time for different NaCl concentrations (c), and for different electrolytes (d).

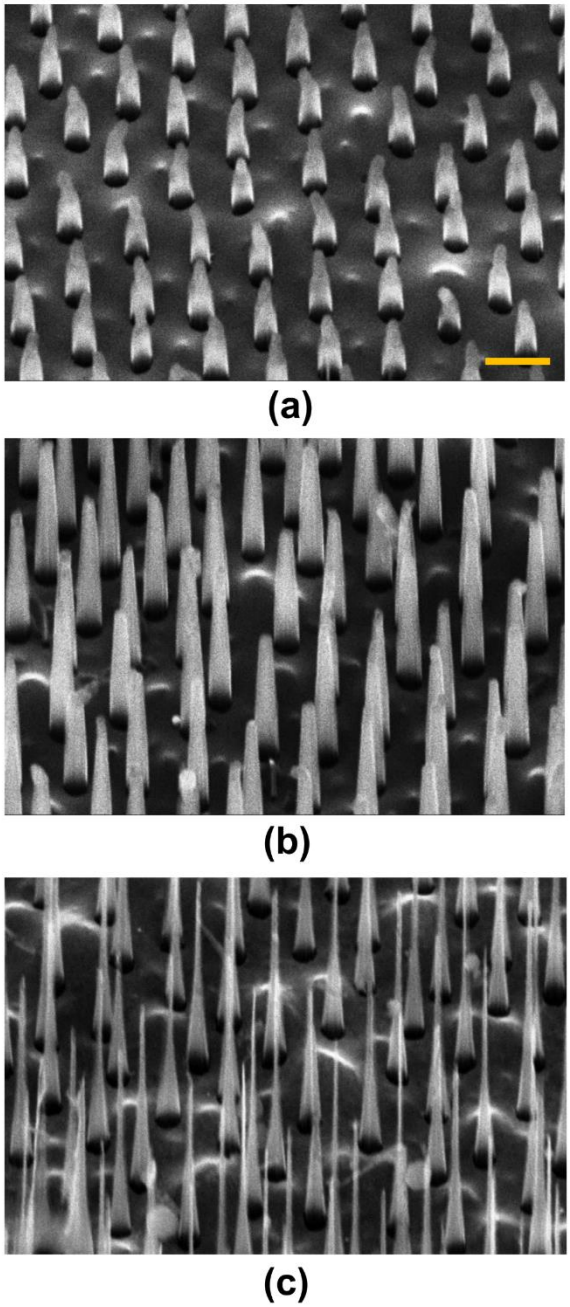

Figure 6.6: SEM images of SiNWs prepared with NaCl-loaded (10 mM) etching solutions of $HF/H_2O_2/H_2O$ (time) = (a) 1.2/0.8/8.0 (10 min) and (b) 1.5/0.5/8.0 (30 min). The SiNWs are unclumped and tapered unlike the hooked structures observed without NaCl. (c) Extended etch time of 60 min with etch solution in (b) results in a long, spear-like nanostructure (45° tilt view, scale bar = 1 μm).

6.2 Controlling directionality and curvature of SiNWs by addition of co-solvant

This section contains material from the following publication with permission from the contributing authors: Y. Kim, A. Tsao, D. H. Lee, R. Maboudian. Solvent-induced formation of unidirectionally curved and tilted Si nanowires during metal-assisted chemical etching. *J. Mater. Chem. C* **2013**, *1*, 220-224. <http://dx.doi.org/10.1039/C2TC00041E>. Reproduced by permission of The Royal Society of Chemistry (RSC).

In metal-assisted chemical etching, the reaction bath often contains wetting agent or co-solvent (usually methanol or ethanol) as a practical means to improve the overall etching uniformity of the samples. While the ratio of HF to the oxidizing agent is known to dramatically affect the porosity and the crystallographic direction of the SiNWs [73], the effect of wetting agent in the resulting morphology of SiNW formed by metal-assisted chemical etching has received limited attention [124, 125]. Chiappini et al. [124] has reported that the inclusion of ethanol with HF and H_2O_2 slows down the etching rate and affects the porosity of the resulting morphology. The Si(100) substrates etched with Ag nanoparticles obtained by electroless deposition formed solid or porous vertically-aligned SiNWs, in some cases on top of a porous silicon layer, depending on the concentration of ethanol and resistivity of the starting wafer. In a study of pore formation by Si etching in HF/H_2O_2/ethanol mixture using thin Au film as the metal catalyst, Chen et al. [125] observed that the etching rate is significantly decreased with increasing amount of ethanol.

This section examines the effect of the concentration and the type of co-solvent on the morphology of SiNWs formed via colloidal lithography and metal-assisted chemical etching. The study expands the concentration range of the conventional wetting agents (namely methanol and ethanol), and also examines other solvents such as 2-propanol and acetonitrile whose effects have not been specifically studied in metal-assisted chemical etching of Si. It is shown that inclusion of co-solvent can influence the *etching direction* as well as the etching rate, resulting in the formation of non-vertical SiNWs. In addition, the fabrication of unidirectionally slanted or curved SiNW array over a large area (on the order of 50 cm^2) is demonstrated, with control over the curvature of the wires to produce SiNW arrays that are either tilted or curved in the same direction. Such non-vertical arrays have shown to present some advantages over the typical vertically-aligned SiNWs, for example in improved electrode contact with excellent anti-reflective properties for solar cells [126]. The current methods for fabricating slanted SiNWs generally rely on the HF/oxidant ratio of the etching bath [116, 127, 128] or the orientation of the starting wafer [126, 129, 130, 131]. As such, this study presents a simple alternative to fabricate unidirectionally-aligned SiNW, either slanted straight or curved, only by controlling the amount of co-solvent added in the etching bath.

6.2.1 Co-solvent and directionality of SiNWs

The SiNWs in this section is 400 nm in diameter, 500 nm in center-to-center spacing, and varies in length depending on the etching condition and duration. They are fabricated in the similar

manner as explained previously, and an additional amount of various organic solvent is added to the etching bath prior to etching. As such, the bath contains HF (48%, EMD), H_2O_2 (35%, Fisher Scientific), DI water (18 MΩ), and an additional solvent (methanol, ethanol, 2-propanol, or acetonitrile, Fisher Scientific). For a 5 × 5 mm^2 chip, the total volume of solution is 10 mL. The amount of HF and oxidant (H_2O_2) are fixed at 2 and 1 mL, respectively, while the ratio of water and co-solvent are varied. From here on, we denote the volume composition as the ratio HF : H_2O_2 : water : co-solvent.

Figure 6.7a shows a representative scanning electron micrograph (SEM) of Si(100) substrate exposed to etching bath containing only HF, H_2O_2, and water (i.e., HF : H_2O_2 : water:co-solvent volume ratio of 2 : 1 : 7 : 0) for 10 min. Under this etching condition, highly clumped SiNWs are observed. Such morphology coincides with increased porosity of the SiNWs at high concentrations of H_2O_2 relative to HF. As discussed above, under these conditions the excessive amount of holes injected into Si by the oxidizing agent can diffuse to the sidewalls of the SiNWs and create nano-porous portion of wires that can clump. Nonetheless, the etching direction is vertical with respect to the substrate, as can be seen from the unclumped base of the wires and the fact that the porous top sections are bent to form groups with no particular orientation or alignment.

Upon a significant addition of methanol at concentrations higher than the ratio HF : H_2O_2 : water : methanol = 2 : 1 : 4 : 3, formation of some non-vertical wires is observed, as shown in Figure 6.7b (2 : 1 : 2 : 5 ratio is given as a representative condition at 20 min of etching). Clumping is also no longer observed, suggesting that the porosity has been reduced even though the ratio of H_2O_2 to HF is constant. Finally, a drastic reduction in the etch rate can be seen in comparing Figure 6.7a and b, i.e., while they are similar in length (~6 μm), the case without the co-solvent took only half the time in the etching bath. Addition of ethanol also results in non-vertical wires, although the amount required to induce the formation is found to be less (2 : 1 : 6 : 1).

Previous reports in the literature regarding the formation of slanted SiNWs are rather conflicting. While many studies [126, 129, 130, 132, 133] report <100> is the favored etching direction (which would suggest that non-vertical SiNWs only form on wafers with orientation other than (100)), preferential etching towards other directions has also been reported on Si(100) substrate [116, 127]. Some have reported the etching simply follows the orientation of the starting wafer, always resulting in the vertical etching direction [134, 135]. Other factors, such as the etching rate [127], the geometry of the catalyst pattern [113], and diffusion rate of the reactants [136], have also shown to be critical parameters in etching direction, further complicating the prediction of resulting directionality of the SiNWs in metal-assisted chemical etching.

Nevertheless, consistent with the studies on ethanol-containing etching bath by Chiappini et al. [124] and Chen et al. [125], the overall etching rate decreased with the increased concentration of the co-solvent. As co-solvents typically have low surface tension, it is likely that locally at the reaction sites, co-solvents are preferably wetted and limit the availability of reaction species HF and H_2O_2, resulting in slower etching rates. It may be speculated that while the <100> direction is often observed to be the preferred etching direction since the number of Si back-bonds that have to be broken is the lowest [137], significant reduction of the etching rate may suppress the

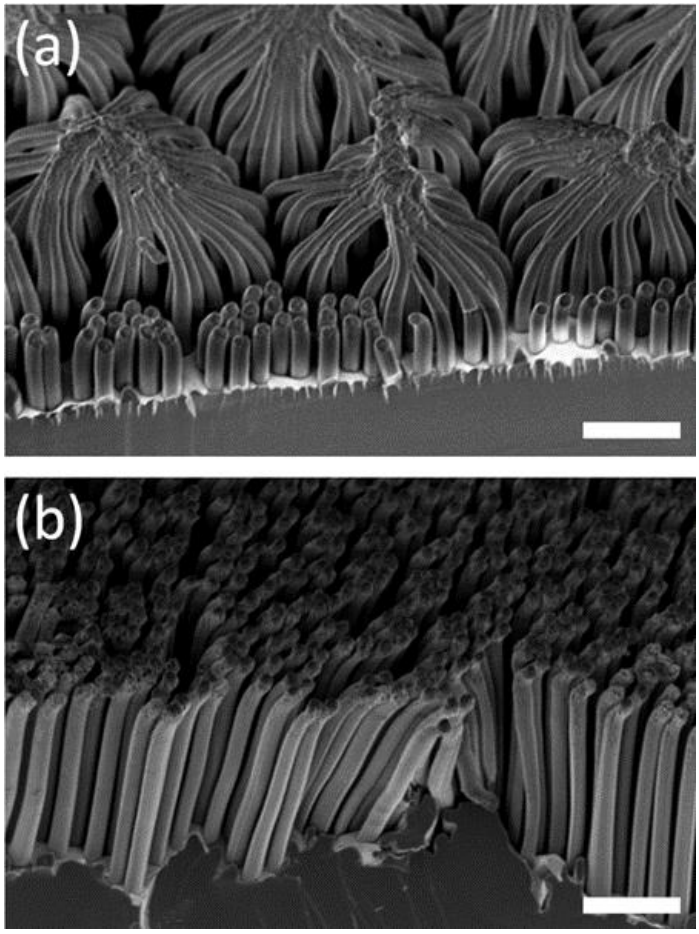

Figure 6.7: Scanning electron micrograph of SiNWs etched in solutions composed by volume of a) HF : H_2O_2 : water = 2 : 1 : 7 for 10 min and b) HF : H_2O_2 : water : methanol = 2 : 1 : 2 : 5 for 20 min. With the addition of wetting agent, non-vertical wire formation is observed. Both scale bars = 2 μm.

vertical etching and allow etching towards other major crystallographic directions or some vector combination of them. In fact, Chern et al. [116], in a study that correlated the HF to H_2O_2 ratio to SiNW orientation resulting from Ag-assisted etching, has suggested that higher relative concentration of HF can allow etching in directions other than <100>, as HF becomes more readily available to remove the oxidized Si. Similar phenomenon may occur for our case if H_2O_2 is more severely shielded from reaction sites by co-solvent than HF is, possibly due to the higher surface tension of H_2O_2, effectively increasing the HF to H_2O_2 ratio locally. Lower local concentration of H_2O_2 may then explain the reduction of SiNW porosity (due to reduced density of injected holes), non-vertical etching (due to higher HF/H_2O_2 ratio), and reduced etching rate (due to overall decreased availability of reactants). Finally, another possible mechanism for non-vertical etching may be electrophoresis, in which the self-induced field across the metal during the etching motivates the movement of the catalyst pattern [131]. This mechanism has been suggested to explain 3-D etching of Si, where metal particles moved in various directions during etching depending on their shapes and sizes [121, 138]. However, the nature of such forces acting on the catalyst particle during metal-assisted etching is not well known, and it is uncertain whether it contributes significantly to our system.

6.2.2 Etching uniformity and SiNW curvature

While incorporating methanol and ethanol induced formation of non-vertical wires, the etching uniformity of SiNW morphology over large-area (for the ~5 × 5 mm^2 sample) was poor for these two systems. The substrates etched with methanol show a mixture of vertical and non-vertical wires, while the domain size (corresponding to the length-scale of regions containing SiNWs leaning in the same direction) remains very small (several micrometers to tens of micrometers) for those etched in ethanol. Upon substituting with 2-propanol, the formation of non-vertical SiNWs is again observed, but with a remarkable improvement in the domain size and uniformity. Specifically, a small addition of 2-propanol (2 : 1 : 6 : 1, Figure 6.8a) produces curved SiNWs that are unidirectional over a large area (in the range of several millimeters to centimeters for larger samples). Increasing the concentration of the co-solvent reduces the curvature, producing almost straight, tilted SiNWs (Figure 6.8b), while preserving the large domain size. It is noteworthy that such a simple approach in varying the type and concentration of an additional solvent in metal-assisted chemical etching not only yields a highly ordered SiNW array that is unidirectional over a large area, but also afford control over the curvature of the resulting wires.

Using acetonitrile as the co-solvant yields similar unidirectionality over a large area, however with more severe curvature (as shown in Figure 6.8c) over a large variation in concentration (2 : 1 : 5 : 2 – 2 : 1 : 2 : 5). Thus, by simply selecting between the two solvents, 2-propanol and acetonitrile, consistent fabrication of unidirectionally angled, either with or without high curvature, could be achieved over large areas.

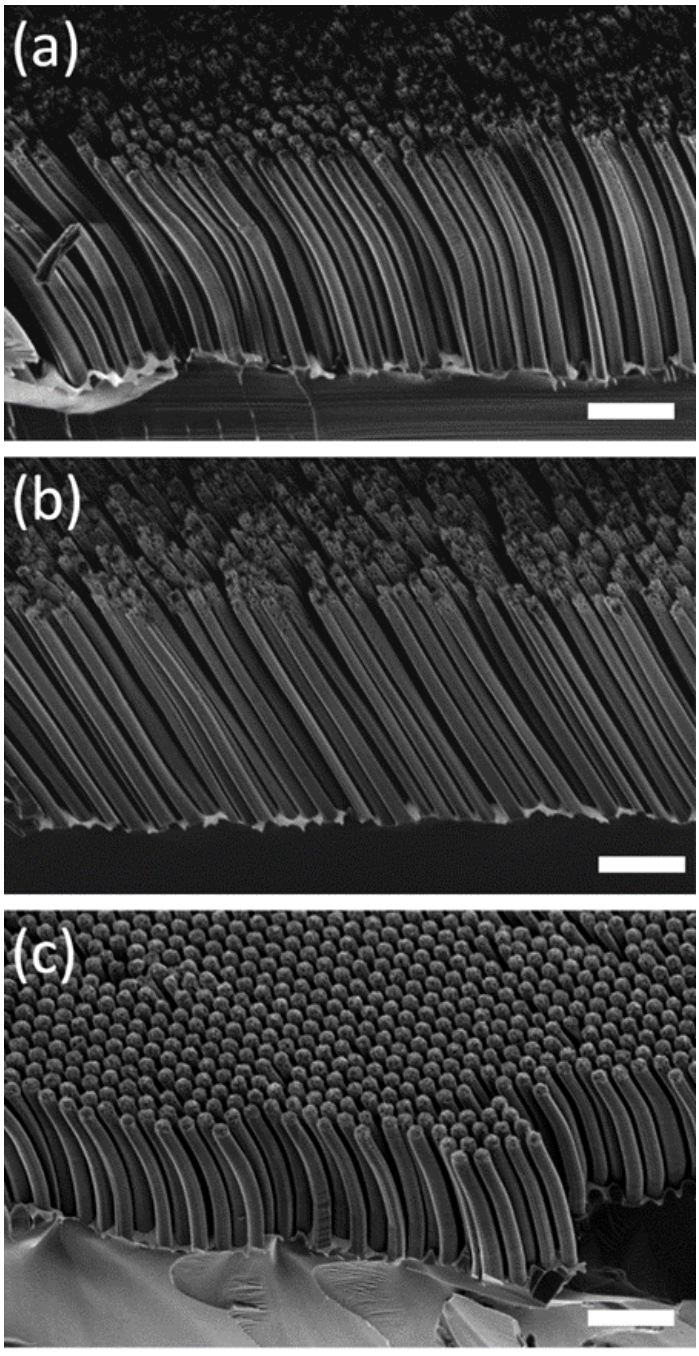

Figure 6.8: SEM images of SiNWs etched for 20 min in HF : H_2O_2 : water : co-solvent a) 2-propanol 2 : 1 : 6 : 1 mL, b) 2-propanol 2 : 1 : 5 : 2, and c) acetonitrile 2 : 1 : 5 : 2. Unidirectional SiNWs that are curved or tilted can be fabricated by controlling the type and concentration of additional co-solvent. All scale bars = 2 μm.

To look more closely into the etching process that leads up to the curved or tilted SiNWs, selected conditions (2 : 1 : 5 : 2 acetonitrile for curved and 2 : 1 : 5 : 2 2-propanol for tilted SiNWs) are observed at various etch times. For the curved SiNWs, formation appears to start with etching at a relatively steep angle with respect to the substrate (Figure 6.9a at 5 min of etching), and gradually becomes more vertical (Figure 6.9b and c at 10 and 15 min, respectively), resulting in the observed curvature of the SiNWs (Figure 6.9d at 20 min). For tilted SiNWs, the earlier stages show straight slanted NW formation (Figure 6.9e and f at 5 and 10 min of etching, respectively), as is expected. The varying wire curvature suggests that the inclusion of additional solvent may affect the diffusion and the solubility of species in the narrow regions between the nanowires. As the etching progresses and the etch depth increases, it is possible that the solvent molecules have limited penetration, resulting in a more vertical etching. Adding excess co-solvent may minimize this effect as observed for 2-propanol in going from the ratio 2 : 1 : 6 : 1 (Figure 6.8a) to 2:1:5:2 (Figure 6.8b). However, for acetonitrile, which has higher surface tension ($\gamma \sim 29$ mJ/m^2) than 2-propanol ($\gamma \sim 22$ mJ/m^2), even an excess amount at the ratio of 2 : 1 : 0 : 7 produced curvature, suggesting that the wettability of solvents may be an important factor in the local composition of the etching bath. In attempt to reduce the possible non-uniform dispersion of chemical species, one case that produced unidirectionally curved SiNW (2 : 1 : 6 : 1 2-propanol) was repeated with vigorous stirring of the etching bath during the SiNW formation. This resulted in elimination of the curvature, producing wires similar to shown in Figure 6.8b showing that diffusion may play a critical role in determining the curvature of the etching SiNWs. At this point, however, the exact origin and mechanism of solvent-induced directional etching, curvature, and uniformity remain speculative and highlight the complexity and yet striking features of metal-assisted etching of silicon.

6.2.3 Summary

The results presented offer a practical solution for large area fabrication of unidirectionally curved or tilted SiNWs. In some cases (e.g., addition of 2-propanol at the concentration of 2 : 1 : 4 : 3), the NWs could be fabricated to tilt the same direction across a large portion (> 1/2) of a 4-inch Si wafer, showing promise for an easy scale-up of the process. The size of the substrate or the bath did not seem to significantly affect the observations given above. Other factors, such as the wafer resistivity and orientation, could dramatically affect the resulting morphology. In summary, a simple approach was presented for fabricating and controlling the morphology of unidirectionally curved or tilted SiNWs via metal-assisted chemical etching. By inclusion of various co-solvants, formation of aligned NWs with control over the curvature and interesting morphologies could be observed over a large area. As unique electronic, thermal, and optical properties of SiNWs, in particular angled SiNWs, are elucidated and more applications found, this approach will prove useful in their fabrication. Various SiNW geometry obtained in Section 6.1 and 6.2 should also prove useful as templates for further processing into GSAs, and the effect of complex geometrical parameters, such as tilting angle, curvature, and tapering of polymer nanofibers can potentially be studied to provide additional insights into fibrillar interface.

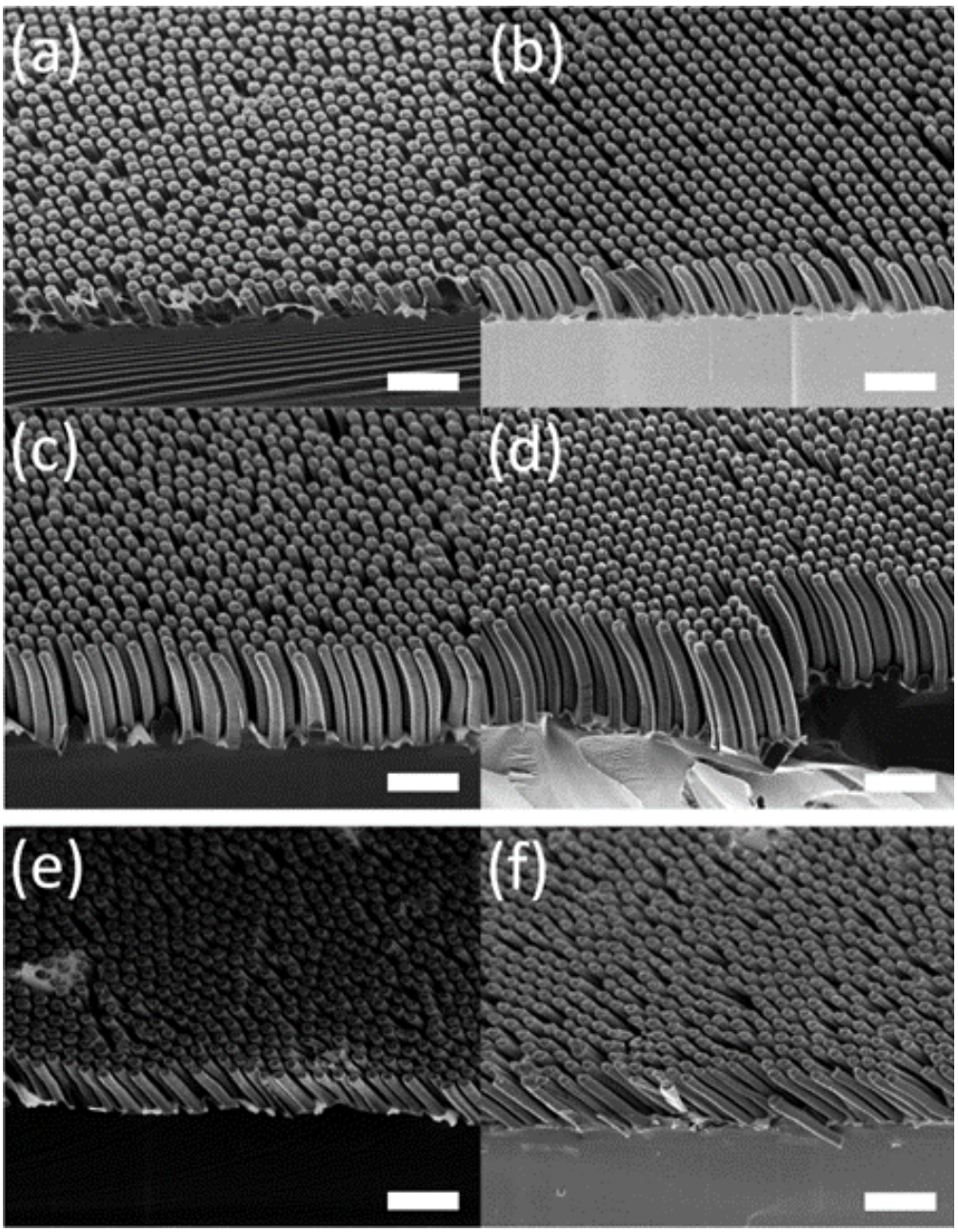

Figure 6.9: (Top two rows) SEM images of curved SiNWs formed in 2 : 1 : 5 : 2 acetonitrile after (a) 5, (b) 10, (c) 15, and (d) 20 min of etching. Gradual change in etching direction is observed. (Bottom row) Images of tilted SiNWs formed in 2 : 1 : 5 : 2 2-propanol taken after (e) 3 and (f) 5 min of etching. The wires are straight from the initial stages of formation. All scale bars = 2 μm.

6.3 Fabrication of hierarchical structure

As introduced in chapter 1, gecko foot-hairs are hierarchical in design, ranging from milli- to nano-meter scale. The hierarchical design allows adaptation to various levels of roughness found in nature's surfaces [7]. We have seen the limitation of single-level nanofibrillar adhesive, in particular with respect to the clumping behavior that curtails the performance beyond a certain aspect ratio. In order to allow the fiber elements a larger range of displacement, nanofibers can be placed on top of micropillars that can appropriately adjust to larger sized asperities. Such designs are faced with additional fabrication challenges, although recent studies have demonstrated various methods of fabrication [29, 49-56, 58, 59]. Here, a few alternative methods of hierarchical silicon template are presented, where the methods extend on the SiNW fabrication by metal-assisted chemical etching. After explaining the fabrication process of the templates, thermoplastic molding on the templates and friction testing results are presented.

6.3.1 Hierarchical silicon micro-/nanowires by double patterning of metal catalysts

As colloidal lithography can cover a large range of pattern size (few tens of nanometers to tens of microns), the most intuitive way to fabricate hierarchical structure using metal-assisted chemical etching is to simply pattern and etch micropillars first, followed by another patterning and etching of nanofibers (Figure 6.10a). This method, however, has a critical problem that the tips of the micropillars are damaged during etching due to hole diffusion (the mechanism was discussed in detail in section 6.1). As a result, the interface between catalyst and silicon is not well defined for the second patterning step, and the final etched structure is a roughened silicon surface, rather than a regular pattern of nano- and micro-wire array. The order of patterning can be reversed (Figure 6.10b), but the silicon-catalyst interface is again ill-defined. As an alternative approach, the two catalyst patterning steps can be combined into one step, as shown in Figure 6.10c. The key here is to have two different catalyst metals for the two patterns, which can be selectively removed. Both the nano- and micro-patterns are etched first, then the catalyst metal for the nano-pattern is selectively removed. The remaining micro-pattern can be further etched to produce a hierarchical silicon wire array. In this case, silver is chosen as the nano-pattern catalyst, and gold is used for the micro-pattern. Silver can easily be removed by nitric acid, which has little effect on gold. An example of silicon structure fabricated by this method is shown in Figure 6.11.

While this method is potentially viable for producing templates for a hierarchical GSA, there are several limitations. The adhesion between the micro-patterned catalyst and silicon seems to be much weaker than that between nano-pattern and silicon. This is true even when the same catalyst material is chosen for both, although the reason is unclear. As a consequence, much of the catalyst layer is delaminated during either the sonication step for the sphere removal or the etching step. A relatively well-defined structure as shown in Figure 6.11 is found in only a small region of the

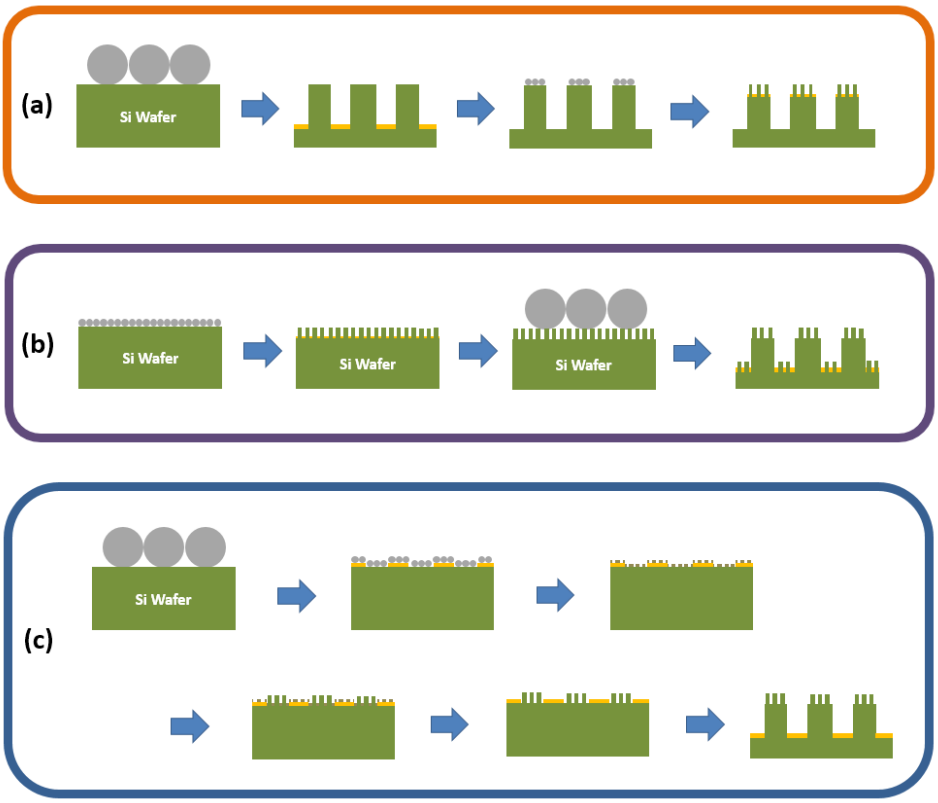

Figure 6.10: Three approaches for applying colloidal patterning and metal-assisted chemical etching of Si to produce hierarchical micropillar and nanowire array. (a) Micropillars are first etched followed by patterning and etching on top of the pillars. (b) Nanowires are first etched, followed by patterning and etching of micro-pillars. (c) Nanoscale colloidal patterning is done on top of microscale patterns, using two different catalysts. Nanowires are etched, and the nanoscale catalyst pattern is selectively removed. The remaining micropatterned catalyst is further etched.

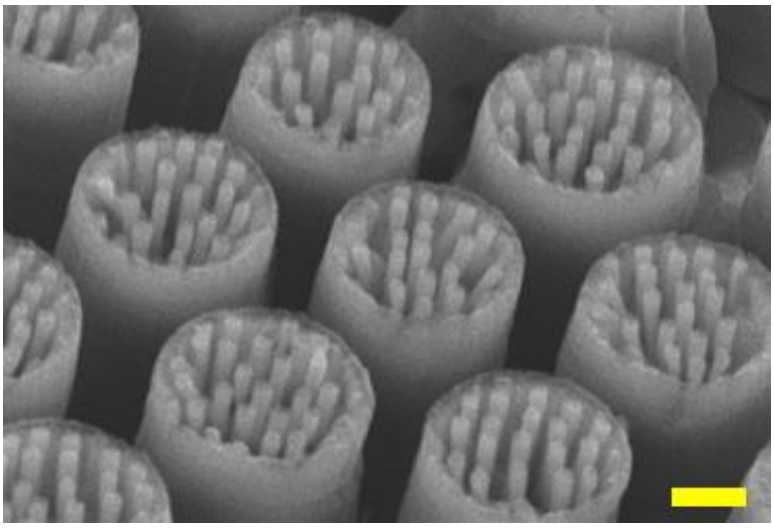

Figure 6.11: An example of hierarchical silicon structure etched by method (c) in Figure 6.10. Scale bar = 2 μm.

entire sample. In addition, the silver removal step using nitric acid may create an unwanted silicon oxide layer between the silicon and the remaining catalyst, which can prevent etching of the underlying silicon. Even when etching begins properly in some limited region, it is observed to slow down and stop at some point, suggesting that metal-assisted chemical etching of features much larger than a few microns may not be appropriate.

6.3.2 Hierarchical base microstructures by deep reactive ion etching

The experimental observations above indicates that more viable method for etching micro-structures should be investigated. To this end, more conventional photolithographic patterning and subsequent Bosch process for plasma etching of silicon is potentially more appropriate. Because photomask patterned by e-beam can be costly, we use a cost-effective alternative in which chromium is evaporated onto a blank photomask through a plastic mesh (McMaster-Carr) whose square holes are 10 μm in width (Figure 6.12a). A positive photoresist (Fujifilm, OCG 825) is spin-coated on a silicon wafer, and an exposure through the photomask followed by development leaves an array of photoresist squares. UV-light baking hardens the photoresist for increased resistance against the subsequent plasma etching. In Bosch process, the wafer is exposed to an alternating pulse of SF_6 and C_4F_8, which etches and passivates (by fluorinated layer) the surface, respectively, in a few second cycles. The resulting etching is nearly vertical, and high aspect ratio

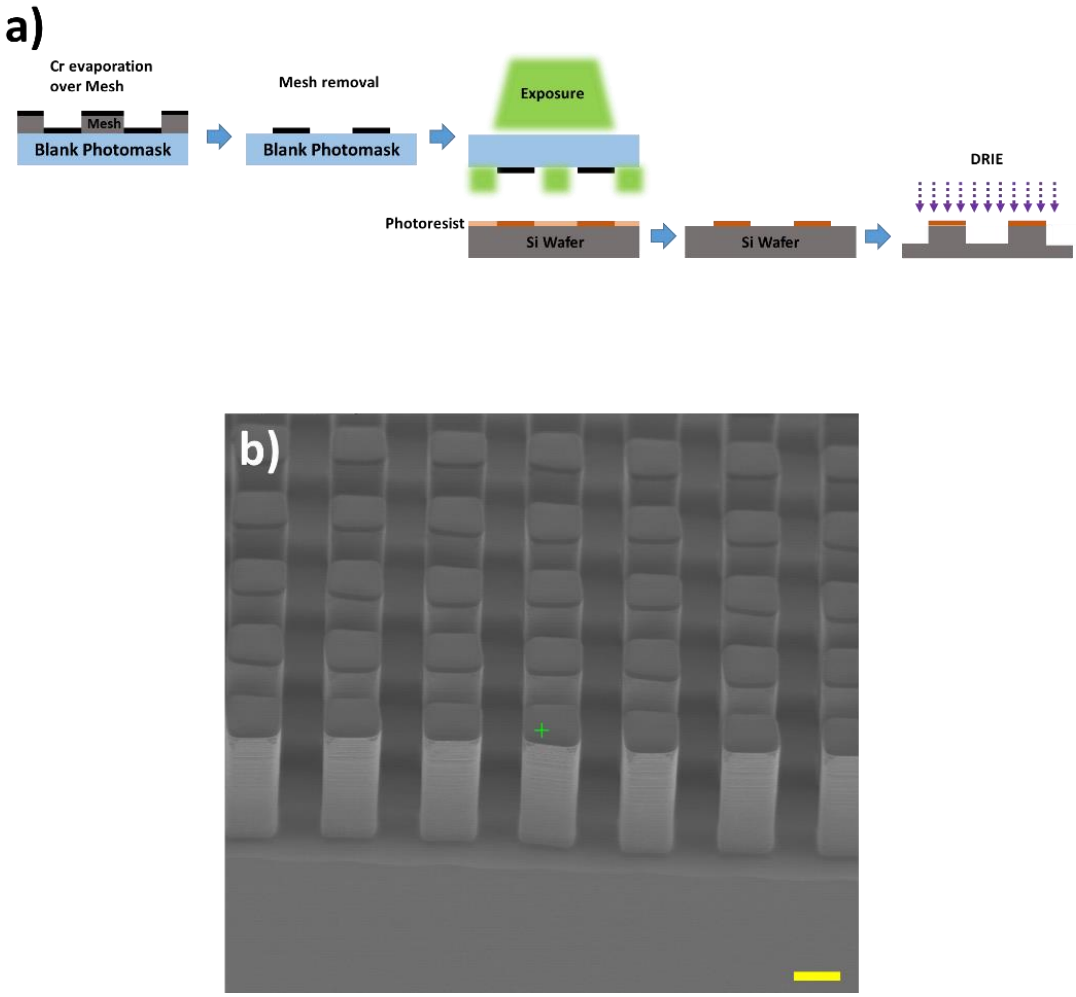

Figure 6.12: (a) Fabrication of square micropillars by photolithography and deep reactive ion etching. A blank photomask is patterned by evaporating chromium through a plastic mesh film. Exposure and development of photoresist is followed by plasma etching by alternating SF_6 and C_4F_8 gases. (b) A representative SEM image of the result. Scale bar = 10 µm.

is obtainable (Figure 6.12b). The remaining photoresist and passivating fluorinated layer can be easily removed by oxygen plasma.

Unlike metal-assisted chemical etching, this dry etching method leaves the top surface undamaged, which allows any patterning on top of the pillars to be well-defined. As such, SiNWs can be etched on top of the pillars following the same method used for single-level SiNW fabrication. A representative SEM image of fabricated hierarchical silicon structure is shown in Figure 6.13. Uniformity over entire 1×1 cm^2 chip is much improved over the previous method. The spacing, diameter, and length of the nanowires can be controlled by the size of the deposited spheres, plasma etching time for size reduction, and the chemical etching duration. The spacing and width of the micropillars can be controlled by choosing appropriate plastic mesh grades, which is available commercially over a wide rage. The length of the pillars depends on the duration of the DRIE. With independent control over the geometric parameters, the optimization for maximal friction is possible, but likely be a cumbersome task. As a preliminary test to determine whether this method provides a usable template for molding GSA, and to possibly compare friction test result to that of single-level fiber array, a few sets of geometrical parameters have been chosen. The pillar width, length, and center-to-center distance are fixed at 10 µm, 30 µm, and 20 µm, respectively. Nanofiber demensions are 800 nm in diameter, 1 µm in center-to-center distance, and $1 - 4$ µm in length. The templates are replicated into LDPE by the same method used for the single-level fibers.

Friction test result (against smooth glass, measured by the procedure described in Section 2.5) in Figure 6.13a shows that compared to single level fiber array over similar range of length, friction is much reduced for the hierarchical structure, although there is a similar increase in length as fibers become longer. This reduction in performance is expected against smooth glass, since introducing the micro-level structure effectively reduced the number of contacting elements. Close examination of the structure after friction testing also reveals that the contact is limited to the edge of the pillar, where the nanofibers are observed to have plastically deformed and collapsed due to concentrated stress (Figure 6.13b). The limited contact zone may have further reduced the performance of the adhesive. To test whether the micropillars provide any benefit to the performance of the adhesive, tests on rough surfaces would be needed to determine if hierarchical structure shows improvement in adaptability. Nonetheless, the friction result shows that moderate friction values can be obtained with the hierarchical structure molded from template fabricated by combination of DRIE and metal-assisted chemical etching of silicon.

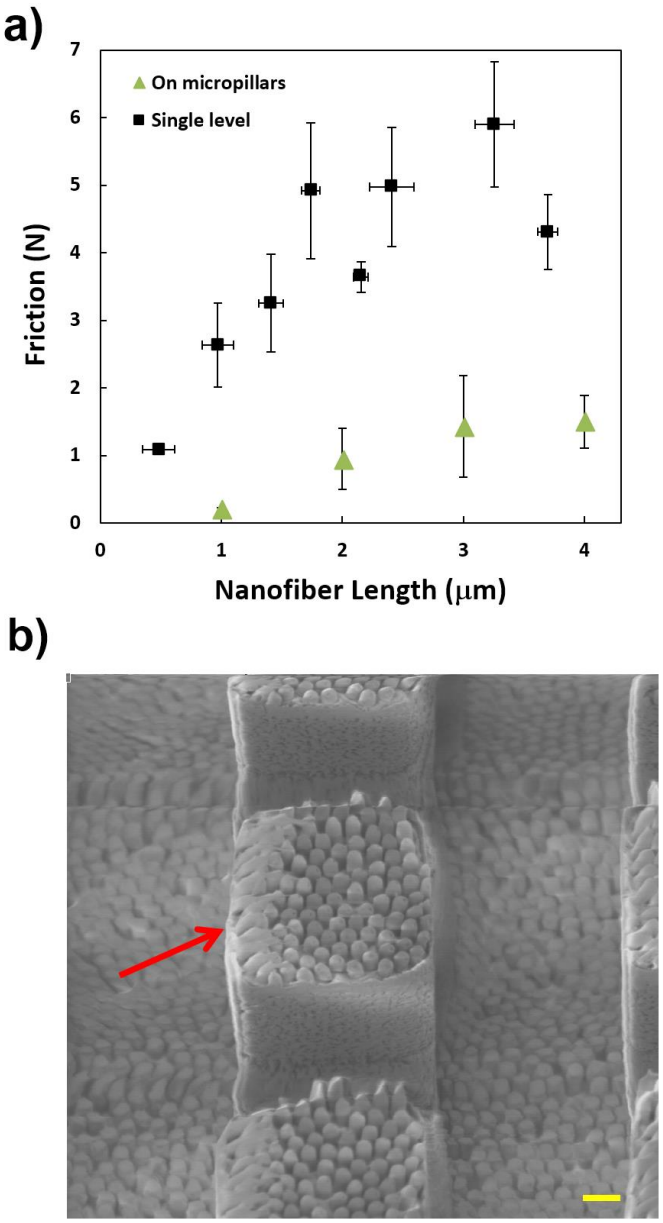

Figure 6.13: (a) Friction of LDPE hierarchical fibers (1 × 1 cm^2 patch). The pillar width, length, and center-to-center distance are fixed at 10 μm, 30 μm, and 20 μm, respectively. Nanofiber demensions are 800 nm in diameter, 1 μm in center-to-center distance, and 1 – 4 μm in length. Compared with the single-level nanofiber with similar dimensions, the hierarchical structure shows a similar trend but low friction overall due to reduced number of fibers. (b) SEM image after friction testing reveals that the contact has been concentrated to one edge of the pillar. Scale bar = 2 μm.

6.4 Fabrication of composite structure

As previously mentioned, the contacting region of the LDPE adhesive sample is limited due to the non-planarity of the film. This section explores one possible solution to this problem, which is embedding individual LDPE fibers in a softer elastomer backing. Such composite structure has potential to better adapt to a large scale roughness or non-planarity of the counter-surface, and easier integration into applications like gecko-inspired climbing robots that currently use elastomer GSAs for the adhesive feet [18-24, 26]. More rigid LDPE fiber elements can potentially provide better resistance against contamination and attachment and detachment mechanism more similar to natural geckos, whose foot-hair material is more similar in stiffness to thermoplastics than soft elastomers [17]. This section provides two methods to fabricate composite GSAs combining various lithographic techniques for both silicon and soft materials.

6.4.1 Composite structure by utilizing polycarbonate filter

The process overview for the 1st method is shown in Figure 6.14a. A commercially available polycarbonate filter with 5 μm circular holes (EMD Millipore) is attached to a cured PDMS film (Dow Corning Sylgard 184), and CF_4 plasma (Plasma-Therm PK-12 RIE, 200 W, 80 SCCM, 30 min) etches away PDMS in spots exposed by the filter holes. A 10 μm LDPE film (The Glad Products Co.) is melted onto the substrate at 160 ℃, and the top layer of LDPE is removed by oxygen plasma (Plasma-Therm PK-12 RIE, 80 W, 100 SCCM, 30 min). Another layer of PDMS is cured on top of the substrate, and the original PDMS film is peeled away, leaving LDPE pillars embedded in the second PDMS layer. An SEM image of the resulting structure is shown in Figure 6.14b. The distribution of pillars are quite random due to the random distribution of the holes in the filter. Also, because PDMS etching in CF_4 is slow and limited in anisotropy, the aspect ratio is obtainable is low. To confirm that the fabricated structure is LDPE/PDMS (fiber/backing) composite, the sample is heated in oven to 160 ℃ (temperature at which LDPE melts, but with no effect on PDMS), which evidently melts only the fibers (Figure 6.14c). A preliminary friction result using pillars with tip diameter of 7 μm, length of 20 μm, and number density of 330000 per cm^2 shows only a small friction at 0.3 N. While satisfactory as a proof-of-concept, this fabrication process must further be optimized to produce higher aspect ratio structures with higher number density in order to bring the performance up to a reasonable level.

6.4.2 Composite structure with photolithography

An alternative approach is summarized in Figure 6.15a. The method uses the same DRIE technique explained earlier for etching the micropillar base, but the pattern is inversed. Rather than evaporating chromium through the plastic mesh onto photomask, the plastic mesh itself is used as the photomask pattern by taping the mesh directly onto a blank photomask. Chromium is still

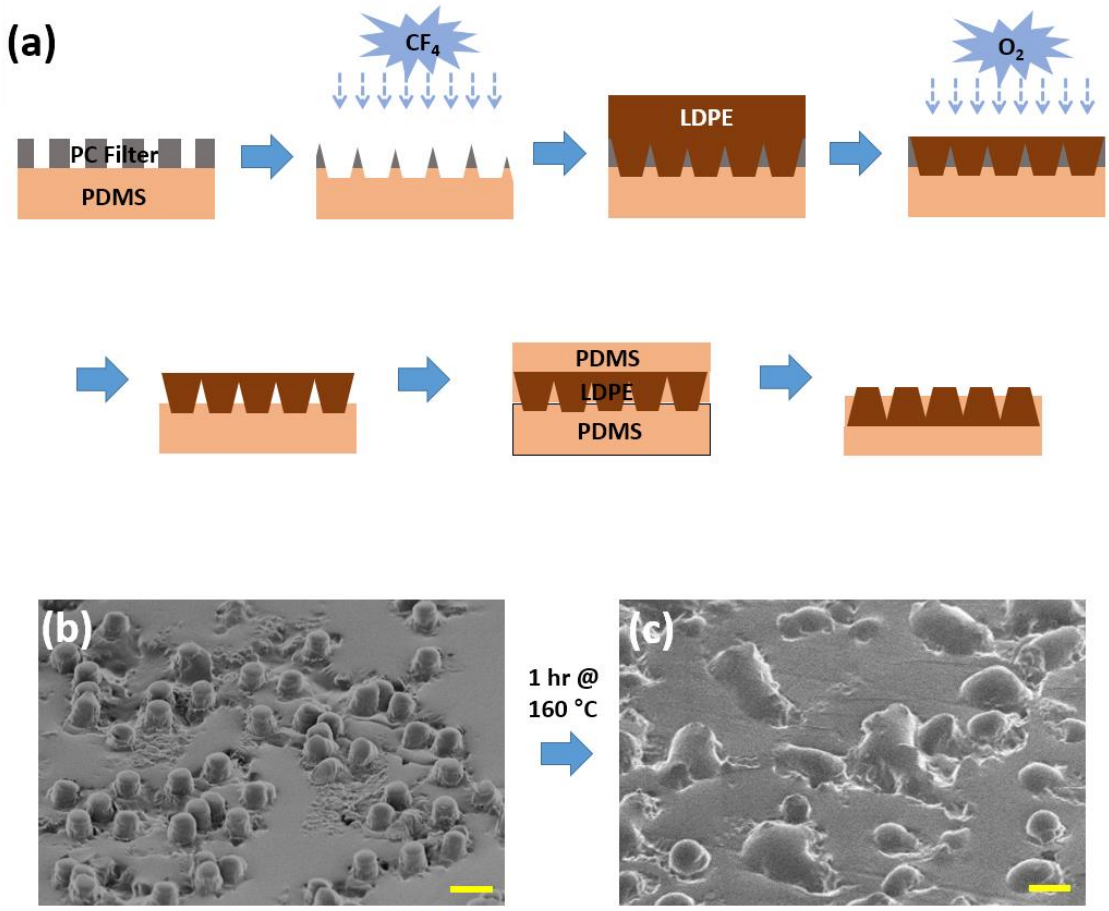

Figure 6.14: (a) Process overview of fabricating an LDPE/PDMS composite structure using a carbonate filter. PDMS is etched in spots exposed by the filter, and an LDPE film is melted on top. The LDPE layer is partially etched by oxygen plasma, and the filter is dissolved away. A second PDMS layer is cured and the original PDMS layer is peeled away. Representative SEM images of the structure after fabrication (b) and after melting the LDPE fibers (c). Scale bars = 10 µm.

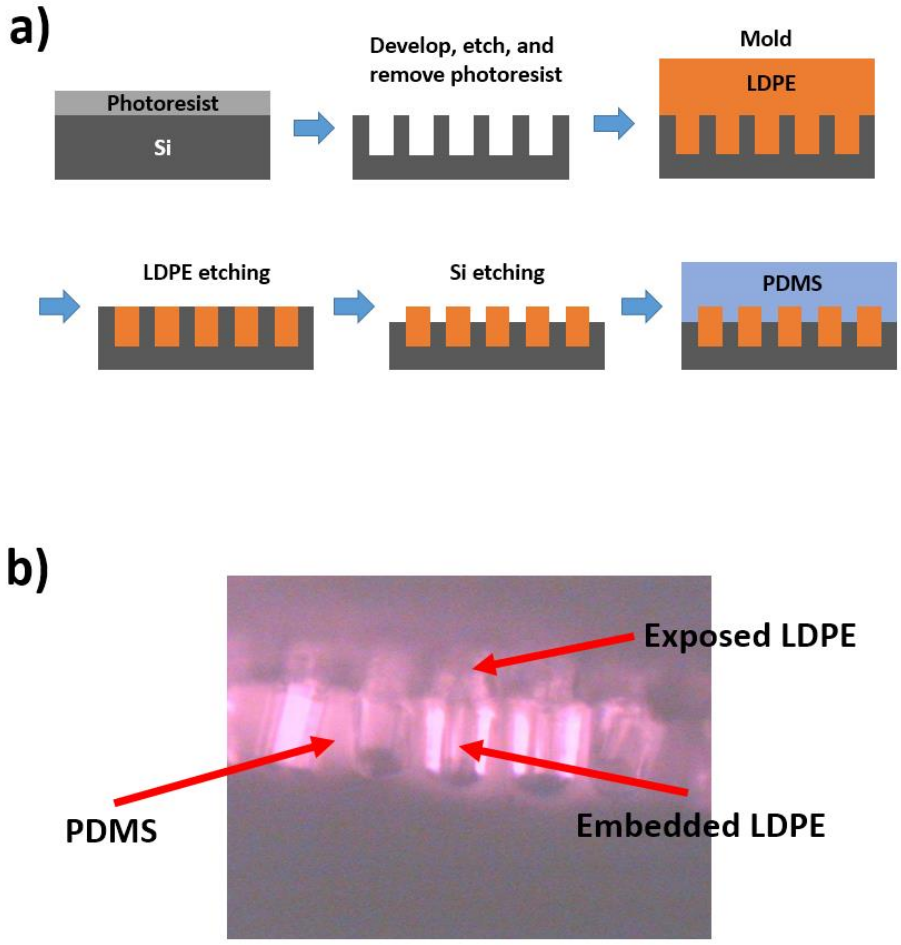

Figure 6.15: (a) Fabrication overview of an LDPE/PDMS composite structure using a silicon template obtained by photolithography. LDPE is melted onto an array of square holes, and the backing layer is etched away by oxygen plasma. Silicon etching by SF6 partially exposes the LDPE fibers, which can be embedded in PDMS. The Si template is dissolved away. (b) An optimal microscope image showing the LDPE micropillars embedded in PDMS.

evaporated on top of the plastic mesh in order to ensure that the material is opaque for the light used for the photoresist exposure. A positive photoresist (Fujifilm, OCG 825) is spin-coated onto a silicon wafer, and exposure and development produces an array of square holes in the photoresist film. A 10 μm is again molded onto the template, and the top layer is removed by oxygen plasma. The LDPE pillars are partly exposed by etching away some of the silicon template away by SF_6 + O_2 plasma. PDMS is cured on top of the substrate, and the silicon template is etched away in HNA solution to leave behind LDPE pillars in PDMS (Figure 6.15b). While the product is a much better defined array of micropillars than the first method, friction testing showed negligible adhesive strength, which suggests further improvement, e.g., higher aspect ratio, is required.

6.5 Fabrication of tapered micropillars

This section is reproduced with permission from: Y. Kim, Y. Chung, A. Tsao, R. Maboudian. Tuning Micropillar Tapering for Optimal Friction Performance of Thermoplastic Gecko-inspired Adhesive. *ACS Appl. Mater. Interfaces* **2014** <http://pubs.acs.org/articlesonrequest/AOR-6qwZVypq8JfAc2twju78>. Copyright 2014 American Chemical Society.

One geometric aspect of GSAs that has not received much attention in the literature is the sidewall tapering of the fibers. While some wedge-shaped structures have been fabricated and tested for adhesive property [139, 140], the effect of the sidewall taper has not been studied in detail. Tuning the tapering angle of synthetic gecko adhesive could be useful for optimizing adhesion and friction performance of such adhesive, as well as for exploring varied contact mechanisms dependent on the shape of the structure.

To this end, this section introduces a simple technique for precise control over sidewall tapering of silicon micropillars. A combination of deep reactive ion etching and chemical etching produces high aspect ratio silicon pillars with tunable tapering angle, depending on the chemical etching bath composition and the etching duration. A subsequent molding process replicates the structures in LDPE, and the frictional behavior is studied and related to the pillar geometry. It is shown that the tapering angle can dramatically affect the contact mechanism of pillars and the friction performance of the array, as a result of change in pillar compliance and the available contact area. Contact deformation of pillars are imaged after friction testing by SEM, and the observed contact behavior is compared with simple finite element models.

6.5.1 Fabrication procedure

An array of micropillars are first defined by the same DRIE method presented in 6.3.2 (Figure 6.16 i – iii). The pillars are then submerged in a silicon etch bath (iv) consisting of hydrofluoric acid (EMD, 48%), nitric acid (EMD, 70%), and acetic acid (EMD, 99.7%). Even without any chemical etch mask, the resulting pillar shape could be controlled simply by diluting the etching bath by deionized water. The acids are first mixed in volume ratio of 4 : 3 : 3 hydrofluoric : nitric :

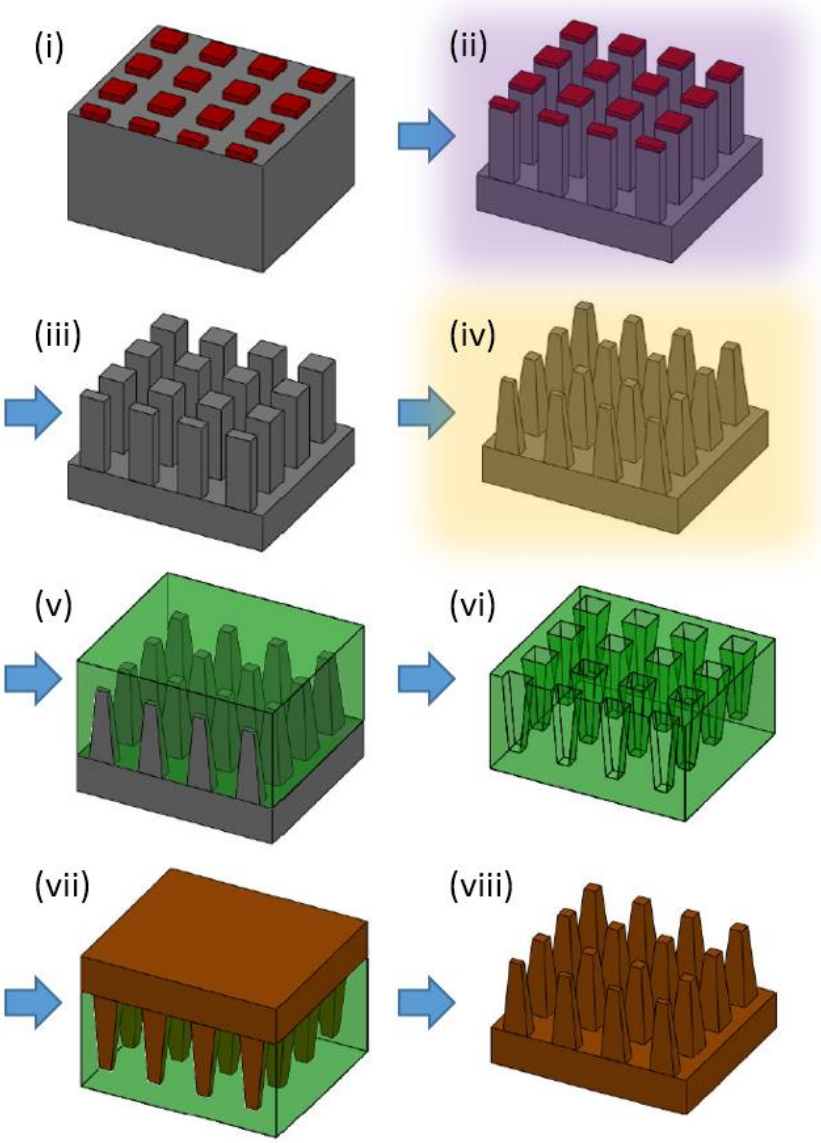

Figure 6.16: Process overview for synthesis of tapered silicon pillar templates and their replication into LDPE thermoplastic, consisting of (i) photoresist patterning, (ii) deep reactive ion etching, (iii) photoresist removal, (iv) HNA etching, (v) polycarbonate film molding, (vi) intermediate template peel-off, (vii) LDPE film molding, and (viii) dissolution of the intermediate template in a methylene chloride bath.

acetic acid (HNA). Each chip is exposed to 5 mL of the HNA solution diluted by additional amount of water (in the range from 0 to 1 mL). When the chip is submerged in the bath, the reaction proceeds to etch away the pillars from the sides and the top, producing various angles of tapering and aspect ratios depending on the amount of dilution and the duration of etching. For most cases, the etching is fast, with the time staying under 1 minute. The resulting array of silicon pillars are replicated into thermoplastic by a two-step molding process. To facilitate peel-off, each silicon template is first coated with a self-assembled monolayer by reaction with octadecyltrichlorosilane in toluene (as described in Section 2.4). Polycarbonate film (McMaster-Carr, 100 μm thick) is melted onto the silicon template in a vacuum oven at 300 ℃ for 1.5 hr (v), and the film is peeled-off after cooling (vi). When clean peel-off is not possible, the template is etched away with undiluted HNA. The intermediate polycarbonate template is used for molding low-density polyethylene film (McMaster-Carr, 100 μm) at 160 ℃ for 1 hr (vii), and the polycarbonate is dissolved away in methylene chloride bath (viii).

6.5.2 Fabricated silicon templates

Before any chemical etching, square pillars obtained by DRIE show no tapering (inset of Figure 6.17a). Side width and height are 10 and 30 μm, respectively, and the spacing between the pillars is 10 μm, corresponding to 250,000 pillar elements in a 1 × 1 cm^2 area. The square pillars become tapered by exposure to silicon etchant containing hydrofluoric, nitric, and acetic acids. This is an electrochemical reaction in which silicon is oxidized and subsequently dissolved by hydrofluoric acid with corresponding reduction of nitric acid [141], resulting in an isotropic etching of silicon in contact with the solution. Acetic acid is a commonly added to this process for moderating the reaction rate [142]. For this study, we have fixed the etchant ratio at HNA = 4 : 3 : 3 by volume, and various amount of deionized water is added for further control over the etched structure. The SEM images in Figure 6.17b – e. show silicon templates after HNA etching at various dilutions. After only a few seconds of etching in undiluted HNA solution (in 5 mL of HNA for each 1 × 1 cm^2 chip), pillars are severely tapered (Figure 6.17b). Slight dilution by water (5 mL HNA to 0.5 mL water, abbreviated as 5/0.5 from here on) results in pillars with less severe tapering (Figure 6.17c). Etching in 5/0.7 condition further moderates the tapering (Figure 6.17d), and 5/1 condition even shows slight reverse tapering (Figure 6.17e).

For more comprehensive overview of tapering development during etching, Figure 2a plots the angles estimated from SEM images at various stages of etching progression in each condition. Tapering for different etching conditions are compared with respect to volume of silicon removed since this is directly proportional to the number of atoms removed and thus indicative of the reaction rate. The tapering is increased with increasing etching time for each dilution condition (more negative for 5/1 condition, where slight reverse tapering is observed), and dilution has decreased tapering overall. Before the flat top area erodes away, the change in the pillar length is small compared to the original pillar length. However, towards the end of etching when the flat top area (or the thinnest middle for the reverse tapered pillar) has been etched away, tapering increases rapidly to leave behind low aspect ratio pyramids, regardless of dilution. These later

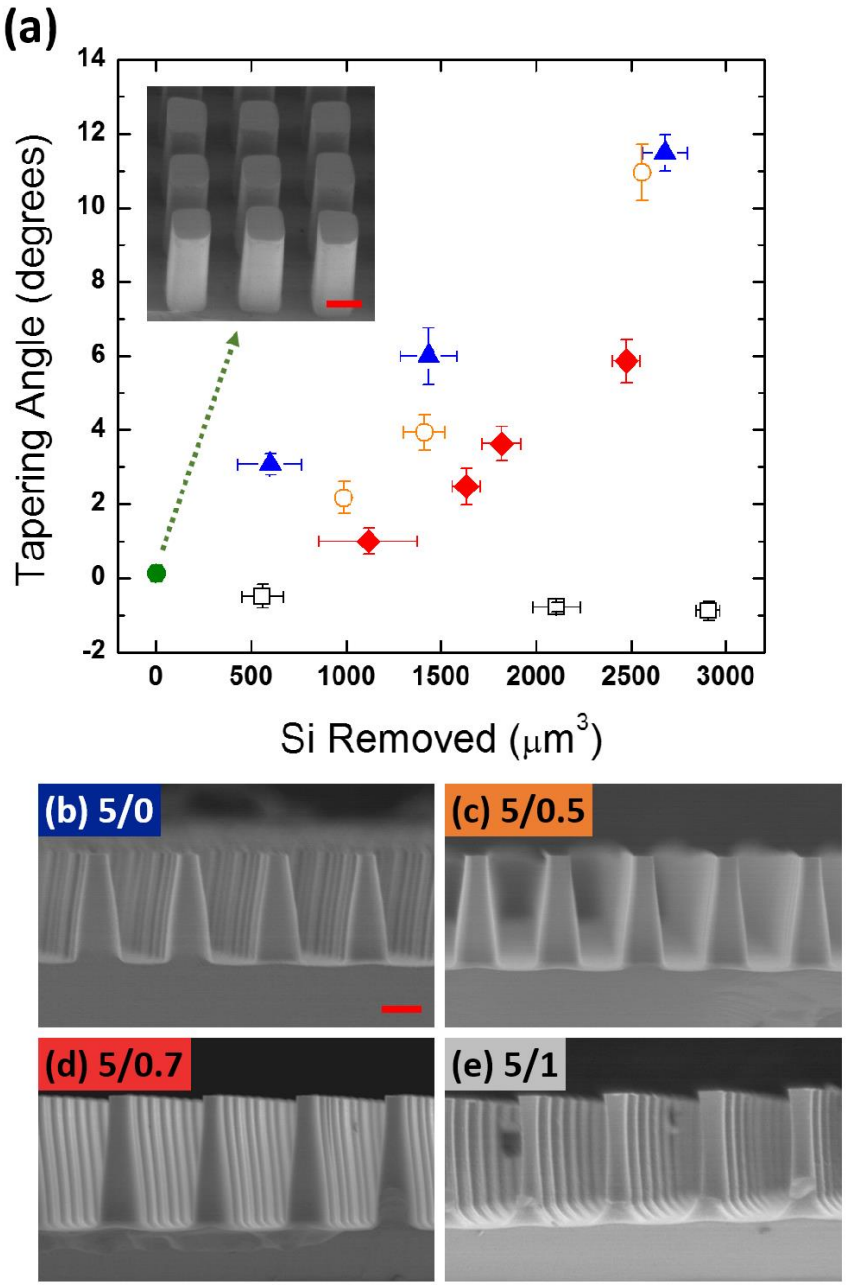

Figure 6.17: (a) Tapering angle change as silicon etching reaction in HNA progresses at different dilution amount by water (filled circle = unetched, filled triangle = HNA/H_2O = 5/0 ratio by volume, empty circle = 5/0.5, filled diamond = 5/0.7, empty square = 5/1). Inset shows an SEM image of unetched silicon pillars. Cross-sectional SEM images of (b) 5/0 – 1s, (c) 5/0.5 – 3 s, (d) 5/0.7 – 5 s, and (e) 5/1 – 15 s silicon templates.

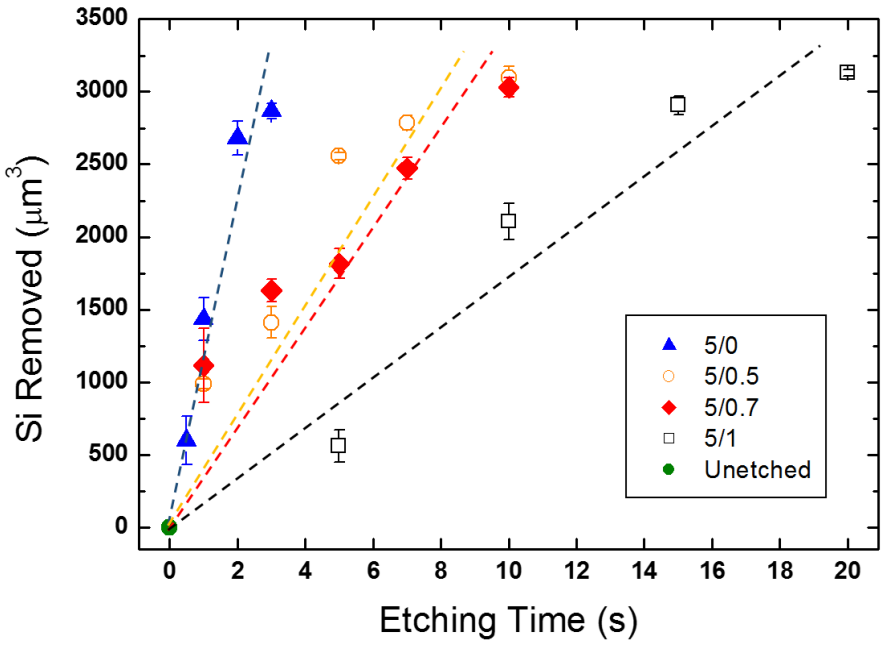

Figure 6.18: The amount of silicon removed in volume as a function of etching time for various dilution. The dashed lines are linear fits to the data, although the volume removed is not quite a linear function of etching time.

points have been omitted and only the approximately linear regime is shown. As shown in Figure 6.18, the etching rate slows with increasing dilution as expected.

While HNA solution has long been used as a silicon etchant [142], recent studies have shown fabrication of silicon architectures in micrometer lengthscale, for example pyramidal tips [143], channels [144], and needles [145], where a hardmask pattern is used to allow etching in selected regions. In contrast, it is interesting to note that the chemical etching in this study is a maskless process in which predefined pillars are exposed to etchant with no intentional masking, and simply diluting the solution allows precise control of the resulting morphology of the silicon structure. It is likely that in the case of the highly concentrated HNA bath (without dilution) with its fast etching rate, significant removal of silicon could occur near the upper portion of the pillars before the solution can progressively reach the lower portion of the pillars for complete wetting. In other words, the etching rate is relatively fast for concentrated HNA in comparison to the diffusion rate of the solution into the microchannels between the pillars, leading to the observed tapering. As the HNA solution is diluted, the etching rate slows, resulting in less severe tapering, as reported. Slight reverse tapering at high dilution may be due to non-uniform reaction rate along the depth. Because HNA etching of silicon is a highly exothermic reaction [146], temperature gradient may develop in the region between the pillars, and result in relatively slower etching of the upper portion.

6.5.3 Friction behavior of tapered LDPE pillar array

Low-density polyethylene replicas are molded from silicon templates exposed to a range of etching conditions. Dilution of water is varied from 0 to 1 mL, and the etching duration has been adjusted so that most of the silicon pillar is etched away for the longest duration for each dilution condition. The corresponding LDPE replica will be simply referred by the etching condition of the silicon template, namely the dilution and the etch time, e.g. 5/0 – 1 s. We have tested the adhesive behavior of the prepared samples by friction testing of 1 × 1 cm^2 patches, as described in section 2.5.

Figure 6.19a plots the friction behavior of LDPE pillars molded from templates etched with undiluted solution (5/0). The etching time was varied from 0 to 3 s, and the corresponding SEM images after friction testing are shown in Figure 6.19b. The unetched pillars show minimal friction (0.4 N for the 1 × 1 cm^2 patch area, equivalent of holding about 40 g of weight). Some of the pillars have a corner that has been slightly flattened where the contact with glass has been made (some pits on top of the pillars are most likely air bubbles trapped during the molding step). It is likely that the contact is limited to the corner that first touches the counter-surface due to high stiffness of the pillar that prevents any significant bending to occur. As the template is progressively etched, the pillars are thinned, then shortened after the flat top area is etched away. There is a corresponding increase in friction up to 1.2 N, then a decrease. As template etching progresses, the contact has propagated to the entire edge, and some of the pillars are observed to have an edge that has plastically flowed over the top of the pillar (Figure 6.19b – 1s). Further etching has yielded sharp-tipped pillars (Figure 6.19b – 2 s) that appear to be bent only at the top. This deformation, however, is observed for all adjacent pillars, suggesting an increase in the number of contacting elements due to higher compliance of the thinned pillars. Significantly shortened pillars (Figure 6.19b – 3s) with high stiffness is consistent with lower friction.

As the template etching bath is diluted (5/0.5), the tapering angle decreases. The corresponding friction data are shown in Figure 6.20a, where a sharper increase in friction is observed in comparison to the 5/0 set. SEM images reveal that contact deformation occurred for most of the pillars even at the earlier stages of etching (Figure 6.20b – 1, 3 s), where the plastically deformed edges are again observed at the top. Less severe tapering has led to pillars that are relatively more flexible while preserving more of the tip area. This leads to both increased number of pillars in contacting glass, as well as larger area of contact for each pillar, explaining why higher peak friction is observed for this set. Further etching has eliminated most of the tip area (Figure 6.20b – 5s), and shows how tapering can be limiting to friction due to limited contact zone. While the thinner top area is seen to be deformed from contact, thicker base prevents the deformation from propagating further. Later stages of etching again leads to shortening of pillars (Figure 6.20b – 7s), limiting the compliance and resulting in low friction.

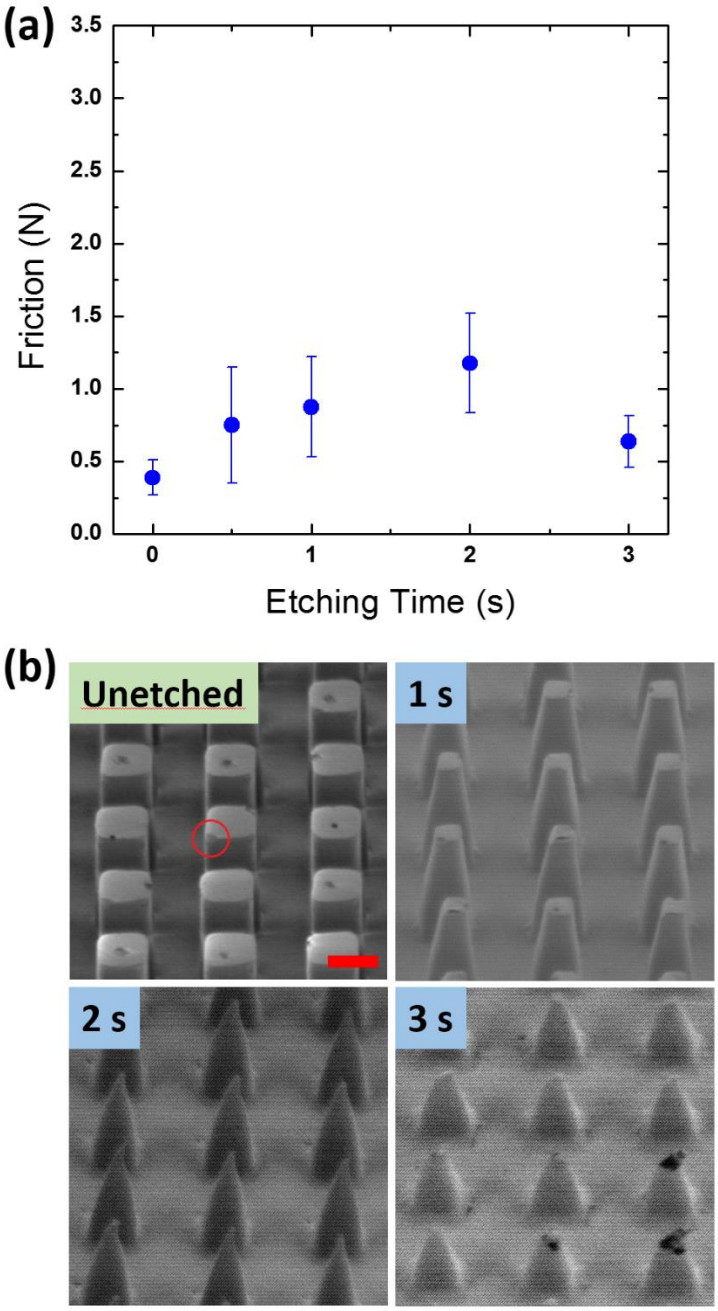

Figure 6.19: (a) Friction performance of 1 × 1 cm^2 patch of LDPE pillar array on smooth glass as template etching progresses in undiluted HNA solution (HNA/H_2O = 5/0 mL for each 1 × 1 cm^2 template). (b) Representative SEM images of LDPE pillars after friction testing for samples molded from unetched and 1, 2, and 3 s etched templates in 5/0 HNA/H_2O solution. Scale = 1 µm.

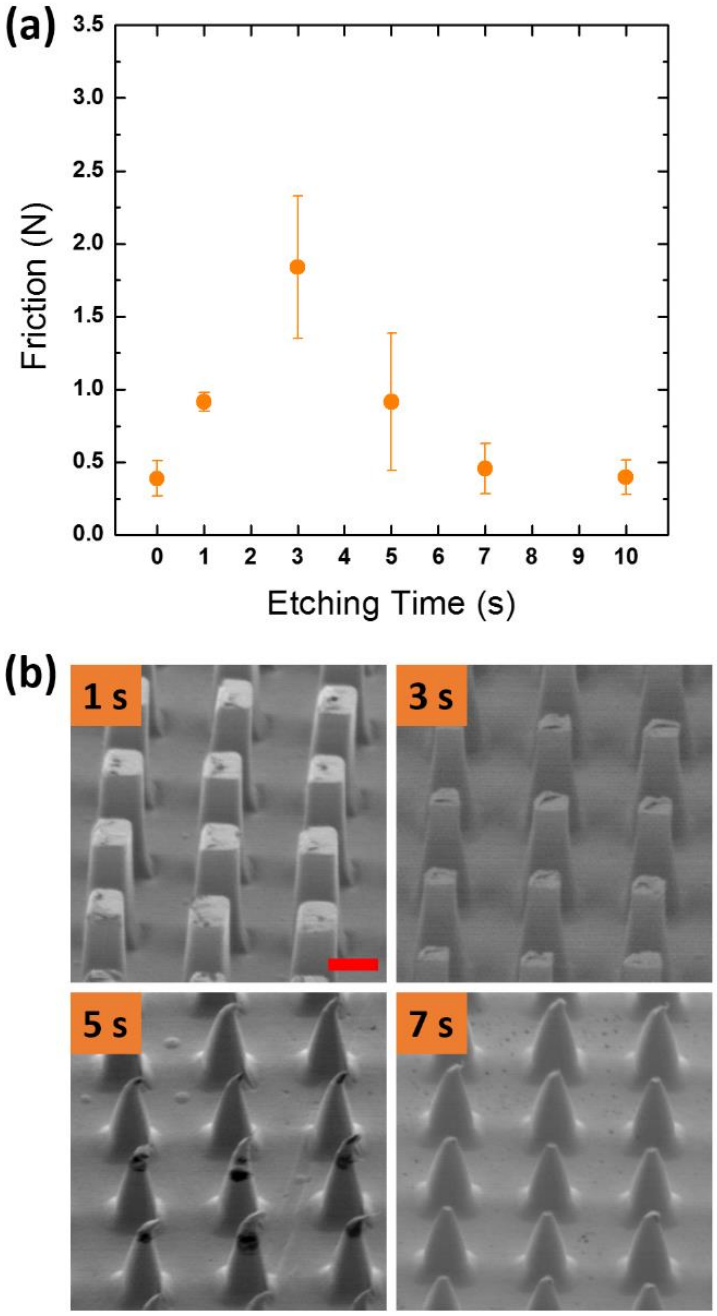

Figure 6.20: (a) Friction performance of 1 × 1 cm^2 patch of LDPE pillar array on smooth glass as template etching progresses in diluted HNA solution (HNA/H_2O = 5/0.5 mL for each 1 × 1 cm^2 template). (b) Representative SEM images of LDPE pillars after friction testing for samples molded from 1, 3, 5, and 7 s etched templates in 5/0.5 solution. Scale bar = 1 µm.

For the further diluted 5/0.7 case, the pillars are nearly vertical. The peak friction for this set has increased even further compared to more tapered cases, and higher friction is maintained over a larger range of etching time (Figure 6.21a). Reducing tapering has again led to compliant pillars with more contact area preserved at the top. The two samples with high friction (Figures 6.21b – 3 and 5s) show contact behavior similar to the sample with peak friction from 5/0.5 set (Figure 6.20b – 3s), where plastic flow at the edge occurs due to concentrated stress. The 5/0.7 – 7s sample, however, seems to maintain high friction despite having a very small top area (Figure 6.21b – 7s). Here, a large bending deformation is observed on the entire pillar, and the sides have flattened on some of the pillars, suggesting that side contact has occurred. Side-contact has been shown to increase contact zone [84], and this could also be true for our case where high friction was maintained despite the significant reduction in contact area available at the tip.

Etching in 5/1 dilution lead to pillars that are slightly reverse tapered, with thinner middle. A steep increase is observed as template etching progresses (Figure 6.22a). While it is likely that the high friction is due to the combination of increased pillar flexibility due to thinner middle and the large contact area preserved at the top, examination of SEM images for high friction samples (Figure 6.22b – 10, 15 s) reveals interesting differences from the previous tapered sets. The edge deformation is much less pronounced despite the high friction, suggesting that stress has been more evenly distributed throughout the top during the shear loading. In particular, the 5/1 - 15s sample shows that significant bending has occurred, but while maintaining the parallel contact with the counter-surface. By 20 s of etching, the top portion has been completely etched away, leaving residual wire structures in some parts that have collapsed as they are too thin to maintain structural integrity.

6.5.4 Comparing observed deformation behavior with finite element modelling

To provide further insight into the deformation observed in SEM after friction testing, finite element modeling for various pillar shapes was performed. For simplicity, a perfectly square cross-section with linear tapering is assumed, and relevant dimensions are estimated from the SEM images. As shown in Figure 6.23, the bottom of the pillar is fixed, and a force of 10 μN is applied to the top surface in the direction parallel to the sample in order to see the initial stage of bending during shear loading. The applied force, 10 μN, is an order of magnitude approximation from 1 N of force (range observed from the friction data) distributed to 250,000 pillars on a 1×1 cm^2 area. This comes out to be 4 μN/pillar, but the actual load on each pillar is likely much higher since not all pillars are in contact. This actual force would be dependent on the shape, but fixing the load at 10 μN allows comparison of stiffness across all shapes. The resulting deformation in the cross-section through the middle of pillar is shown in Figure 7 for four representative shapes. The deformation value indicates in microns the distance each point has moved from the original position. As the same load is applied to all pillars, larger deformation corresponds to relatively less stiff pillar geometry.

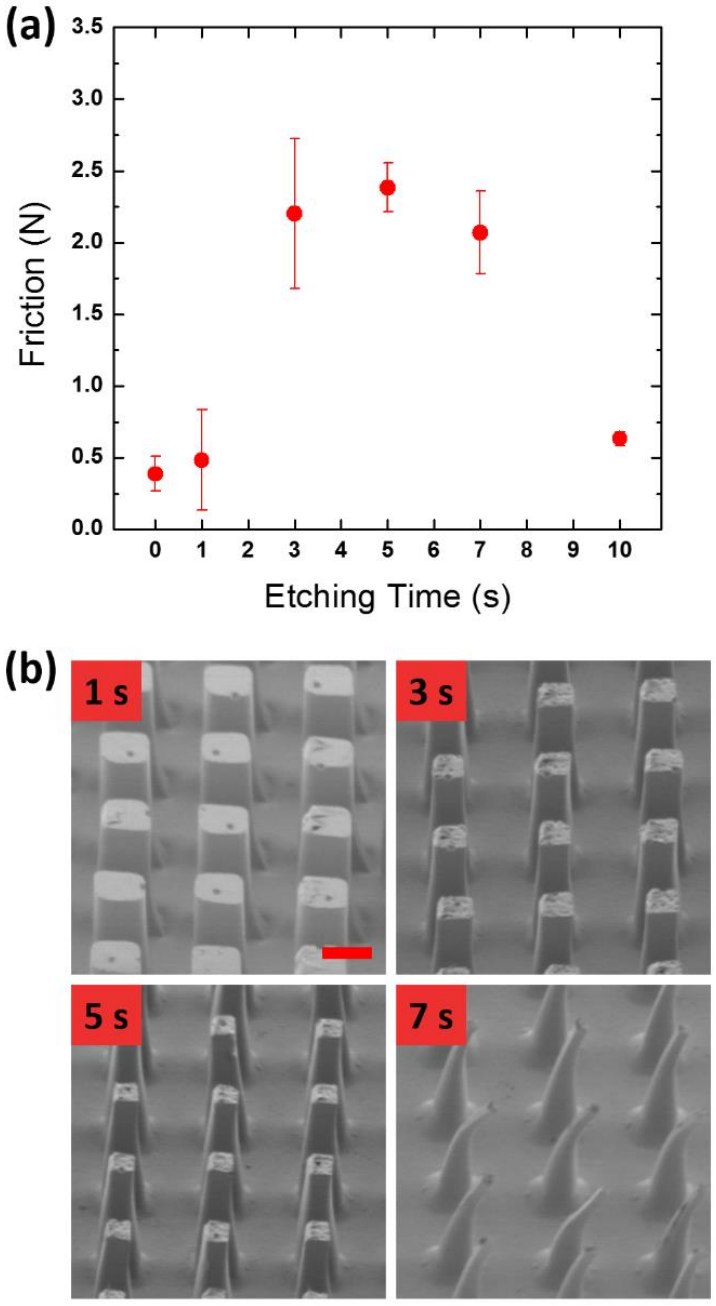

Figure 6.21: (a) Friction performance of 1 × 1 cm^2 patch of LDPE pillar array on smooth glass as template etching progresses in diluted HNA solution (HNA/H_2O = 5/0.7 mL for each 1 × 1 cm^2 template). (b) Representative SEM images of LDPE pillars after friction testing for samples molded from 1, 3, 5, and 7 s etched templates in 5/0.7 solution. Scale bar = 1 µm

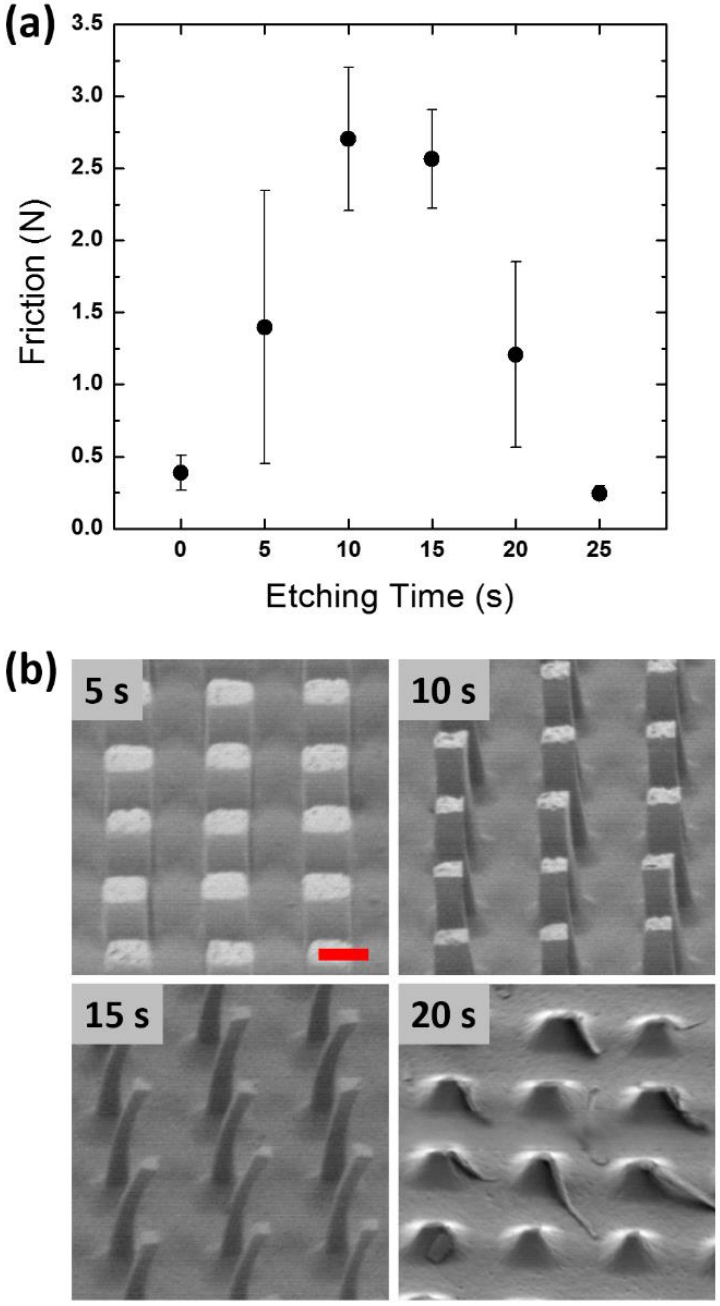

Figure 6.22: (a) Friction performance of 1 × 1 cm^2 patch of LDPE pillar array on smooth glass as template etching progresses in diluted HNA solution (HNA/H_2O = 5/1 mL for each 1 × 1 cm^2 template). (b) Representative SEM images of LDPE pillars after friction testing for samples molded from 5, 10, 15, and 20 s etched templates in 5/1 solution. Scale bar = 1 µm

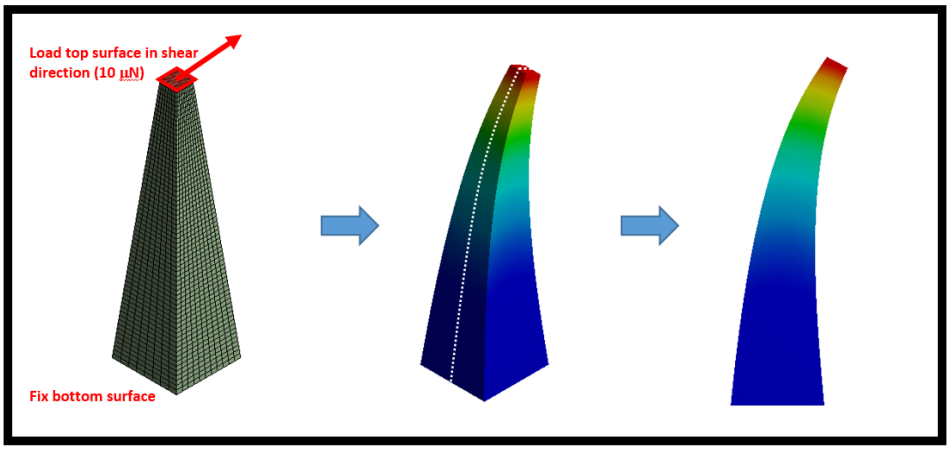

Figure 6.23: The finite element modeling was performed using ANSYS, and the representative images showing mesh elements, boundary conditions, resulting deformation, and the cross-section are shown. Only elastic deformation is considered, though in reality, the deformation is both elastic and plastic.

For the unetched shape (Figure 6.24a), a small deformation of ~0.58 µm is predicted at the tip. This is consistent with the SEM observation (Figure 6.19b – unetched), where no significant change in structure has occurred other than occasional dents in some corners suggesting contact. It is likely that the high stiffness has prevented any neighboring pillars to come into contact, given unavoidable height variation from fabrication. With high degree of tapering (Figure 6.24b), the finite element model suggests a large bending only at the top portion of the pillar, also consistent with experimentally observed behavior for pillars of similar shape (Figure 6.20b – 5 s). As most of the top area has been etched away, the pillar sides would have to come into contact to result in high friction. However, stiff portion towards the base limits the bending, and only allows the sides very close to the top to come into contact. As tapering is reduced, deformation is propagated further down the pillar, resulting in greater deformation throughout the entire pillar (Figure 6.24c). This compliance of the whole pillar can allow other neighboring pillars to come into contact and also make side contact possible, as confirmed by the SEM images that show all pillars in the vicinity have been deformed and some have been flattened on the sides (Figure 6.21b – 7 s). The reverse tapered shape (Figure 6.24d) is thinnest in the middle, and it is predicted that a large bending occurs there. However, this contact shape is different from that observed in the SEM images (Figure 6.22b – 15 s), where the top surface is still aligned parallel to the counter-surface. It seems the large top contact area has ensured enough adhesion to prevent rotational bending of the pillar. Nonetheless, the thin middle portion still enables a high degree of deformation and thus, allowing a large number of pillars to contact the counter surface, and the large top area ensures enough adhesion is provided by each pillar.

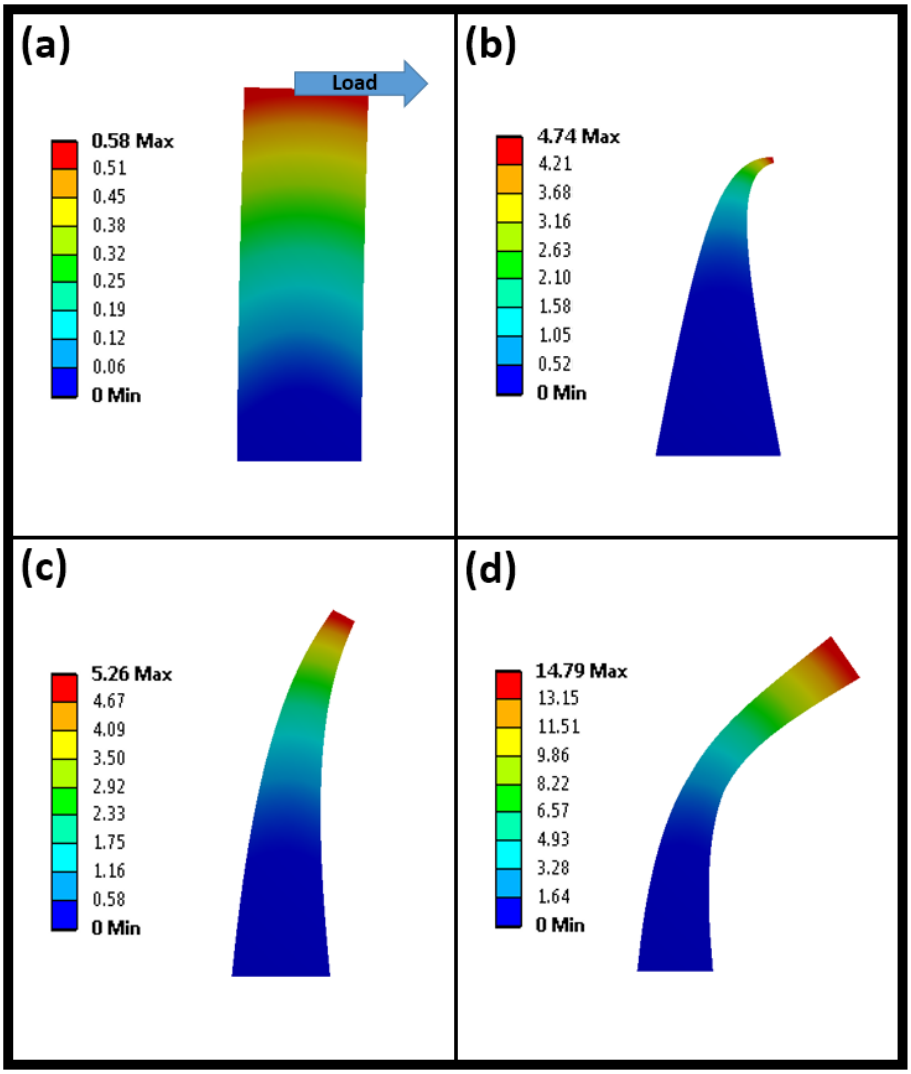

Figure 6.24: Bending behavior of various shaped pillars predicted by finite element modeling. Geometries are based on LDPE pillars molded from (a) unetched, (b) 5/0.5 – 5 s, (c) 5/0.7 – 7 s, and (d) 5/1 – 15 s etched templates. Total deformation on a cross-sectioned plane down the middle is displayed with the maximum value in µm noted.

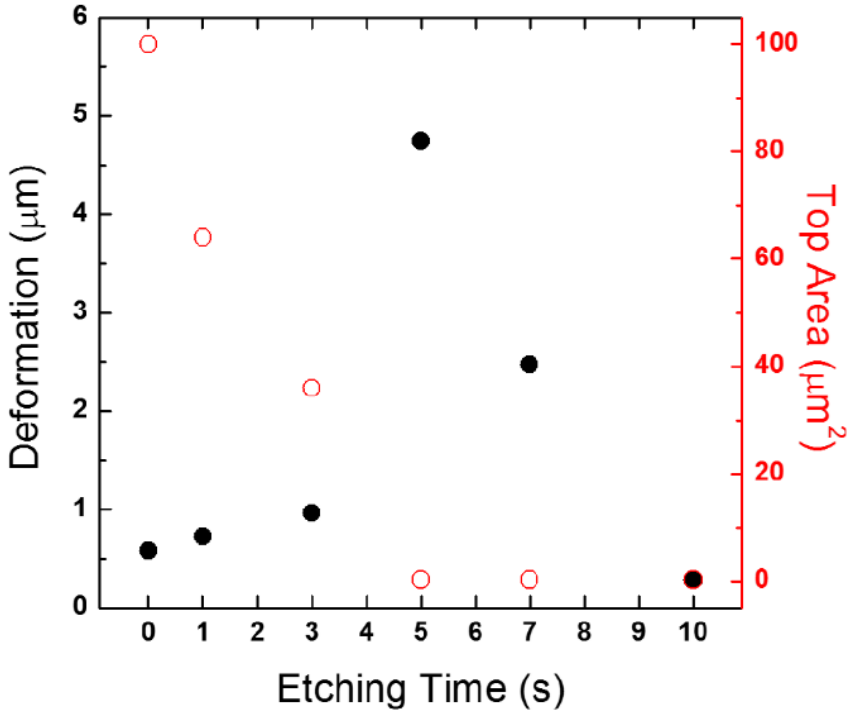

Figure 6.25: Total deformation (indicative of pillar stiffness) and top area change as etching progresses in 5/0.5 solution. A maximum is observed in compliance, but the top area continuously decreases to near 0.

To further examine the effect of pillar stiffness and contact area on the observed macroscale friction, the deformation predicted by ANSYS and top area of the pillar shapes estimated from the SEM images for the 5/0.5 etch condition have been plotted in Figure 6.25. As expected, dramatic decrease in stiffness (corresponding to higher deformation) is observed as pillars are thinned during etching, followed by an increase (corresponding to lower deformation) due to shortening once the top has been etched away. While it is reasonable that higher compliance enables higher number of pillars in contact, the peak value occurs at longer etching time than observed in the friction data (Fig. 6.20a). Accounting for the eroding top area, however, it would shift the peak to lower values, closer to the friction result. Despite its simplicity, the analysis based on pillar deformation and available top area qualitatively captures key elements affected by the tapering angle: the tapered pillars should be compliant enough to ensure high number of contacts, while sufficient contact area should be available on each pillar, since the macroscale friction performance depends on the combination of the two factors.

6.5.5 Summary

This section presented a simple method for tuning the tapering angle of a silicon pillar array by maskless chemical etching of lithographically defined vertical pillars. While etching thinned, and then eventually shortened the pillars, dilution of the etching solution by water decreased the tapering angle of the resulting pillars. By using them as templates for molding, thermoplastic pillar array with a variety of shapes could be fabricated. Frictional testing showed that the adhesive behavior of the film was very sensitive to the tapering angle. In general, friction initially increased with increasing etching time of template as the pillars thinned to be more compliant, but decreased as the top started to etch away and pillars were shortened. As tapering angle decreased, the peak friction value could be significantly increased. SEM observation of deformed pillars after testing revealed that the contact behavior was dependent on the pillar shape. While thicker pillars molded from templates with short etching time showed little deformation due to high stiffness, highly tapered pillars showed contact deformation limited to the top portion of the pillar. As tapering angle decreased, deformation was more pronounced throughout the entire pillar. Finite element modelling confirmed that observed deformation is consistent with what was expected from mechanical analysis and provided useful insights on the contributing factors of pillar compliance and contact area. As template etching proceeds, there is an optimum in compliance, but contact area continually decreases, and the resulting macroscale friction is a combined effect of the two. Decreasing tapering effectively leads to preserving the contact area available at the top as pillars are thinned for higher compliance.

Chapter 7

Conclusion and Future Works

7.1 Summary of dissertation

Following the introduction to gecko adhesion, a brief survey the literature on gecko-inspired adhesives, and explanation of the challenges currently faced by such adhesives, majority of this work was dedicated to addressing some of the challenges, specifically for gaining a better understanding of friction behavior of fibrillar interface. It was demonstrated that SiNWs etched by metal-assisted chemical etching yielded well-defined templates suitable for replicating into thermoplastic fibrillar array with adhesive characteristics. Some fundamental fiber geometric parameters were optimized for high friction on smooth glass, followed by friction testing on rough and low surface energy counter-substrates that served as model substrates simulating surfaces in potential applications. These studies provided insights on how the mechanical behavior of individual fibers influence the adhesive behavior of the array as a whole, which were supported by simple mechanical analyses. It is hoped that the knowledge will aid in the rational design of future gecko synthetic adhesives, both in obtaining high adhesion and friction and for versatile performance on a wide range of surfaces outside the controlled laboratory environment.

Later chapters examined various ways to fabricate more complex designs for GSAs. Particular attention was paid to how metal-assisted chemical etching could be controlled to produce different SiNW morphologies, not only useful as molding templates for GSAs, but also for applications in various SiNW devices. This was followed by fabrication schemes for hierarchical structure, composite adhesive design, and tapered micropillars with precise control over the tapering angle. Although some of the presented fiber designs resulted in only modest friction, they served as proof-of-concept for new fabrication approaches to aid and inspire improved methods in the future.

7.2 Future works

Due to limitations of single level nanofibers, further optimization of hierarchical structures remains an important issue, in particular with respect to various geometric parameters. The effects

of basic parameters, such as width, length, and spacing of both levels of hierarchical structures should be explored. In addition, approaches to distribute the load more evenly within the micro-structure base is critical. To this end, various shapes of micro-pillar base, for example with different tapering angles, could be studied to see whether the stress concentration at the edge can be relieve for the hierarchical structure. Macroscale friction testing and post-test observation of deformation should provide useful information for maximizing performance and determining the modes of failure or mechanical limitations of the adhesive.

Continued study on testing of GSAs on non-ideal surface is also critical for fabricating adhesive with high strength on a variety of surfaces. While this work gave some insights on the effect of roughness and surface energy on GSA performance based on simplified model substrates, surfaces in real applications present much more complex challenges, with any possible combinations of various levels of roughness, a wide range of surface energies, and different levels of contamination. Further studying these factors, in particular with respect to combined effect of roughness and surface energy, should provide useful insights on fibrillar interfacial behavior and rational design of adhesives. Methods used here for creating model rough surfaces (silica evaporation over colloidal array) and self-assembled monolayer coating can easily be combined to produce more complex model substrates for such study.

Finally, the shortcomings of thermoplastics should be improved upon. While exhibiting high adhesive friction, thermoplastic adhesives tend to have low normal adhesive strength, rendering them a poor substitute for conventional pressure sensitive tapes in a typical use. Improvement in normal adhesive strength could be made by various approaches, for example based on manipulation of the tip shape for higher contact area, optimization of fiber number density, and research into failure mechanisms that limit the normal adhesion strength. Durability of thermoplastics, in particular LDPE used throughout this work, also remains an important problem. While the plastic deformation is a useful for examining contact behavior of fibers, it ultimately limits the life cycle of the adhesive. To this end, plastics closer in stiffness to natural gecko could be studied in more detail. Although they require fabrication of higher aspect ratio structure due to higher stiffness, higher durability and similarity in the material stiffness could aid in design of adhesive that more closely mimic the mechanism of natural gecko adhesion.

Bibliography

[1] K. Autumn, Y. A. Liang, S. T. Hsieh, W. Zesch, W. P. Chan, T. W. Kenny, R. Fearing, R. J. Full. Adhesive force of a single gecko foot-hair. *Nature* **2000**, *405*, 681-685.

[2] K. Autumn, M. Sitti, Y. A. Liang, A. M. Peattie, W. R. Hansen, S. Sponberg, T. W. Kenny, R. Fearing, J. N. Israelachvili, R. J. Full. Evidences for van der Waals adhesion in gecko setae. *Proc. Natl. Acad. Sci. U.S.A.* **2002**, *99*, 12252-12256.

[3] K. Autumn, C. Majidi, R. E. Groff, A. Dittmore, R. Fearing. Effective elastic modulus of isolated gecko setal arrays. *J. Exp. Biol.* **2006**, *209*, 3558-3568.

[4] E. Arzt, S. Gorb, R. Spolenak. From micro to nano contacts in biological attachment devices. *Proc. Natl. Acad. Sci. U.S.A.* **2003**, *100*, 10603-10606.

[5] Y. Tian, N. Pesika, H. Zeng, K. Rosenberg, B. Zhao, P. McGuiggan, K. Autumn, J. Israelachvili. Adhesion and friction in gecko toe attachment and detachment. *Proc. Natl. Acad. Sci. U.S.A.* **2006**, *103*, 19320-19325.

[6] K. Autumn, A. Dittmore, D. Santos, M. Spenko, M. Cutkosky. Frictional adhesion: a new angle on gecko attachment. *J. Exp. Biol.* **2006**, *209*, 3569-3579.

[7] L. F. Boesel, C. Greiner, E. Arzt, A. del Campo. Gecko-inspired surfaces: a path to strong and reversible dry adhesives. *Adv. Mater.* **2010**, *22*, 2125-2137.

[8] D. Sameoto, C. Menon. Recent advances in the fabrication and adhesion testing of biomimetic dry adhesives. *Smart Mater. Struct.* **2010**, *19*, 103001.

[9] A. del Campo, E. Arzt. Design parameters and current fabrication approaches for developing bioinspired dry adhesives. *Macromol. Biosci.* **2007**, *7*, 118-127.

[10] H. E. Jeong, K. Y. Suh. Nanohairs and nanotubes: efficient structural elements for gecko-inspired artifical dry adhesives. *Nano Today* **2009**, *4*, 335-346.

[11] M. K. Kwak, C. Pang, H. Jeong, H. Kim, H. Yoon, H. Jung, K. Suh. Towards the next level of bioinspired dry adhesives: new designs and applications. *Adv. Funct. Mater.* **2011**, *21*, 3606-3616.

[12] S. Hu, Z. Xia. Rational design and nanofabrication of gecko-inspired fibrillar adhesives. *Small* **2012**, *8*, 2464-2468.

[13] A. Jagoda, C. Hui. Adhesion, friction, and compliance of bio-mimetic and bio-inspired structured interfaces. *Mater. Sci. Eng., R.* **2011**, *72*, 253-292.

[14] L. Juan, Y. Qinglin, X. Jingjing, L. Kesong, G. Lin, J. Lei. Adhesive materials inspired by gecko and mussel. *Prog. Chem.* **2012**, *24*, 1946-1954.

[15] A. J. Kinloch. *Adhesion and Adhesives: Science and Technology*, 1987 ed. Chapman & Hall: London, 1987.

[16] B. N. J. Persson. On the mechanism of adhesion in biological systems. *J. Chem. Phys.* **2003**, *118*, 7614-7621.

[17] K. Autumn. Gecko adhesion: structure, function, and applications. *MRS bull.* **2007**, *32*, 473-478.

[18] A. Asbeck, S. Dastoor, A. Parness, L. Fullerton, N. Esparza, D. Soto, B. Heyneman, M. Cutkosky. Climbing rough vertical surfaces with hierarchical directional adhesion. *IEEE Int. Conf. Robot.*, Kobe, Japan, May 12-17, 2009, 2675-2680.

[19] D. Santos, S. Kim, M. Spenko, A. Parness, M. Cutkosky. Directional adhesive structures for controlled climbing on smooth vertical surfaces. *IEEE ICRA*, Roma, Italy, April 10-14, 2007, 1262-1267.

[20] B. Aksak, M. P. Murphy, M. Sitti. Gecko inspired micro-fibrillar adhesives for wall climbing robots on micro/nanoscale rough surfaces. *IEEE ICRA*, Pasadena, CA, May 19-23, 2008, 3058-3063.

[21] C. Menon, M. Murphy, M. Sitti. Gecko inspired surface climbing robots. *IEEE ROBIO*, Shenyang, China, August 22-26, 2004, 431-436.

[22] Y. Li, D. Sameoto, C. Menon. Properties validation of an anisotropic dry adhesion designed for legged clmibing robots. *IEEE ROBIO*, Guilin, China, December 19-23, 2009, 1906-1911.

[23] E. W. Hawkes, J. Ulmen, N. Esparza, M. R. Cutkosky. Scaling walls: applying dry adhesives to the real world. *IEEE IROS*, San Francisco, CA, September 25-30, 2011, 5100-5106.

[24] S. Kim, M. Spenko, S. Trujillo, B. Heyneman, D. Santos, M. R. Cutkosky. Smooth vertical surface climbing with directional adhesion. *IEEE. Trans. Robot* **2008**, 24, 65-74.

[25] M. Sitti, R. S. Fearing. Synthetic gecko foot-hair micro/nano-structures for future wall-climbing robots. *IEEE ICRA*, Taipei, Taiwan, September 14-19, 2003, 1164-1170.

[26] M. P. Murphy, C. Kute, Y. Mengüç, M. Sitti. Waalbot II: adhesion recovery and improved performance of a clmibing robot using fibrillar adhesives. *Int. J. Robot. Res.* **2010**, *30*, 118-133.

[27] A. Sintov, T. Avramovich, A. Shapiro. Design and motion planning of an autonomous clmibing robot with claws. *Robot. Auton. Syst.* **2011**, *59*, 1008-1019.

[28] M. F. Silva, R. S. Barbosa, A. L. C. Oliveira. "Climbing robot for ferromagnetic surfaces with dynamic adjustment of the adhesion system. *J. Robotics* **2012**, 906545.

[29] H. E. Jeong, J. Lee, H. N. Kim, S. H. Moon, K. Y. Suh. A nontransferring dry adhesive with hierarchical polymer nanohairs *Proc. Natl. Acad. Sci. U.S.A.* **2009**, *106*, 5639-5644.

[30] A. G. Gillies, J. Kwak, R. S. Fearing. Controllable particle adhesion with a magnetically actuated synthetic gecko adhesive. *Adv. Funct. Mater.* **2013**, *23*, 3256-3261.

[31] A. G. Gillies, R. S. Fearing. Shear adhesion strength of thermoplastic gecko-inspired synthetic adhesive exceeds material limits. *Langmuir* **2011**, *27*, 11278-11281.

[32] L. Qu, L. Dai, M. Stone, Z. Xia, Z. L. Wang. Carbon nanotube arrays with strong shear binding-on and easy normal lifting-off. *Science*, **2008**, *322*, 238-242.

[33] A. K. Geim, S. V. Dubonos, I. V. Grigorieva, K. S. Novoselov, A. A. Zhukov, S. Y. Shapoval. Microfabricated adhesive mimcking gecko foot-hair. *Nat. Mater.* **2003**, *2*, 461-463.

[34] B. Aksak, M. P. Murphy, M. Sitti. Adhesion of biologically inspired vertical and angled polymer microfiber arrays. *Langmuir* **2007**, *23*, 3322-3332.

[35] T. Kim, H. E. Jeong, K. Y. Suh, H. H. Lee. Stooped nanohairs-geometry-controllable, unidirectional, reversible, and robust gecko-like dry adhesive. *Adv. Mater.* **2009**, *21*, 2276-2281.

[36] H. Yoon, H. E. Jeong, T. Kim, T. J. Kang, D. Tahk, K. Char, K. Y. Suh. Adhesion hysteresis of Janus nanopillars fabricated by nanomolding and oblique metal deposition. *Nano Today* **2009**, *4*, 385-392.

[37] M. Moon, T. Cha, K. Lee, A. Vaziri, H. Kim. Tilted Janus polymer pillars. *Soft Matter* **2010**, *6*, 3924-3929. 2010.

[38] J. Lee, R. S. Fearing. K. Komvopoulos. Directional adhesion of gecko-inspired angled microfiber arrays. *Appl. Phys. Lett.* **2008**, *93*, 191910.

[39] D. Santos, M. Spenko, A. Parness, S. Kim, M. Cutkosky. Directional adhesion for climbing: theoretical and practical considerations. *J. Adhes. Sci. Technol.* **2007**, *21*, 1317-1341.

[40] M. P. Murphy, B. Aksak, M. Sitti. Adhesion and anisotropic friction enhancements of angled heterogeneous micro-fiber arrays with spherical and spatula tips. *J. Adhes. Sci. Technol.* **2007**, *21*, 1281-1296.

[41] H. E. Jeong, J. Lee, M. K. Kwak, S. H. Moon, K. Y. Suh. Effect of leaning angle of gecko-inspired slanted polymer nanohairs on dry adhesion. *Appl. Phys. Lett.* **2010**, *96*, 043704.

[42] G. Huber, S. N. Gorb, N. Hosoda, R. Spolenak, E. Arzt. Influence of surface roughness on gecko adhesion. *Acta Biomater.* **2007**, *3*, 607-610.

[43] A. del Campo, C. Greiner, I Á lvaerez , E. Arzt. Patterned surfaces with pillars with controlled 3D tip geometry mimicking bioattachment devices. *Adv. Mater.* **2007**, *19*, 1973-1977.

[44] A. del Campo, C. Greiner, E. Arzt. Contact shape controls adhesion of bioinspired fibrillar surfaces. *Langmuir* **2007**, *23*, 10235-10243.

[45] S. Kim, M. Sitti. Biologically inspired polymer microfibers with spatulate tips as repeatable fibrillar adhesives. *Appl. Phys. Lett.* **2006**, *89*, 261911.

[46] M. P. Murphy, B. Aksak, M. Sitti. Gecko-inspired directional and controllable adhesion. *Small* **2009**, *5*, 170-175.

[47] J. Davies, S. Haq, T. Hawke, J. P. Sargent. A practical approach to the developmentof a synthetic gecko tape. *Int. J. Adhes. Adhes.* **2009**, *29*, 380-390.

[48] D. Wang, A. Zhao, R. Jiang, D. Li, M. Zhang, Z. Gan, W. Tao, H. Guo, T. Mei. Surface properties of bionic micro-pillar arrays with various shapes of tips. *Appl. Surf. Sci.* **2012**, *259*, 93-98.

[49] M. P. Murphy, S. Kim, M. Sitti. Enhanced adhesion by gecko-inspired hierarchical fibrillar adhesives. *ACS Appl. Mater. Interfaces* **2009**, *1*, 849-855.

[50] J. Lee, B. Bush, R. Maboudian, R. S. Fearing. Gecko-inspired combined lamellar and nanofibrillar array for adhesion on nonplanar surface. *Langmuir* **2009**, *25*, 12449-12453.

[51] H. Lee, B. Bhushan. Fabrication and characterization of hierarchical nanostructured smart adhesion surfaces. *J. Colloid Interface Sci.* **2012**, *372*, 231-238.

[52] H. Izadi, B. Zhao, Y. Han, N. McManus, A. Penlidis. "Teflon hierarchical nanopillars with dry and wet adhesive properties. *J. Polym. Sci., Part B: Polym. Phys.* **2012**, *50*, 846-851.

[53] C. Greiner, E. Arzt, A. del Campo. Hierarchical gecko-like adhesives. *Adv. Mater.* **2009**, *21*, 479-482.

[54] E. Huovinen, J. Hirvi, M. Suvanto, T. A. Pakkanen. Micro-micro hierarchy replacing micro-nano hierarchy: precisely controlled way to produce wear-resistant superhydrophobic polymer surfaces. *Langmuir* **2012**, *28*, 14747-14755.

[55] M. Röhrig, M. Thiel, M. Worgull, H. Hölscher. 3D direct laser writing of nano- and microstructured hierarchical gecko-mimicking surfaces. *Small* **2012**, *8*, 3009-3015.

[56] H. Izadi, M. Golmakani, A. Penlidis. Enhanced adhesion and friction by electrostatic interactions of double-level Teflon nanopillars. *Soft Matter* **2013**, *9*, 1985-1996.

[57] D. Y. Lee, D. H. Lee, S. G. Lee, K. Cho. Hierarchical gecko-inspired nanohairs with a high aspect ratio induced by nanoyielding. *Soft Matter* **2012**, *8*, 4905-4910.

[58] H. Zhang, L. Wu, S. Jia, D. Guo, Z. Dai. Fabrication and adhesion of hierarchical micro-seta. *Chin. Sci. Bull.* **2012**, *57*, 1343-1349.

[59] A. Y. Y. Ho, L. P. Yeo, Y. C. Lam, I. Rodríguez. Fabrication and analysis of gecko-inspired hierarchical polymer nanosetae. *ACS Nano* **2011**, *5*, 1897-1906.

[60] W. R. Hansen, K. Autumn. Evidence for self-cleaning in gecko setae. *Proc. Natl. Acad. Sci. U.S.A.* **2005**, *102*, 385-389.

[61] J. Lee, R. S. Fearing. Contact self-cleaning of synthetic gecko adhesive from polymer microfibers. *Langmuir* **2008**, *24*, 10587-10591.

[62] A. G. Gillies, J. Puthoff, M. J. Cohen, K. Autumn, R. S. Fearing. Dry self-cleaning properties of hard and soft fibrillar structures. *ACS Appl. Mater. Interfaces* **2013**, *5*, 6081-6088.

[63] J. Lee, R. S. Fearing. Wet self-cleaning of superhydrophobic microfiber adhesives formed from high density polyethylene. *Langmuir* **2012**, *28*, 15372-15377.

[64] S. Vajpayee, A. Jagota, C. Hui. Adhesion of a fibrillar interface on wet and rough surfaces. *J. Adhes.* **2010**, *86*, 39-61.

[65] J. N. Israelachvilli. *Intermolecular and Surface Forces*, 2nd ed., Academic Press: Oxford, UK, 1991.

[66] M. de Meijer, S. Haemers, W. Cobben, H. Militz. Surface energy determinations of wood: comparison of methods and wood species. *Langmuir* **2000**, *16*, 9352-9359.

[67] D. K. Owens, R. C. Wendt. Estimation of the surface free energy of polymers. *J. Appl. Polym. Sci.* **1969**, *13*, 1741-1747.

[68] M. Yu, T. Kowalewski, R. S. Ruoff. Structural analysis of collapsed, and twisted and collapsed, multiwalled carbon nanotubes by atomic force microscopy. *Phys. Rev. Lett.* **2001**, *86*, 87-90.

[69] D. H. Lee, Y. Kim, R. S. Fearing, R. Maboudian. Effect of fiber geometry on macroscale friction of ordered low-density polyethylene nanofiber arrays. *Langmuir* **2011**, *27*, 11008-11016.

[70] Y. Kim, F. Limanto, D. H. Lee, R. S. Fearing, R. Maboudian. Role of counter-substrate surface energy in macroscale friction of nanofiber arrays. *Langmuir* **2012**, *28*, 2922-2927.

[71] Y. Kim, R. K. Claus, F. Limanto, R. S. Fearing, R. Maboudian. Friction characteristics of polymeric nanofiber arrays against substrates with tailored geometry. *Langmuir* **2013**, *29*, 8395-8401.

[72] N. Vogel, C. K. Weiss, K. Landfester. From soft to hard: the generation of functional and complex colloidal monolayers for nanolithography. *Soft Matter* **2012**, *8*, 4044-4061.

[73] Z. Huang, N. Geyer, P. Werner, J. de Boor, U. Gösele. Metal-assisted chemical etching of silicon - a review. *Adv. Mater.* **2011**, *23*, 285-308.

[74] S. Begej. Planar and Finger-Shaped Optical Tactile Sensors for Robotic Applications. *IEEE J. Rob. Autom.* **1988**, *4*, 472-484.

[75] C. Greiner, A. del Campo, E. Arzt. Adhesion of bioinspired micropatterned surfaces - effects of pillar radius, aspect ratio, and preload. *Langmuir* **2007**, *23*, 3495-3502.

[76] Z. Burton, B. Bhushan. Hydrophobicity, adhesion, and friction properties of nanopatterned polymers and scale dependence for micro- and nanoelectromechanical systems. *Nano Lett.* **2005**, *5*, 1607-1613.

[77] N. J. Glassmaker, A. Jagota, C. Hui. Adhesion enhancement in a biomimetic fibrillar interface. *Acta Biomater.* **2005**, *1*, 367-375.

[78] Y. Zhao, T. Tong, L. Delzeit, A. Kashani, M. Meyyappan, A. Majumdar. Interfacial energy and strength of multiwalled-carbon-nanotube-based dry adhesive. *J. Vac. Sci. Technol. B* **2006**, *24*, 331-335.

[79] R. Spolenak, S. Gorb, E. Arzt. Adhesion design maps for bio-inspired attachment systems. *Acta Biomater.* **2005**, *1*, 5-13.

[80] K. L. Johnson, K. Kendall, A. D. Roberts. Surface energy and the contact of elastic solids *Proc. R. Soc. London, Ser. A* **1971**, *324*, 301−313.

[81] M. Sitti, R. S. Fearing. Synthetic gecko foot-hair micro-nano-structures as dry adhesives *J. Adhes. Sci. Technol.* **2003**, *17*, 1055-1073.

[82] B. Schubert, C. Majidi, R. E. Groff, S. Baek, B. Bush, R. Maboudian, R. S. Fearing. Towards friction and adhesion from high modulus microfiber arrays. *J. Adhes. Sci. Technol.* **2007**, *21*, 1297-1315.

[83] Matweb Material Property Data. Overview of materials for Low Density Polyethylene (LDPE), Molded. Accessed February 12, 2014.

[84] J. Lee, C. Majidi, B. Schubert, R. S. Fearing. Sliding-induced adhesion of stiff polymer microfibre arrays. I. macroscale behaviour. *J. R. Soc. Interface* **2008**, *5*, 835-844.

[85] C. Majidi, R. E. Groff, Y. Maeno, B. Schubert, S. Baek, B. Bush, R. Maboudian, N. Gravish, M. Wilkinson, K. Autumn, R. S. Fearing. High friction from a stiff polymer using microfiber arrays. *Phys. Rev. Lett.* **2006**, *97*, 076103.

[86] D. H. Gracias, G. A. Somorjai. Continuum force microscopy study of the elastic modulus, hardness and friction of polyethylene and polypropylene surfaces. *Macromolecules* **1998**, *31*, 1269-1276.

[87] J. L. Willett. Mechanical Properties of LDPE Granular Starch Composite. *J. Appl. Polym. Sci.* **1994**, *54*, 1685-1695.

[88] C. S. Majidi, R. E. Groff, R. S. Fearing. Attachment of fiber array adhesive through side contact. *J. Appl. Phys.* **2005**, *98*, 103521.

[89] T. Beléndez, C. Neipp, A. Beléndez. "Large and small deflections of a cantilever beam. *Eur. J. Phys.* **2002**, *23*, 371-379.

[90] K. Lee. Large deflections of cantilever beams of non-linear elastic material under a combined loading. *Int. J. Nonlinear. Mech.* **2002**, *37*, 439-443.

[91] G. Huber, H. Mantz, R. Spolenak, K. Mecke, K. Jacobs, S. N. Gorb, E. Arzt. Evidence for capillarity contributions to gecko adhesion from single spatula nanomechanical measurements. *Proc. Natl. Acad. Sci. U.S.A.* **2005**, *102*, 16293-16296.

[92] J. B. Puthoff, M. S. Prowse, M. Wilkinson, K. Autumn. Changes in materials properties explain the effects of humidity on gecko adhesion. *J. Exp. Bio.* **2010**, *213*, 3699-3704.

[93] L. Ge, S. Sethi, L. Ci, P. M. Ajayan, A. Dhinojwala. Carbon nanotube-based synthetic gecko tapes. *Proc. Natl. Acad. Sci. U.S.A.* **2007**, *104*, 10792-10795.

[94] D. Janssen, R. D. Palma, S. Verlaak, P. Heremans, W. Dehaen. Static solvent contact angle measurements, surface free energy and wettability determination of various self-assembled monolayers on silicon dioxide. *Thin Solid Films* **2006**, *515*, 1433-1438.

[95] A. Heise, M. Stamm, M. Rauscher, H. Duschner, H. Menzel. Mixed silane self assembled monolayers and their in situ modification. *Thin Solid Films* **1998**, *327-329*, 199-203.

[96] H. I. Kim, T. Koini, T. R. Lee, S. S. Perry. Systematic studies of the frictional properties of fluorinated monolayers with atomic force microscopy: comparison of CF_3^- and CH_3^- terminated films. *Langmuir* **1997**, *13*, 7192-7196.

[97] W. Sun, P. Neuzil, T. S. Kustandi, S. Oh, V. D. Samper. The nature of the gecko lizard adhesive force. *Biophys. J.* **2005**, *89*, L14-L17.

[98] J. N. Israelachvili, Y. Chen, H. Yoshizawa. Relationship between adhesion and friction forces. *J. Adhes. Sci. Technol.* **1994**, *8*, 1231-1249.

[99] N. M. Pugno, E. Lepore. Observation of optimal gecko's adhesion on nanorough surfaces. *Biosystems* **2008**, *94*, 218-222.

[100] N. Cañas, M. Kamperman, B. Völker, E. Kroner, R. M. McMeeking, E. Arzt. Effect of nano- and micro-roughness on adhesion of bioinspired micropatterned surfaces. *Acta Biomater.* **2012**, *8*, 282-288.

[101] J. Yu, S. Chary, S. Das, J. Tamelier, K. L. Turner, J. N. Israelachvili. Friction and adhesion of gecko-inspired PDMS flaps on rough surfaces. *Langmuir* **2012**, *28*, 11527-11534.

[102] Y. Cui, C. M. Lieber. Functional nanoscale electronic devices assembled using silicon nanowire building blocks. *Science* **2001**, *291*, 851-853.

[103] L. J. Chen. Silicon nanowires - the key building block for future electronic devices. *J. Mater. Chem.* **2007**, *17*, 4639-4643.

[104] R. Agarwal, C. M. Lieber. Semiconductor nanowires: optics and optoelectronics. *Appl. Phys. A* **2006**, *85*, 209-215.

[105] A. I. Hochbaum, R. Chen, R. D. Delgado, W. Liang, E. C. Garnett, M. Najarian, A. Majumdar, P. Yang. Enhanced thermoelectric performance of rough silicon nanowires. *Nature* **2008**, *451*, 163-168.

[106] Y. Cui, Q. Wei, H. Park, C. M. Lieber. Nanowire nanosensors for highly sensitive and selective detection of biological and chemical species. *Science* **2001**, *293*, 1289-1292.

[107] M. D. Kelzenberg, S. W. Boettcher, J. A. Petykiewicz, D. B Turner-Evans, M. C. Putnam, E. L. Warren, J. M. Spurgeon, R. M. Briggs, N. S. Lewis, H. A. Atwater. Enhanced absorption and carrier collection in Si wire arrays for photovoltaic applications. *Nat. Mater.* **2010**, *9*, 239-244.

[108] C. Hsin, W. Mai, Y. Gu, Y. Gao, C. Huang, Y. Liu, L. Chen, Z. Wang. Elastic properties and buckling of silicon nanowires. *Adv. Mater.* **2008**, *20*, 3919-3923.

[109] S. Hoffmann, I. Utke, B. Moser, J. Michler, S. H. Christiansen, V. Schmidt, S. Senz, P. Werner, U. Gösele, C. Ballif. Measurement of the bending strength of vapor-liquid-solid grown silicon nanowires. *Nano Lett.* **2006**, *6*, 622-625.

[110] M. K. Dawood, T. H. Liew, P. Lianto, M. H. Hong, S. Tripathy, J. T. L. Thong, W. K. Choi. Interference lithographically defined and catalytically etched, large-area silicon nanocones from nanowires. *Nanotechnology* **2010**, *21*, 205305.

[111] C. Chartier, S. Bastide, C. Lévy-Clément. Metal-assisted chemical etching of silicon in HF-H_2O_2. *Electrochim. Acta.* **2008**, *53*, 5509-5516.

[112] C. Lee, K. Tsujino, Y. Kanda, S. Ikeda, M. Matsumura. Pore formation in silicon by wet etching using micrometre-sized metal particles as catalysts. *J. Mater. Chem.* **2008**, *18*, 1015-1020.

[113] Z. Huang, T. Shimizu, S. Senz, Z. Zhang, X. Zhang, W. Lee, N. Geyer, U. Gösele Ordered arrays of vertically aligned [110] silicon nanowires by suppressing the crystallographically preferred 100 etching directions. *Nano Lett.* **2009**, *9*, 2519-2525.

[114] M. Zhang, K. Peng, X. Fan, J. Jie, R. Zhang, S. Lee, N. Wong. Preparation of large-area uniform silicon nanowires through metal-assisted chemical etching. *J. Phys. Chem. C* **2008**, *112*, 4444-4450.

[115] N. Megouda, T. Hadjersi, G. Piret, R. Boukherroub, O. Elkechai. Au-assisted electroless etching of silicon in aqueous HF-H_2O_2 solution. *Appl. Surf. Sci.* **2009**, *255*, 6210-6216.

[116] W. Chern, K. Hsu, I. S. Chun, B. P. de Azeredo, N. Ahmed, K. Kim, J. Zuo, N. Fang, P. Ferreira, X. Li. Nonlithographic patterning and metal-assisted chemical etching for manufacturing of tunable light-emitting silicon nanowire arrays. *Nano Lett.* **2010**, *10*, 1582-1588.

[117] Y. Qu, L. Liao, Y. Li, H. Zhang, Y. Huang, X. Duan. Electrically conductive and optically active porous silicon nanowires. *Nano Lett.* **2009**, *9*, 4539-4543.

[118] C. C. Büttner, A. Langner, M. Geuss, F. Müller, P. Werner, U. Gösele. Formation of straight 10 nm diameter silicon nanopores in gold decorated silicon. *ACS Nano* **2009**, *3*, 3122-3126.

[119] X. Li, P. W. Bohn. Metal-assisted chemical etching in HF-H_2O_2 produces porous silicon. *Appl. Phys. Lett.* **2000**, *77*, 2572-2574.

[120] I. S. Chun, E. K. Chow, X. Li. Nanoscale three dimensional pattern formation in light emitting porous silicon. *Appl. Phys. Lett.* **2008**, *92*, 191113.

[121] O. J. Hildreth, W. Lin, C. P. Wong. Effect of catalyst shape and etchant composition on etching direction in metal-assisted chemical etching of silicon to fabricate 3D nanostructures. *ACS Nano* **2009**, *3*, 4033-4042.

[122] N. Sato, K. Sakaguchi, K. Yamagata, Y. Fujiyama, T. Yonehara. Epitaxial growth on porous Si for a new bond and etchback silicon-on-insulator. *J. Electrochem. Soc.* **1995**, *142*, 3116-3122.

[123] A. Pascual, J. F. Fernández, C. R. Sánchez. Structural characteristics of p-type porous silicon and their relation to the nucleation and growth of pores. *J. Porous Mater.* **2002**, *9*, 57-66.

[124] C. Chiappini, X. Liu, J. R. Fakhoury, M. Ferrari. Biodegradable porous silicon barcode nanowires with defined geometry. *Adv. Funct. Mater.* **2010**, *20*, 2231-2239.

[125] W. Y. Chen, J. T. Huang, Y. C. Cheng, C. C. Chien, C. W. Tsao. Fabrication of nanostructured silicon by metal-assisted etching and its effects on matrix-free laser desorptionionization mass spectrometry. *Anal. Chim. Acta.* **2011**, *687*, 97-104.

[126] H. Fang, X. Li, S. Song, Y. Xu, J. Zhu. Fabrication of slantingly-aligned silicon nanowire arrays for solar cell applications. *Nanotechnology* **2008**, *19*, 255703.

[127] J. Kim, H. Han, Y. H. Kim, S. Choi, J. Kim, W. Lee. Au-Ag Bilayered Metal Mesh as a Si Etching Catalyst for Controlled Fabrication of Si Nanowires. *ACS Nano* **2011**, *4*, 3222-3229.

[128] Z. Huang, T. Shimizu, S. Senz, Z. Zhang, N. Geyer, U. Gösele. Oxidation rate effect on the direction of metal-assisted chemical and electrochemical etching of silicon. *J. Phys. Chem. C* **2010**, *114*, 10683-10690.

[129] K. Peng, M. Zhang, A. Lu, N. Wong, R. Zhang, S. Lee. Ordered silicon nanowire arrays via nanosphere lithography and metal-induced etching. *Appl. Phys. Lett.* **2007**, *90*, 163123.

[130] C. Chen, C. Wu, C. Chou, T. Yen. Morphological control of single-crystalline silicon nanowire arrays near room temperature. *Adv. Mater.* **2008**, *20*, 3811-3815.

[131] K. Peng, A. Lu, R. Zhang, S. Lee. Motility of metal nanoparticles in silicon and induced anisotropic. *Adv. Funct. Mater.* **2008**, *18*, 3026-3035.

[132] M. Christophersen, J. Carstensen, S. Rönnebeck, C. Jäger, W. Jäger, H. Föll. Crystal orientation dependence and anisotropic properties of macropore formation of p- and n-type silicon. *J. Electrochem. Soc.* **2001**, *148*, E267-E375.

[133] V. Lehmann. The physics of macropore formation in low doped n-type silicon. J. *Electrochem. Soc.* **1993**, *140*, 2836-2843.

[134] K. Peng, Y. Wu, H. Fang, X. Zhong, Y. Xu, J. Zhu. Uniform, axial-orientation alignment of one-dimensional single-crystal silicon nanostructure arrays. *Angew. Chem. Int. Ed.* **2005**, *44*, 2737-2742.

[135] K. Peng, H. Fang, J. Hu, Y. Wu, J. Zhu, Y. Yan, S. Lee. Metal-particle-induced, highly localized site-specific etching of Si and formation of single-crystalline Si nanowires in aqueous fluoride solution. *Chem. Eur. J.* **2006**, *12*, 7942-7947.

[136] J. Kim, Y. H. Kim, S. Choi, W. Lee. Curved silicon nanowires with ribbon-like cross sections by metal-assisted chemical etching. *ACS Nano* **2011**, *5*, 5242-5248.

[137] X. G. Zhang. *Electrochemistry of Silicon and Its Oxide*, Kluwer Academic/Plenum Publishers: New York, 2001.

[138] O. J. Hildreth, D. Brown, C. P. Wong. 3D out-of-plane rotational etching with pinned catalysts in metal-assisted chemical etching of silicon. *Adv. Funct. Mater.* **2011**, *21*, 3119-3128.

[139] A. Parness, D. Soto, N. Esparza, N. Gravish, M. Wilkinson, K. Autumn, M. Cutkosky. A microfabricated wedge-shaped adhesive array displaying gecko-like dynamic adhesion, directionality and long lifetime. *J. R. Soc. Interface* **2009**, *6*, 1223-1232.

[140] S. Chary, J. Tamelier, K. Turner. A microfabricated gecko-inspired controllable and reusable dry adhesive. *Smart Mater. Struct.* **2013**, *22*, 025013.

[141] D. R. Turner. On the mechanism of chemically etching germanium and silicon. J. *Electrochem. Soc.* **1960**, 107, 810-816.

[142] B. Schwartz, H. Robbins. Chemical etching of silicon IV. etching technology. *Electrochem. Soc.* **1976**, *123*, 1903-1909.

[143] D. Resnik, D. Vrtacnik, U. Aljancic, M. Mozek, S. Amon. Different aspect ratio pyramidal tips obtained by wet etching. *Microelectron. J.* **2003**, *34*, 591-593.

[144] M. Bauhuber, A. Mikrievskij, A. Lechner. Isotropic wet chemical etching of deep channels with optical surface quality in silicon with HNA based etching solutions. *Mater. Sci. Semicond. Process* **2013**, *16*, 1428-1433.

[145] A. A. Hamzah, N. Abd Aziz, B. Yeop Majlis, J. Yunas, C. F. Dee, B. Bais. Optimization of HNA etching parameters to produce high aspect ratio solid silicon microneedles. *J. Micromech. Microeng.* **2012**, *22*, 095017.

[146] W. Hui, "How to prevent a runaway chemical reaction in the isotropic etching of silicon with HF-HNO_3-CH_3COOH or HNA Solution. *Proc. SPIE* **2004**, *5276*, 270-279.